

PERFORMANCE QUALIFICATION AND RAMAN INVESTIGATION ON
CELL BEHAVIOR AND AGING OF LiFePO_4 CATHODES
IN LITHIUM-ION BATTERIES

by

AMIR SALEHI

Presented to the Faculty of the Graduate School of
The University of Texas at Arlington in Partial Fulfillment
of the Requirements
for the Degree of

MASTER OF SCIENCE IN MATERIALS SCIENCE AND ENGINEERING

THE UNIVERSITY OF TEXAS AT ARLINGTON

May 2013

Copyright © by Amir Salehi 2013

All Rights Reserved

ACKNOWLEDGEMENTS

It is my pleasure acknowledging my supervisor, Dr. Fuqiang Liu for the opportunity he has given me to learn and develop my abilities under his supervision during my research. I always recognize his encouragement and useful advice throughout obstacles which are the nature of any research environment. I appreciated the fact that although he expects improvement and outcomes he allowed me to work on my own way to plan my research. I also appreciate the fact that despite difficulties he was willing to provide financial support that helped me to focus on my research.

I would like to thank my committee members, professor Yao Hao and Dr. David Wetz who accept to serve my thesis committee and to provide their comments which give me correct insight about my future works. I wish to thank my fellow electrochemistry lab members for their grate input, and partnership during my research. I am grateful for the support I've gained from Md. Noor-E-Alam Siddique and Sujay Bagi who helped me in common projects and data analyzing. I do appreciate all the support I've got from the department of Materials Science and Engineering, and CCMB during my research.

I also share the credit of my work with my wife for her dedication in taking all of my responsibilities at home throughout my study and research at UT Arlington.

March 18, 2013

ABSTRACT

PERFORMANCE QUALIFICATION AND RAMAN INVESTIGATION ON CELL BEHAVIOR AND AGING OF LiFePO₄ CATHODES IN LITHIUM-ION BATTERIES

Amir Salehi, M.S.

The University of Texas at Arlington, 2013

Supervising Professor: Fuqiang Liu

This thesis explores the ability of Raman spectroscopy to understand the complex chemistry taking place in LiFePO₄ cathodes of Li ion batteries. The performance of Li ion batteries was optimized through electrode fabrication and assembling procedures. Various amounts of Timcal Super P carbon were used to construct a conductive network of C-LiFePO₄ particles and the performance of the cathodes was examined during battery cycling. Raman spectroscopy along with electrochemical characterization such as charge/ discharge curves, electrochemical impedance spectroscopy and Cyclic Voltammetry was employed for detailed investigation of battery performance and aging. It is found that both quantity and quality of the conductive carbon affect the rate performance and cyclic behavior of the cells. The cathodes with 2% additive carbon showed a faster capacity fading during cycling than that with 10% additive carbon due to a quicker degradation of the conductive network as indicated by sp^2/sp^3 and I_D/I_G ratios in Raman spectroscopy results. The rate performance of cathodes with 2%, 10% and 20 % carbon was also compared and a better rate performance was found for 2% carbon. It showed a proper electronic

network which is mostly provided by carbon coating along with a large pore size of the cathode which facilitates the electrolyte penetration.

Furthermore, in situ Raman spectroscopy was employed to probe electrolyte concentration variation at the cathode LiFePO_4 particle surface in an optically transparent lithium ion cell. A Raman laser spot size of $2\ \mu\text{m}$ was applied so that transport dynamics at individual particle surface could be investigated. The variation of Li^+ concentration in the LiPF_6 /ethylene carbonate (EC) + dimethyl carbonate (DMC) electrolyte was determined, for the first time. This was done by monitoring the C–O stretching vibration signal intensity and the corresponding relationship to EC solvation. The electrolyte concentration at the LiFePO_4 particle surface was found to fluctuate during the battery charge/discharge cycle. Particularly, near the end of battery discharge, it reached to a minimum value which was far less than its initial balanced value ($1\ \text{mol}\cdot\text{dm}^{-3}$).

TABLE OF CONTENTS

ACKNOWLEDGEMENTS	iii
ABSTRACT	iv
LIST OF ILLUSTRATIONS	vix
LIST OF TABLES.....	vi
Chapter	Page
1. INTRODUCTION.....	1
2. BACK GROUND	4
2.1 Lithium ion battery.....	4
2.1.1 Cathode material.....	6
2.1.2 Conductive network of Li-ion battery cathodes.....	10
2.1.3 Electrolyte	13
2.1.4 Anode materials	16
2.2 Aging of LiFePO ₄ cathodes.....	19
2.3 Conduction in Li- ion batteries	20
2.4 Electrochemical impedance spectroscopy.....	23
2.5 Raman spectroscopy	26
2.5.1 The principles of infrared and Raman spectroscopy	26
2.5.2 Application of Raman spectroscopy in the characterization of Li-ion batteries	28
2.5.2.1 Raman spectroscopy of the electrolyte.....	28
2.5.2.2 Raman spectroscopy of the active materials	31
2.5.2.3 Raman spectroscopy of the conductive carbon	35

3. EXPERIMENTAL	40
3.1 Introduction	40
3.2 Making the li-ion battery.....	40
3.2.1 Preparation of the cathode	40
3.2.2 Preparation of the anode	42
3.2.3 Electrochemical cell design	43
3.2.4 Preparation of the electrolyte.....	44
3.2.5 Assembling the cell.....	45
3.3 Electrochemical behavior.....	46
3.3.1 CV test	46
3.3.2 Cycling test	48
3.3.3 Electrochemical Impedance Spectroscopy.....	48
3.4 Characterization.....	48
3.4.1 XRD	48
3.4.2 SEM	49
3.4.3 Raman spectroscopy	49
3.4.3.1 Ex-situ Raman spectroscopy	49
3.4.3.2 In-situ Raman spectroscopy	50
4. RESULT AND DISCUSSION.....	51
4.1 Introduction	51
4.2 Improvement of the cell performance	51
4.2.1 Electrochemical cell design	51
4.2.2 Pressure effect.....	52
4.2.3 Carbon additive effect.....	55
4.2.4 Effect of additive carbon on the cycling behavior.....	64

4.3 Electrochemical Impedance Spectroscopy.....	71
4.4 In-sit Raman spectroscopy of the surface of LiFePO ₄ cathode in a working Li- ion battery	73
4.4.1 Introduction	73
4.4.2 Electrochemical Cell design.....	74
4.4.3 Carbon removal from the cathode surface	75
4.4.4 In-situ Raman spectroscopy	79
4.5 Conclusion	86
REFERENCES.....	88
BIOGRAPHICAL INFORMATION.....	91

LIST OF ILLUSTRATIONS

Figure	Page
2.1 Lithium ion batteries energy density among other batteries	5
2.2 Schematic representation of the charge and discharge process of a lithium rechargeable battery.....	6
2.3 Layered crystal structure of LiCoO_2	7
2.4 Three dimensional frame work of LiMn_2O_4 cathodes.....	8
2.5 The olivine structure of LiFePO_4 : showing the FeO_6 octahedral (grey), PO_4 tetrahedral (brown), and the one-dimensional tunnels in which the lithium ions reside.....	9
2.6 Schematic representation of possible ways of loading conductive additive for improvement of electronic conductivity of the electrodes in Li-ion cells.....	10
2.7 Ionic conductivity of LiPF_6 (open symbols) and LiCF_3SO_3 (filled symbols) in EC-based mixed solvents. (○) $\text{LiPF}_6/(\text{EC}+\text{DMC})$, (◇) $\text{LiPF}_6/(\text{EC}+\text{DME})$, (▽) $\text{LiPF}_6/(\text{EC}+\text{DEC})$, (●) $\text{LiCF}_3\text{SO}_3/(\text{EC}+\text{DMC})$, (◆) $\text{LiCF}_3\text{SO}_3/(\text{EC}+\text{DME})$	14
2.8 (a) The operation range of LiCoO_2 cathode, graphite anode and the stability potential window of most common liquid electrolytes. (b) Formation of SEI layer and gas generation on a typical Li-ion battery	15
2.9 The comparison of different types of anodes for the volume change effects associated to the charge and discharge process in lithium cells.....	18
2.10 (A) Raman spectra of carbonaceous material of C- LiFePO_4 cathode at different discharge rates (C0 new cathode without aging, C1, C2, C4 and C6 discharged at 1C, 2C, 4C and 6C respectively). (B) Experimental Raman spectra with deconvoluted fits of D and G bands. (C) Variation of I_D/I_G of a C- LiFePO_4 cathode at different discharge rates	20
2.11 Typical discharge curve of a battery with various types of polarization.....	23
2.12 (A, top) Simple battery circuit diagram, where C_{DL} represents the capacitance of the electrical double layer at the electrode-solution interface. Z_{anode} and $Z_{cathode}$ are the impedances of anode and cathode reactions and sometimes might be considered as a series resistance capacitance with values derivative from the Argand diagram. This reaction capacitance can be 10 times the size of the double-layer capacitance. The reaction resistance component of Z is related to the exchange current for the kinetics of the reaction. (B, bottom) Argand diagram of the battery circuit diagram for an idealized battery system. The characteristic behaviors of ohmic, activation, and diffusion or concentration polarizations are represented.	24

2.13 The electrochemical impedance spectroscopy (EIS) measurement and the equivalent circuit of the cathode half cell (LiCoO ₂)	25
2.14 Schematic vibrational energy levels and correspond transitions. The thickness of the arrows are indicative of the signal strength of the transitions.....	27
2.15 (a) Raman spectra for symmetric stretching vibration band of C–O single bond and (b) the symmetric ring deformation of EC in the LiCF ₃ SO ₃ system. (A) Solvent DMC, (B) solvent EC+DMC (50 : 50 by volume), (C)-(G) EC+DMC dissolving LiCF ₃ SO ₃ (C: 0.05, D: 0.1, E: 0.5, F: 1.0, G: 1.5 mol dm ⁻³	29
2.16 The variation of the relative intensity with salt concentration change in the LiCF ₃ SO ₃ /(EC+DMC) system. EC (720 (◇) cm ⁻¹), (○) EC (900 cm ⁻¹), (●) DMC (920 cm ⁻¹).....	30
2.17 (A) Average Raman spectra of an LCO cathode sheet. Raman spectra of four different (B) cathode and (C) anode sheets calculating by averaging the individual spectra of a mapped area on the surface of the electrodes	32
2.18 Variation of ν_1 and ν_3 modes in the Raman spectra of Li _x FePO ₄ (0 ≤ x ≤ 1)	33
2.19 The collected Raman spectra of LiFePO ₄ carbon coated olivine powder at different laser powers. He–Ne (633cm ⁻¹) laser source was utilized (a) in air and (b) in helium (99.99%).....	34
2.20 Raman spectra of C- LiFePO ₄ powder at various stages of charge – discharge process (half charge (HC),full charge(FC), half discharge(HC) and full discharge(FD) in frequency range 150 to 1200 cm ⁻¹	35
2.21 Vibrational modes for single-crystal graphite. The B_{2g} frequency is predicted but not yet observed experimentally	37
2.22 Raman spectra and spectrum deconvolution of (a) TIMCAL Super P, (b) TIMCAL Super S, and (c) in-situ carbon	38
3.1 (A) The pin set was used to make tiny holes through the Al foil. (B) the extra material removed from the back of the coated foil	42
3.2 Schematic representation of li-ion experimental cell	44
3.3 The glass reservoir and the epoxy connectors were made separately and then attached together to form the complete structure of the B type cases	45
3.4 The transparent cell with three connection terminals, used for the CV test	46

3.5 The cyclic voltammetry test for the first five cycles after making the cell	47
3.6 XRD pattern of LiFePO ₄ powder synthesized with solid state method	48
3.7 The setup of the in-situ experiment. After placing the case in appropriate position, the wires were passed from a hole through the instrument cover and connected to the charger for cycling	50
4.1 The effect of pressure on the performance of the cathodes with 10% carbon(A) and 20% carbon (B). The cathode was made without applying pressure in dis3 and dis4 and with applying 2.5 ton/cm ² pressure in dis2p and dis3p. The charge and discharge rate of 0.1C was applied in all conditions.....	53
4.2 The effect of pressure on the performance of the LiFePO ₄ cathode with 20% carbon at 5C discharge rate. The cells were assembled using the type A case. 2.5 ton/cm ² pressure applied for making the pressed cathode	54
4.3 The discharge behavior of the cathode with 10% carbon (C10p), and 20% carbon (C20p) at 1C discharge rate for the pressed cathodes at 2.5 (ton/cm ²).....	56
4.4 The variation of the capacity at different charge and discharge rates for the cathodes with (A) 10% and (B) 20% carbon. Both cathodes were pressed by applying 2.5 ton/cm ² . The discharge rate of 0.1C was applied during the discharge for the unmarked points in the discharge cycles	57
4.5 Electrochemical charge and discharge plots of the cells with C2, C10 and C20 cathodes. The charge and discharge performed at (A) 0.1C, (B) 0.5C and (C) 1C rate. The red numbers at the bottom of the figures are the average capacity in mAh/gr	59
4.6 Peak deconvolution of carbon fresh electrodes (A) electrode with 2% carbon (C2) , (B) electrode with 10% carbon (C10).....	60
4.7 (A) and (B) SEM image of synthesized material with solid state method without additive carbon. (C) and (D) SEM image of the cross section of fresh C2 cathode. The pores structure of the cathode is demonstrated in different magnifications indicating insufficient carbon around the active material.	62
4.8 Total discharge capacity of C2, C10 and C20 cathodes in different discharge rates. The cells were assembled in type B cases.....	63
4.9. Schematic representation of the cathodes with different carbon content. (A), (B) and (C) show cathodes with 2% , 10% and 20% additive carbon respectively.....	64
4.10 Cyclic behavior of (A) C2 cathode with 2% carbon additive during 264 cycles, and (B) C10p cathode with 10% carbon additive during 420 cycles. Both capacity fading were studied at 1C rate	66

4.11 Raman spectra of carbonaceous materials with correspond SP^2/SP^3 and I_D/I_G . (A) fresh electrode with 2% additive carbon C2, (B) Aged electrode with 2% additive carbon C2, (C) fresh electrode with 10% additive carbon C10p, (B) Aged electrode with 10% additive carbon C10p.....	67
4.12 Carbon additive conversion over cycling for C2 (with 2% carbon additive) and C10p (with 10% carbon additive) cathodes. Variation of (A) I_D/I_G and , (B) SP^2/SP^3 over cycling.....	68
4.13 SEM image with different magnification of C2 cathode on the left side and C10p cathode on the right side.....	69
4.14 SEM image of C10p cathode after more than cycles. The reduction of the particle size of the cathodes leads to the formation of the cracks in the cathode. The indicated area in (A) and (B) are demonstrated in (B) and (C) respectively with higher magnification	70
4.15 The Nyquist plot of C10 and C20 in the frequency range of 10 KHz –10 mHz. Charge and discharge was performed at (A) 0.1C and (B) 1C	71
4.16 The Nyquist plot of C2 in the frequency range of 10 KHz –10 mHz. Charge and discharge was performed at (A) 0.1C rate and (B) 0.5C and 1C rate.....	73
4.17 Schematic representation of in-situ Raman experimental cell.....	75
4.18 (A) - (E) Raman spectra of the C- $LiFePO_4$ as a function of laser power. Fe_2O_3 and $\gamma-Li_3Fe_2(PO_4)_3$ bands are marked by (*) and (+) symbols, respectively. $LiFePO_4$ peak is marked with (x). The laser beam of 532 nm with a spot size of $2\mu m$ was exposed to the surface of the cathode for 7 min	76
4.19 (a) Raman spectra of individual $(150 \times 150) \mu m^2$ areas in the cathode surface. More oxides from decomposition of $LiFePO_4$ are generated in areas of A and B. The identity of different vibrational bands is labeled in Fig 4.20. (b) Distribution of the band at 950 cm^{-1} in a $(80 \times 80) \mu m^2$ area on the cathode surface. The color map, at the bottom of the figure, correlates correspond Raman intensity and the colors. The red color visualizes the region with the highest Raman intensity with the wavenumber of 950 cm^{-1}	78
4.20 Charge, discharge and rest cycles of the C- $LiFePO_4/Li$ cell during the in-situ experiment. During the first stage of charge and discharge cycle, the cell was charged at a constant rate of 0.4C. The second stage of charge was performed with a constant voltage at 4.0V. The open circles indicate the states when the in-situ Raman spectra were collected	80

4.21 (A) The Raman spectra of DMC. The peak at about 915 cm^{-1} is assigned to C–O stretching band of the bulk DMC. (B) The Raman spectra of EC with the C–O stretching band at about 895 cm^{-1} . (C) Typical in-situ Raman spectra from $(150\text{-}1800)\text{ cm}^{-1}$. The region below 1000 cm^{-1} has been rescaled for better illustration of the weak bands of both electrolyte and LiFePO_4 (*).	81
4.22 De-convoluted Raman spectra (between 870 and 970 cm^{-1}) at different states of the charge during (A) charge, and (B) discharge in the in situ experiment. The C-O stretching Raman bands of the un-solvated (*, at 895 cm^{-1}) and solvated EC (+, at 904 cm^{-1}) are labeled in (A) and (B).	84
4.23 Variation of Li^+ concentration in the $\text{LiPF}_6/\text{DMC}+\text{EC}$ system during charge, discharge, and rest portions of the cycle. The Li^+ ion concentrations were computed from the Raman spectral data (Figs. 4.22 B and C) as described in the text.....	85

LIST OF TABLES

Table	Page
2.1 Crystal structure and electrochemical behavior of Li-ion cathode materials with different amounts of carbon additive	11
2.2 Structure and selected properties of the solvents at 298°K (unless otherwise noted).....	13
2.3 Different types of internal resistance of the cell	22
3.1 The composition and the processing conditions of different cathodes. LiFePO ₄ is made by using the solid state method	41
3.2 The setup of the Raman spectroscope for Ex-situ experiments.....	49
3.3 The setup of the Raman spectroscope for the In-situ experiment.....	50
4.1 Correspond amount of sp ² /sp ³ and I _D /I _G for C2 and C10 cathodes.....	60
4.2 Capacity drop of cathodes by increasing the discharge rate with different carbon additives.....	61
4.3 Cyclic tests on C2 and C10p type cathodes	65
4.4 Characteristic vibrational peaks observed in the in-situ Raman spectroscopy	82

CHAPTER 1

INTRODUCTION

Increasing demand on today's society for energy consumption necessitates reliable and affordable energy sources. Consumption of fossil fuels as the main source of energy over the last century has been negatively impacted the earth's ecological life. Climate change has been recognized as one of the destructive consequences of such approach by many scientists. As a result of using fossil fuels, CO₂ emission has been doubled from 1970 to 2005 [1]. Besides, the oil resources are very limited, considering the political issues regarding the price; it is a fragile source for future energy. Therefore, it is emergent to find alternative energy sources to replace fossil fuels.

Recently a transition has been initiated from using fossil fuels towards all kinds of renewable energy resources. Although today's modern society is still relying on non-renewable energy basis, scientists have started the search for appropriate replacement options. Hydroelectricity, tidal and geothermal energies, wind energy, solar energy and fuel cells, are some of the options.

Utilizing solar or wind power requires an effective energy storage system to compensate the power shortage in the peak usage intervals; therefore, super capacitors and batteries are essential for this purpose [2]. Batteries are the best energy storage systems since they exhibit more energy storage capacities with an energy efficiency of more than 90% [3]. Among all battery systems, lithium ion batteries are the most desired systems for their high energy densities as well as low weight densities [2].

The energy and power density of Li-ion batteries are mostly determined by cathode materials which incorporate their crystal structures with Li ions through a discharge process. Most commercialized cathodes like LiCoO₂, LiMn₂O₄, Li(Ni,Co,Al)O₂ or Li(Ni,Co,Mn)O₂ become

a solid solution for a wide range of concentrations over Li insertion or extraction. However, LiFePO_4 (LFP) forms a two-phase (LiFePO_4 – FePO_4) transition, consequently there are no extra kinetic barriers such as nucleation of second phase or growth through interphase motion, which leads to a remarkably high rate capability of LiFePO_4 [4, 5]. Lithium iron phosphate has a theoretical capacity of 170mAh/gr and practically it can reach to about 95% of its theoretical capacity 160mAh/gr [6]. LiFePO_4 also shows a good cycle ability and thermal stability. The working potential of LiFePO_4 is about 3.5 V vs. Li which is pretty lower than the maximum stability potential (5V) of available organic electrolytes, which makes LFP cathode a safe material during charging/discharging processes.

The improvement of present LFP-based lithium ion batteries requires studying the key components of the cell and their mutual reactions especially understanding real time reactions taking place under working condition. Electrode materials undergo a quick relaxation process during battery cycles [4], therefore ex-situ studies might not be able to access the dynamic processes occurring during the cell performance. Creating appropriate conductive network is also necessary for LFP cathodes since it's a semiconductor with relatively low electronic conductivity (10^{-9} to 10^{-10} S/cm) [7]. Raman spectroscopy is a sensitive technique to investigate the both dynamic chemical and structural variations at the surface. In-situ Raman spectroscopy of Li-ion batteries provides real time information about the dynamic reactions of the cell. Utilizing in-situ technique provides the opportunity for disclosure of mutual interactions between the active material and electrolyte at the surface of the electrode.

This thesis aims to further study the complex chemistry taking place on the LiFePO_4 cathode surface using both in situ and ex situ Raman spectroscopy. To accomplish this task, an electrochemical cell was first designed and utilized to examine the electrochemical performance of the LFP material with various amount of carbon additive, then in-situ Raman spectroscopy employed to study the surface phenomena during working condition of the cell.

This thesis is organized into four chapters. Chapter one is a general introduction including current approach for finding new energy resources, the importance of lithium ion batteries as an effective energy storage system, and motivation for understanding the complex reactions in Li-ion batteries. Chapter two provides a background of our research starting with the structure of Li-ion batteries and its components also the electrochemical reactions taking place in an actual cell. Impedance spectroscopy as an effective tool for cell diagnosis is briefly explained and subsequently, theory and application of Raman spectroscopy for characterization of Li-ion cell is discussed. The experimental part is summarized in chapter three, starting with the composition of the cathodes, cell structure, assembly and electrochemical test conditions. It proceeds with characterization of the microstructure and Raman spectroscopy experiments. Chapter four contains our experimental results and discussion. The cell performance is first studied based on the cathodes with various densities and carbon contents. Then the impedance behavior of the cells and the procedure for in-situ Raman experiment are explained. Finally, in the end of chapter four, the conclusion of our research is summarized.

CHAPTER 2

BACKGROUND

2.1 Lithium ion batteries

Lithium metal is a light and abundant element with a small atomic radius which makes it a favorite choice for energy storage application. Utilizing the unique characteristics of lithium in the lithium ion batteries provides a compact and light energy storage system as seen in Fig.2.1. They usually generate a voltage of about 4V with a specific energy density between 100Whkg^{-1} and 150Whkg^{-1} [8].

The structure of batteries is composed of cathode, anode, separator and electrolyte. Fig.2.2 shows a schematic configuration of a Li-ion battery. Lithium ions migrate between the electrodes during charge and discharge. Graphite is mostly used as the anode for the commercial lithium ion batteries. The layered structure of the graphite accommodates lithium ions between the layers. The electrolyte, an ionic conductive agent, is generally composed of an organic mixed carbonate solvent (dimethyl carbonate, DMC, and ethylene carbonate, EC) with a dissolved lithium salt like lithium hexafluorophosphate (LiPF_6). The cathode acts as a host structure for the lithium ions and provides appropriate space for lithium ion diffusion. The separator, typically a porous polyethylene polymer, provides appropriate path way for lithium ions, meanwhile prevents the electrodes from shorting [9].

During the charging process, lithium ions leave the cathode towards anode and electrons move in the same direction from the external circuit. Therefore, cathode undergoes an oxidation reaction during the charging process. Meanwhile as the lithium ions and electrons enter the anode side, reduction happens in the anode. In the discharge process, lithium ions leave the anode towards cathode, passing through the electrolyte, at the same time electrons

move in the same direction from the external circuit. Consequently oxidation of the anode and reduction of the cathode electrode occur in the discharge process.

The capacity of the electrodes is defined by the quantity of the lithium ions they can host in the crystal structure. Today's lithium ion batteries are based on the insertion mechanism in which lithium ions form intercalation compounds by occupying the interatomic spaces in the host crystal structure. Typically a maximum of one electron is generated per transition metal in an insertion reaction which increasingly limits the specific energy of the batteries. Notable increase of the performance is reported by conversion chemistry which introduces two to six electron transfer [10].

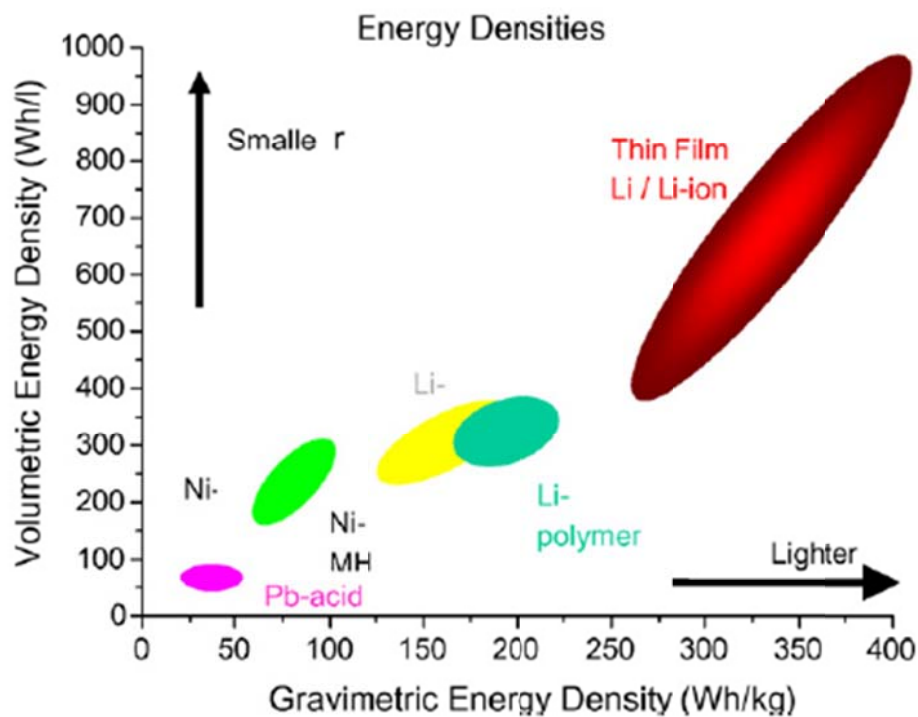


Figure 2.1 Lithium ion batteries energy density among other batteries[7].

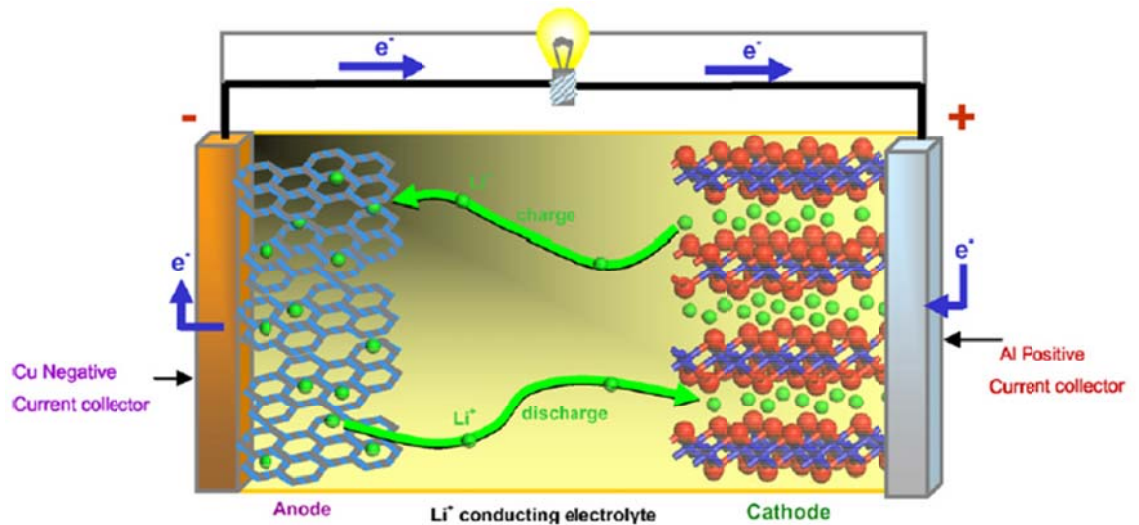


Figure 2.2 Schematic representation of the charge and discharge process of a lithium rechargeable battery [7].

2.1.1. Cathode materials

Lithium metal oxides have been used as the cathode materials for many years. Layered LiCoO_2 (Fig.2.3) was utilized as the cathode of the first commercial li-ion battery by Sony in 1991. Since then lots of researches have been conducted to improve the performance and safety of the cells utilizing other transition metal oxides like LiMn_2O_4 , $\text{LiNi}_{0.5}\text{Mn}_{1.5}\text{O}_4$ [1]. Today's main interest of the manufactures about the cathode material is manganese-based compounds and olivine lithium metal phosphates. Among all available cathode material, olivine lithium iron phosphate is a fascinating choice for today's applications; however, high capacities are required for some applications like EVs or HEVs. LiFePO_4 with the theoretical capacity of 170 mAh/gr is an acceptable cathode material considering other available candidates like spinel LiMn_2O_4 (Fig.2.4) and LiCoO_2 with the theoretical capacity of 148 and 274 mAh/gr respectively [6]. The LiFePO_4 and LiMn_2O_4 are environmentally friendly, while the toxic nature of cobalt makes the LiCoO_2 cathodes potentially harmful. LFP cathodes are more stable than LMO (layered LiMnO_2 or spinel LiMn_2O_4) and during charge and discharge show a flat plateau around 3.5 V. However, LFP is naturally a semiconductor with the electronic conductivity of 10^{-9} Scm^{-1} [11] which is

relatively low when compared to the conductivity of 10^{-3} Scm^{-1} for LiCoO_2 [12]. Hence, additional processes require for the application of LFP as the cathode active material.

John Goodenough first reported the electro-active behavior of Li_xCoO_2 as the cathode material in 1980 while at Oxford University [13]. It has a high structural stability so it can be cycled more than 500 times with 80–90% capacity retention. The layered structure of LiCoO_2 provides appropriate space for lithium ions to diffuse into the material. Its specific capacity of about 140 Ah/kg and density capacity of 690 Ah/L are due to the ability of releasing half of the lithium atoms per mol and oxidizing half of cobalt to the trivalent stage. Thin film Li_xCoO_2 cathode gives the best power densities between 4.2 and 3.0 V [14]. The diffusion coefficients from 10^{-11} to $10^{-12} \text{ m}^2/\text{s}$ at room temperature have been reported for Li_xCoO_2 that are indicative of its good lithium mobility [15]. Despite the above-mentioned advantages of LCO, their toxic nature and high cost comparing to other available materials led the investigation for more appropriate materials.

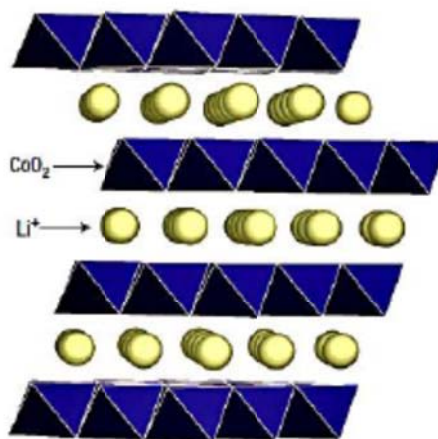


Figure 2.3 Layered crystal structure of LiCoO_2 [16].

Manganese oxides are among available cathode materials that have been used due to their low cost, abundant and environmental friendliness. LiMn_2O_4 is the most attractive one since it is more stable than LiMnO_2 under over charged situations, providing a favorable capacity with a relatively high electronic conductivity. LiMn_2O_4 has a three-dimensional spinel

type crystal structure, with a cross linked channels that are large enough for lithium insertion. The expansion-contraction of the structure due to insertion and extraction of lithium ions is less than that of the LCO cathode [17]. The relatively low capacity, instability at high temperatures, shorter cycle life and undesirable dissolution of small particles are among the main unfavorable properties of the LiMn_2O_4 cathodes. Comparing to LCO, performance of the LiMn_2O_4 cathodes are not easily reproducible in terms of the cell resistance and cycle ability.

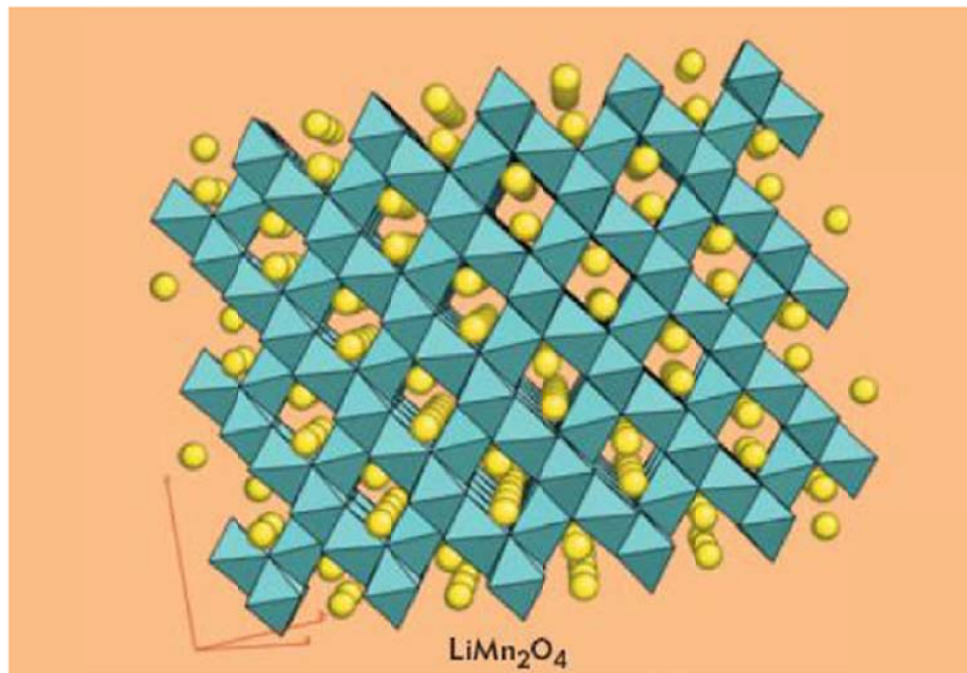


Figure 2.4 Three dimensional frame work of LiMn_2O_4 cathodes[7].

Lithium iron phosphate is a promising material as an alternative for the cathode of lithium ion batteries. LiFePO_4 as an electro-active cathode for rechargeable lithium batteries presents a relatively high energy density, thermal stability at fully charged state and safety also is a cheap and non-toxic material. LFP with an olivine type crystal structure (Fig.2.5) shows a flat plateau of intercalation voltage about 3.5 V relative to lithium metal. It is stable in common organic electrolytes and also is easy to synthesize [18].

John Goodenough and co-workers at the University of Texas, Austin discovered the LFP as the cathode of the li-ion batteries in 1997 [19]. But it has been ignored due to its low electronic conductivity (10^{-9} to 10^{-10} S/cm) [7]. Li, Fe and P atoms occupy octahedral 4a, octahedral 4c and tetrahedral 4c sites, respectively, in the ordered olivine structure of LFP which is in fact made of two separate LiFePO_4 and FePO_4 phases. Fe cations have only one oxidation states in these phases (2^+ in LiFePO_4 and 3^+ in FePO_4) and practically the full capacity was not achievable because as the electrochemical reaction proceeds, electronically isolated areas remains intact in the bulk electrode. In order to get acceptable energy, the small particles should be coated with an electronically conductive agent [20]. The conductive coating reduces the Li^+ transport distance and increases the electronic contact between the particles; consequently, the coated particles result in a greatly improved electrochemical behavior with a full capacity even after a long cycling. LFP can presently reach to 90% of its theoretical capacity with noble rate performance which make it as a favorite candidate for today's applications [7].

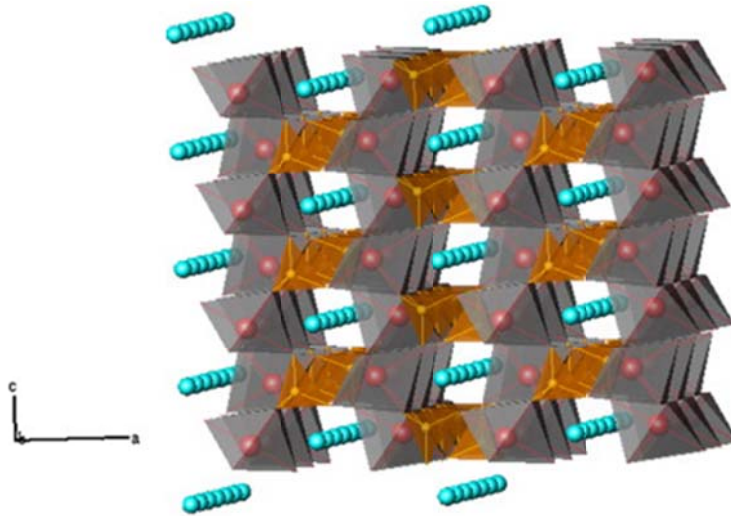
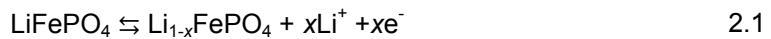


Figure 2.5 The olivine structure of LiFePO_4 : showing the FeO_6 octahedral (grey), PO_4 tetrahedral (brown), and the one-dimensional tunnels in which the lithium ions reside [21].

The insertion mechanism of LFP cathode is summarized using the following equation:



During lithiation and delithiation, the length of P-O and Fe-O bonds change and the volumetric change is approximately 6.5% [19, 22]. As the volumetric change is low the LFP cathodes show a good cycleability. The volumetric change of the unit cell for LCO cathodes is about 10% leading to a weaker cycle ability than LFP [23].

2.1.2. Conductive network of Li-ion battery cathodes

Presence of an appropriate electronic component in the cathode is crucial for proper transferring of electrons between the current collector and the active material in the bulk of the electrode. Several approaches have been reported for constructing an electronically conductive frame work to increase the electronic conductivity of LFP materials [6, 11, 24, 25]. As Fig.2.6. shows, the loading of conductive additives that might be implemented in different configurations.

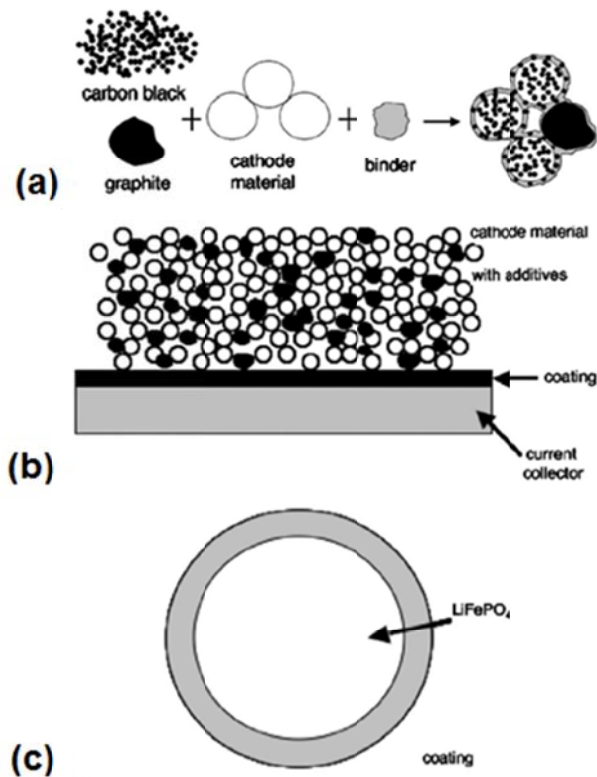


Figure 2.6 Schematic representation of possible ways of loading conductive additive for improvement of electronic conductivity of the electrodes in Li-ion cells [6].

Carbon black additive provides appropriate porosity for penetration of the electrolyte inside the electrodes and also builds a supportive framework for the active material particles. Carbon black is amorphous carbon and mainly composed of sp^3 type orbital and consequently is not conductive. Graphite, on the other hand is a conductive additive which its sp^2 electronic structure provides appropriate electronic conductivity for transferring electrons between the active material and current collector. Therefore appropriate ratio between graphite and carbon black might be considered for different applications. The carbon additive effect on the performance of different cathode materials is summarized in Table 2.1.

Table 2.1 Crystal structure and electrochemical behavior of Li-ion cathode materials with different amounts of carbon additive [6].

Cathode material	Crystal structure	Theoretical capacity (mAh/gr)	additive	Amount (wt%)	Capacity (mAh/gr)	Conductivity	Other
LiCoO ₂	Layered	274	Carbon	5-10	158	-	-
			Carbon black	5	-	-	Slight improvement in cyclability from 125 to 133 (mAh/g) in 10 cycles
LiMn ₂ O ₄	Spinel	148	Nonaqueous ultrafine carbon with TAB2	20 (1:3-1:1)	130	-	-
			Carbon black	32.2	135	-	-
LiFePO ₄	Olivine	170	Carbon black	31	-	Conductivity increase: 5×10^{-8} to 0.1 S/cm	-
			Carbon black Graphite	6 6	160	Resistance decrease: 140 to 80 Wcm ²	-

Although additive carbon increases both porosity and electronic conductivity of the electrode, the excessive amount of additive carbon reduces the volumetric energy density of the electrodes. Hence, the adjustment for the composition of the active material and additive carbon is crucial to meet the optimum electrochemical performance of the electrodes. Practically any

adjustment for the active material and additive carbon requires the balance for the amount of the binder. Binder in the li-ion cells is usually a chemically stable material like PTFE. Employing less amounts of binder leads to a weak bonding between the electrode particles and excessive binder decreases the direct contacts between the active material and the conductive carbon. Therefore, optimization of the binder is also important.

LiFePO_4 is an attractive active material as the cathode of Li-ion batteries. However the limitation in the electronic conductivity of LFP as the active material restricts its performance especially in high rate charge and discharge situations. Two methods might be employed to increase the electronic conductivity: doping the active material or adding an electronically conductive network to LFP. Doping changes the electronic structure of the active material leading to a different electrochemical behavior. Coating of active material particles with conductive agents (carbon, polymers, RuO_2 , or others) [11] has been reported to improve the conductivity of the particles which is a renowned and effective method to increase the conductivity of the LFP cathodes. Since the carbon coating covers the particle surface, the insertion or extraction of lithium ions would be possible in many different sites on the surface of the active material which in turn improves the performance of the electrode. In this case the coating must be thin enough, on the nano scale so that lithium ions can penetrate through without appreciable polarization. Besides the internal electric field generated by electrons may enhance the lithium ions motion [25, 26].


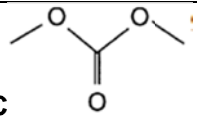
The construction of the cathode for the high rate charge and discharge applications like EVs and HEVs requires fast lithium diffusion in the LFP as well as enhanced electronic conductivity. Such properties have been reported for nano sized LiFePO_4 coated with a thin layer of lithium phosphate, which acted as a Li^+ reservoir to direct Li^+ into the b and c directions of the unit cell, enhancing the diffusion of Li^+ in the particles [5]. This cathode construction could be cycled at rates as high as 400C (i.e., charged and recharged within a few seconds), which would be sufficient for EV and HEV applications.

Later on, in chapter 4 we discuss how limitation of lithium concentration on the surface of lithium iron phosphate limits the intercalation of the lithium ions to the particles during discharge. The improved electronic conductivity and lithium diffusion rate has also been reported for LiFePO₄/C composite cathode [11].

2.1.3. Electrolyte

Electrolyte is a critical component of lithium ion cell which provides appropriate ionic conductivity for Li⁺ transport and also has interface with both the anode and cathode electrodes. Conventional lithium ion batteries mostly employ a mixture of organic carbonate solvent (EC+DMC) with a lithium salt like LiPF₆ as electrolyte. Table 2.1 summarizes the molecular structure and selected properties of EC and DMC solvents. EC has a relatively high dielectric constant which helps to dissociate the dissolved salt; however it is in solid state at room temperature and should be mixed with a low viscosity solvent like DMC for appropriate ion transportation.

Table 2.2. Structure and selected properties of the solvents at 298°K (unless otherwise noted) [27].

Solvent	Molecular weight	Density 10 ³ kgm ⁻³	Relative permittivity at 313°K	Viscosity /10 ⁻² P	Donicity
 EC	88.1	1.32	89.8	1.93	164
 DMC	90.1	1.06	3.1	0.63	15.1

The ionic conductivity of the electrolyte depends on the salt concentration and shows a maximum for a certain amount of salt. The behavior of the electrolyte at various salt concentrations has been reported for mixed solvent systems (Fig.2.7). As the salt concentration increases, the conductivity of the electrolyte increases and presents a maximum. Further

increase in the salt concentration slowly decreases the resultant conductivity. The optimum salt concentration of the electrolyte systems with dissolved LiPF_6 is about $(0.8-1) \text{ mol dm}^{-3}$. Any deviation from the optimum salt concentration reduces the cell performance especially for lower concentrations. Consequently, adjustment of the salt concentration for the electrolyte is crucial to reach the optimum performance of the cell.

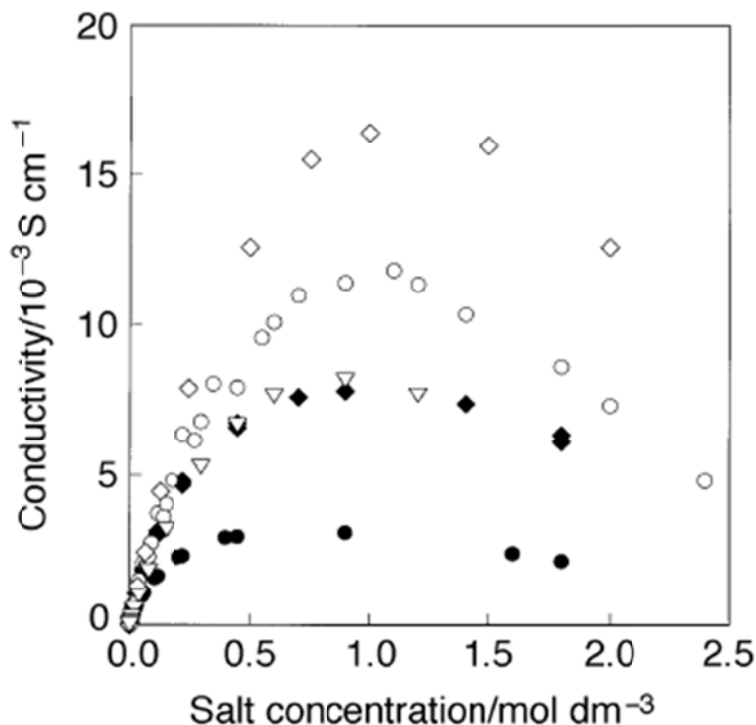


Figure 2.7 Ionic conductivity of LiPF_6 (open symbols) and LiCF_3SO_3 (filled symbols) in EC-based mixed solvents. (\circ) $\text{LiPF}_6/(\text{EC}+\text{DMC})$, (\diamond) $\text{LiPF}_6/(\text{EC}+\text{DME})$, (∇) $\text{LiPF}_6/(\text{EC}+\text{DEC})$, (\bullet) $\text{LiCF}_3\text{SO}_3/(\text{EC}+\text{DMC})$, (\blacklozenge) $\text{LiCF}_3\text{SO}_3/(\text{EC}+\text{DME})$ [27].

The stability potential of the conventional electrolyte expands from 0.8 V to 4.5V vs. Li (Fig.2.7.a). If the potential of the battery electrodes falls within the stability potential window of the electrolyte, they form a thermodynamically stable system. Surprisingly, Mesocarbon microbids (MCMB) (2.1.4), which is widely being used as anode material, is thermodynamically unstable in LIB system due to its low stability potential (0.05V vs. Li) [8]. Consequently, MCMB reacts with electrolyte and the process is accompanied with gas generation. However, formation

of a protective Solid Electrolyte Interphase (SEI) layer on anode prevents farther decomposition of the electrolyte. Cathode electrodes like LCO and LMO also react with conventional electrolyte at potentials higher than 4 V to form oxides (Fig.2.8.b). Although the potential of LCO/conventional electrolyte/MCMB is below 4.0V under normal working condition, in case of accidentally overcharge situation, the oxidation of cathode materials may cause serious safety issues like explosion of the overcharged battery. Over discharge situation also may damage SEI film on anode which leads to gas generation inside the cell.

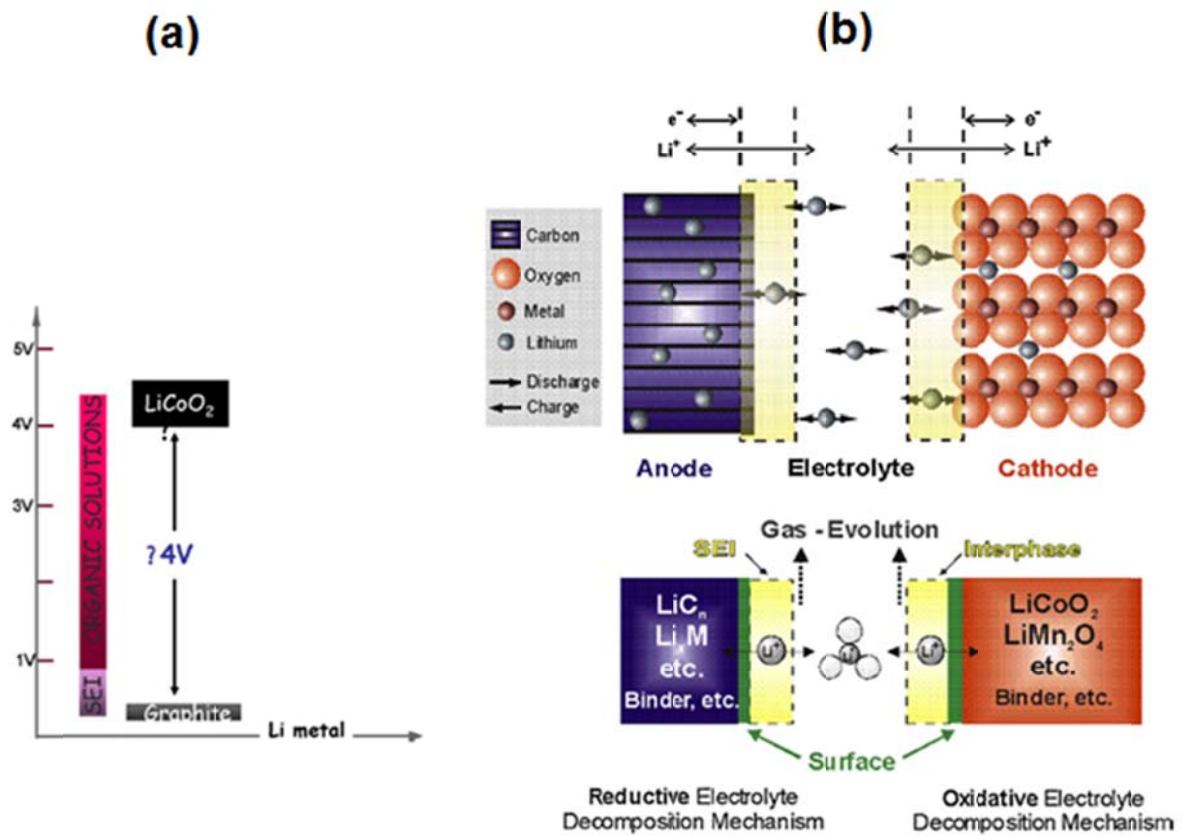


Figure 2.8 (a) The operation range of LiCoO₂ cathode, graphite anode and the stability potential window of most common liquid electrolytes. (b) Formation of SEI layer and gas generation on a typical Li-ion battery [8].

The disadvantages of the conventional liquid electrolyte are summarized as: (i)relatively narrow stability potential window that prevents utilizing electrodes beyond the window; (ii) the

safety concern for high vapor pressure and flammability of the electrolyte; (iii) environmental incompatibility and toxic nature. Several approaches have been attempted for improvement of the liquid electrolyte system including additives for making stable SEI layer or improvement of the thermal stability, shot-down separators for preventing thermal runaway, and utilizing other lithium salts than LiPF_6 to reduce the toxic nature.

Solvent-free lithium conducting membranes are an ideal choice to a more reliable system. Solvent-free electrolytes are based on homopolymers, such as polyethylene oxide and PEO which host a lithium salt, LiX , e.g. lithium trifluoromethanesulfonate (LiCF_3SO_3). Although they only show high ionic conductivity above 70°C , their application for automotive industry where the temperature is not a critical factor, is quite possible. Nanoparticles of ceramic additives in the polymer bulk of PEO reduce the working condition to 60°C by forbidding crystallization of PEO from their amorphous state at temperatures above 60°C . Other approaches include utilizing Gel-type Polymer Electrolyte (GPE) and Ionic liquids (ILs) (low temperature molten salts). The mechanism of GPE is based on trapping typical liquid lithium ion solutions (e.g. LiPF_6 -carbonate solvent mixtures) in a polymer matrix, e.g., poly(acrylo nitrile), PAN or poly(vinylidene fluoride), PVDF. ILs are non-volatile, non-flammable, highly conductive, environmentally compatible and can safely operate in a wide temperature range. They are typically formed by the combination of a weakly interacting, large cation, e.g., the imidazole type, and a flexible anion, e.g., N,N-bis(trifluoromethanesulfonyl), imide (TFSI). The main issue of ILs is their high cost; however, they can be used as additives to the common organic liquid electrolyte solutions to reach a reasonable cost [8].

2.1.4. Anode materials

Carbonaceous materials, Li alloys and Lithium Titanium Oxide (LTO) are among the anode materials for the lithium-ion batteries. Carbonaceous materials like, Mesocarbon microbids (MCMB) are the most popular anodes for commercial Li-ion batteries. They exhibit a high specific charge along with appropriate negative redox potentials, also a better cycling

performance than Li alloys due to their dimensional stability. During the charging process, lithium ions diffuse reversibly into the carbon structure and form a lithium/carbon intercalation Li_xC_n compound. The crystallinity, microstructure and the morphology of the carbonaceous material indicate the quality of the intercalated compound. Therefore, the potential and current characteristics of the anode electrochemical behavior are determined by the carbon type. One of the disadvantages of carbonaceous anodes is the safety issue. Though MCMB with the potential of 0.05 V vs. Li is favorable for having a higher cell energy density, the potential is lower than the minimum stability potential of conventional electrolytes and SEI layer forms on the surface of carbonaceous anode (session 2.1.2). Under over discharge or over heating conditions, SEI layer may be detached from the anode surface leading to gas generation and explosion of the cell.

Li alloys are alternative materials to replace common carbon based electrodes. Lithium–silicon (Li–Si), and lithium–tin (Li–Sn), alloys, are the most promising materials for improving the anode capacity. Li–Si and Li–Sn alloys show the capacity of 4000mAhg^{-1} and 990mAhg^{-1} which are much higher than 370mAhg^{-1} for Li–graphite electrode. Unfortunately the volumetric change of the charged and discharged state is too much for the Li alloy materials which produce lots of mechanical stress in the crystal structure, consequently intense capacity fading occurs over the cycling process [28](see Fig.2.9).

Utilizing nanostructured anode construction lessens the volumetric change effect leading to long cycling behavior along with improved capacity. For example the matrix of carbon in the metal-carbon nanocomposites such as tin-carbon acts as a protecting shell for the nanopowders, and at the same time provides enough space for volume expansion which leads to improved stability over cycling [29].

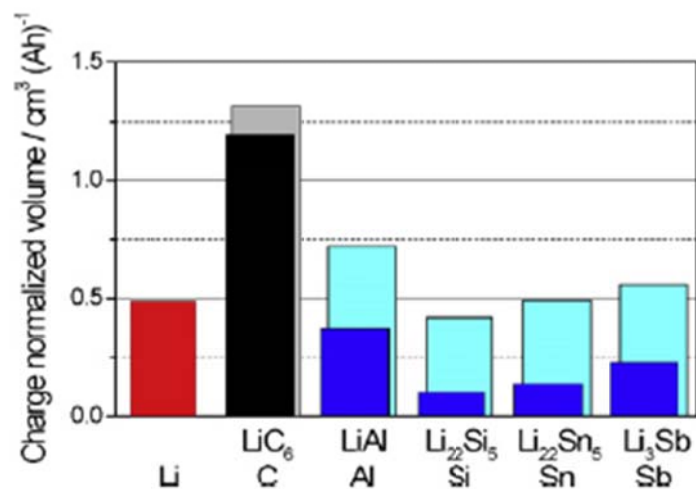


Figure 2.9 The comparison of different types of anodes for the volume change effects associated to the charge and discharge process in lithium cells [8].

Anode materials based on titanium oxides are another alternative for the anode electrode providing a safer cell performance. Anatase titanium oxide TiO_2 (TO) [30] and lithium titanium oxide, $\text{Li}_4\text{Ti}_5\text{O}_{12}$ (LTO) [31] are attractive anode materials with the insertion potential between 1.2V and 2.0V vs. Li which is within the stability window of the common electrolytes. LTO has a lithium rich spinel crystal structure, showing a flat plateau (a two phase electrochemical behavior) with a theoretical capacity of 170mAhg^{-1} and potential of 1.5V vs. Li. The capacity and the resultant potential of the cell using LTO are less than that of graphite (capacity and potential of 370mAhg^{-1} and 0.05V vs. Li respectively) which leads to a lower specific energy density. However, $\text{Li}_4\text{Ti}_5\text{O}_{12}$ is still an attractive anode material for several reasons: (i) high stability over cycling (less than 1% charge/ discharge volumetric change); (ii) decent capability of charge and discharge at a high rate and very low temperature; (iii) high thermal stability in both charged and discharged states and (iv) no SEI formation on the surface of the anode since no decomposition occurs on its working potential. Titanium oxide, TO, in a brookite crystal structure is a cost effective and safe anode material with the environmental friendliness nature, showing a theoretical capacity of 335mAhg^{-1} . The electrochemical

performance of the TO depends on the particle morphology as a result research has been conducted to find appropriate production and processing of Nano material [31, 32].

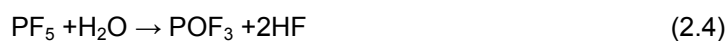
2.2 Aging of LiFePO₄ cathodes

LiFePO₄ is a relatively stable material as the cathode of Li-ion batteries. It shows a good thermal stability at elevated temperatures which reduces the risk of decomposition due to overheating in possible overcharging or high discharge rate conditions. Despite the stability of LFP materials, actual Li-ion batteries based on LFP cathodes show a gradual capacity fading along with an increase of the impedance over time.

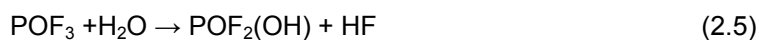
Several mechanisms have been proposed for the degradation of the cathode during cycling. One notable effect is the existence of unavoidable moisture in the cell especially by using LiPF₆ salt in a mixed organic solvent. The reaction of water and LiPF₆ forms HF which leads to Fe dissolution. The mechanism of reaction between water and LiPF₆ in organic solvents has been reported based on the following equations [33]:



LiPF₆, which is nonelectrolytic dissociative, produces PF₅, a strong Lewis acid, and PF₅ reacts with water.



It is also possible that POF₃ may react with water via the following equation:



Iron dissociation in different electrolytes in the presence of HF leads to the capacity fading over aging [34]. However, the exact mechanism of Fe dissolution, the impact of HF and H₂O contaminants on Fe ion dissolution, and the surface chemistry of LiFePO₄ electrodes in these solutions has not yet been determined [35]. Also the effect of different synthesis routes on the stability of cathodes in presence of moisture at various temperatures has been studied through the cell impedance and CV tests [36]. Formation of LiF (2%-5%) on carbon-coated Li_xFePO₄

materials and about 18% LiF on LiCoO₂ over cycling have been reported using X-Ray Photoelectron Spectroscopy [37].

Variation in the quality of carbon coating of LFP cathode at various discharge rates has been investigated by means of Raman spectroscopy [38]. It seems that the degradation of conductive network of the cathode especially at high discharge rates has a notable effect on the cell performance which leads to capacity fading of the cell over cycling.

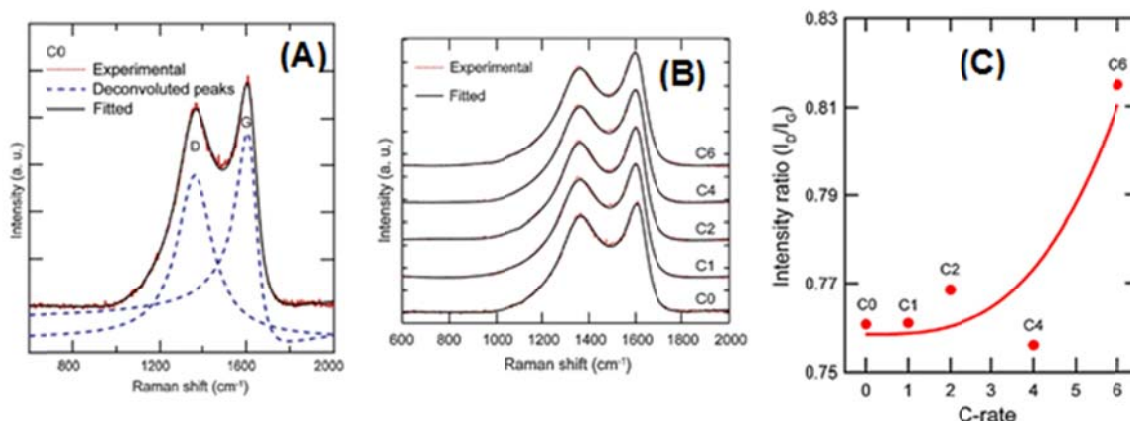


Figure 2.10 (A) Raman spectra of carbonaceous material of C-LiFePO₄ cathode at different discharge rates (C0 new cathode without aging, C1, C2, C4 and C6 discharged at 1C, 2C, 4C and 6C respectively). (B) Experimental Raman spectra with deconvolution fitting of D and G bands. (C) Variation of I_D/I_G of a C-LiFePO₄ cathode at different discharge rates [38].

Fig.2.10 (C) and (B) show the variation of I_D/I_G of a C-LiFePO₄ cathode at different discharge rates along with corresponding Raman spectra of the carbonaceous material of the electrode. Deconvolution method was used for fitting the experimental Raman spectra, considering two G and D bands. A Lorentz fitting method is used for D band and Breit-Wigner-Fano (BWF) function fit for G band (Fig.2.10.A). High discharge rate leads to the formation of poor quality carbon which decreases the electronic conductivity of the carbonaceous network [38].

2.3 Conduction in Li-ion batteries

Generally, all key phenomena involving conducting charged particles from cathode to anode and vice versa are important to study the conductive behavior of an electrochemical cell.

Li ion exchanges one electron in the redox reaction in the Li-ion cell (Fig.2.2.). The ease of electron transfer between the anode and cathode through current collectors, electrical leads and electrodes in outer circuit indicates the magnitude of cell's driving force. Also the ionic conductivity of the electrolyte and electrodes for transferring Li ions are important to complete the electrochemical reaction. The operating potential of the cell is lower than the standard cell potential due to several potential drops which can be shown as following equation:

$$E_T = E_{ocv} - [(\eta_{ct})_a + (\eta_{ct})_c] - [(\eta_c)_a + (\eta_c)_c] - IR_i = IR_a \quad (2.6)$$

where E_T is the operating potential of the cell, E_{ocv} is the standard cell potential, $(\eta_{ct})_a$ and $(\eta_{ct})_c$ are activation polarizations (charge-transfer over voltage) at the anode and cathode, $(\eta_c)_a$ and $(\eta_c)_c$ are concentration polarizations at the anode and cathode, I is the cell operating current, R_i is the internal resistance of the cell and R_a is the apparent cell resistance [39].

Kinetics of charge transfer and mass transfer are related to activation and polarization concentrations respectively. Activation polarization, η_a , occurs due to the limitation of the charge transfer reaction. The current or flow rate of a charge-transfer reaction can be explained by following equations:

$$i = i_0 \exp(\alpha F \eta_a / RT) - \exp((1 - \alpha) F \eta_a) / RT \quad (\text{Butler-Volmer equation}) \quad (2.7)$$

$$\eta_a = a - b \log(i/i_0) \quad (\text{Tafel equation}) \quad (2.8)$$

where a and b are constant numbers, $(i=I/A)$ is the current or flow rate, A is the surface area of the electrode, $i_0 = k_0 F a$ is the exchange current density, F is the Faraday constant, k_0 is the reaction rate constant for the electrode reaction, and a is the activity product of the reactants, R is the gas constant and α is the transfer coefficient, which is best considered as the fraction of the change of overpotential that leads to a change in the rate constant reaction occurs fast in a time frame of 10^{-2} - 10^{-4} s [40].

Concentration polarization, η_c , arises from the limitation in the mass transport capabilities like limited diffusion from the electrode surface that might occur at the end of the

charge or discharge to replace the reacted material. Concentration polarisation reactions can be explained by the following equation:

$$\eta_c = (RT/n) \ln(C/C_0) \quad (2.9)$$

where C is the concentration at the electrode surface and C_0 is the concentration in the bulk of the solution. The concentration polarization reactions are relatively slow and buildup and decay take more than 10^{-2} s [40].

Internal resistance R_i of the cell can be separated into ionic, interfacial and electrical resistance which are summarized in Table 2.3.

Table.2.3 Different types of internal resistance of the cell [39].

Type of resistance	Internal resistance of cell ($R_i =$ ionic resistance + electrical resistance+interfacial resistance)
Ionic	<ul style="list-style-type: none"> • Electrode(cathode and anode) particle • Electrolyte
Electrical	<ul style="list-style-type: none"> • Electrode(cathode and anode) particle • Conductive additives • Percolation network of additives in electrode • Current collectors • Electrical taps
Interfacial	<ul style="list-style-type: none"> • Between electrolyte and electrodes • Between electrode particles and conductive additives • Between electrode and current collector • Between conductive additives and current collector

Total internal resistance is the sum of each internal resistance. Quantitative interpretation of potential drop is quite challenging because multiple parameters affect the total potential drop of the cell. The influence of various types of polarizations is shown in Fig. 2.11.

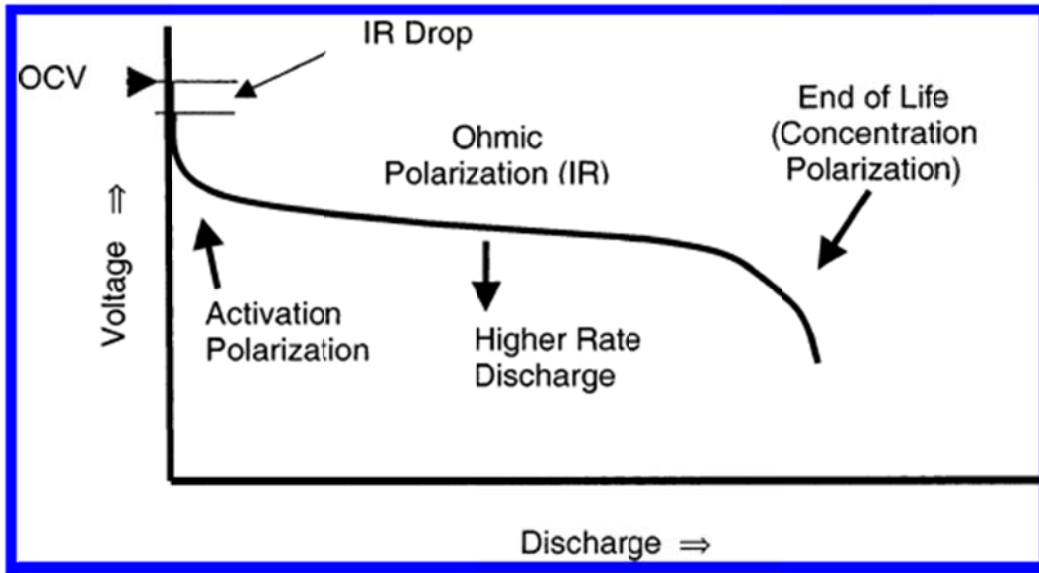


Figure 2.11 Typical discharge curve of a battery with various types of polarization. [40].

2.4. Electrochemical Impedance Spectroscopy

Electrochemical impedance spectroscopy (EIS) is a sensitive technique for the study of the internal components of an electrochemical system. AC EIS has great advantages in comparison with DC electrochemical technique. It can provide detailed kinetic information and also can be used to monitor changes in the battery properties at different states of usage and storage conditions: the state of charge, reaction mechanisms, possible change in the active surface during operation, separator evaluation, SEI formation, possible electrode corrosion, and the kinetics of each electrode. EIS is a non-destructive method since the perturbation of the AC signal is very small. Depending on the analysis type, EIS may be implemented at either galvanostatic (constant current) or potentiostatic (constant voltage) modes.

The impedance of an electrode or battery can be shown by the following equation:

$$Z = R + j\omega X \quad (2.10)$$

where $X = \omega L - 1/(\omega C)$, $j = \sqrt{-1}$ and ω is the angular frequency ($2\pi f$); L is the inductance, and C is the capacitance. A schematic diagram of the equivalent circuit of a battery and the corresponding Argand diagram are shown in Fig.2.12.

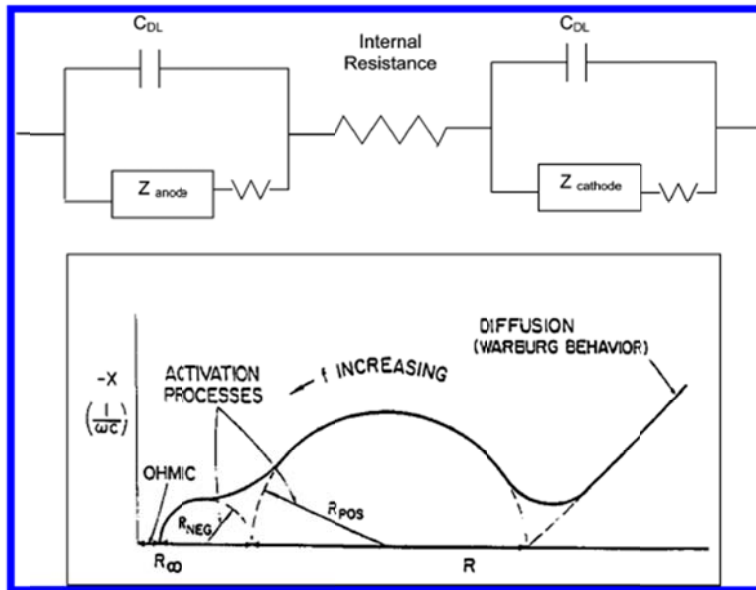


Figure 2.12 (A, top) Simple battery circuit diagram, where C_{DL} represents the capacitance of the electrical double layer at the electrode-solution interface. Z_{anode} and $Z_{cathode}$ are the impedances of anode and cathode reactions and sometimes might be considered as a series resistance capacitance with values derivative from the Argand diagram. This reaction capacitance can be 10 times the size of the double-layer capacitance. The reaction resistance component of Z is related to the exchange current for the kinetics of the reaction. (B, bottom) Argand diagram of the battery circuit diagram for an idealized battery system. The characteristic behaviors of ohmic, activation, and diffusion or concentration polarizations are represented. [40].

Each electrode reaction shows a specific, characteristic impedance sign. Ideally, the semicircle in the mid-frequency region is related to charge transfer reactions (activation processes) that is indicative of relaxation processes; the diffusion processes (concentration processes) show a line with 45° angle which often denoted as Warburg element and ohmic components are independent of frequency. The maximum frequency, f_m , of the semicircle indicates the relaxation time ($T = 1/f_m = RC_p$). Where R is related to the exchange current for the reaction; C_p is called the polarization capacitance which is typically about $200 \mu F/cm$; ~ 10 times larger than the capacitance of the EDL. Battery exhibit large capacitances of farads due to their large surface areas with a resistance of milliohms.

The variation of the cell impedance at various frequencies demonstrates the behavior of the electrolyte, electrodes and interfaces, and also the diffusion mechanism taking place in

the cell. Although the interpretation of the diffusion mechanism is complicated, the comparison of the cell behavior with existing standard models would provide an insight about the nature of the reactions. Fig.2.13 Shows the Nyquist plot of a LiCoO_2 electrode and its typical equivalent circuit used to fit the electrochemical impedance spectroscopy curve [41]. The measured resistance at the high frequency region corresponds to the resistance of the ionic electrolyte R_s . It is added in series to the rest of the circuit. The parallel resistance and the capacitance of the SEI layer are represented by R_{sei} and Q_{sei} (Constant Phase Element, CPE) respectively. They are related to the Li^+ migration through the SEI layer. The charge-transfer resistance (R_{ct}) and the capacitance of the double layer (Q_{dl}) on the particle surface are represented in the middle frequency region. The bulk diffusion of lithium ions in the low frequency region is represented by a CPE (Q_{d}). Also the same approach has been followed for the LiM_xO_y ($M = \text{transition metals}$) and other active electrode materials, showing a good agreement with the experimental data [42].

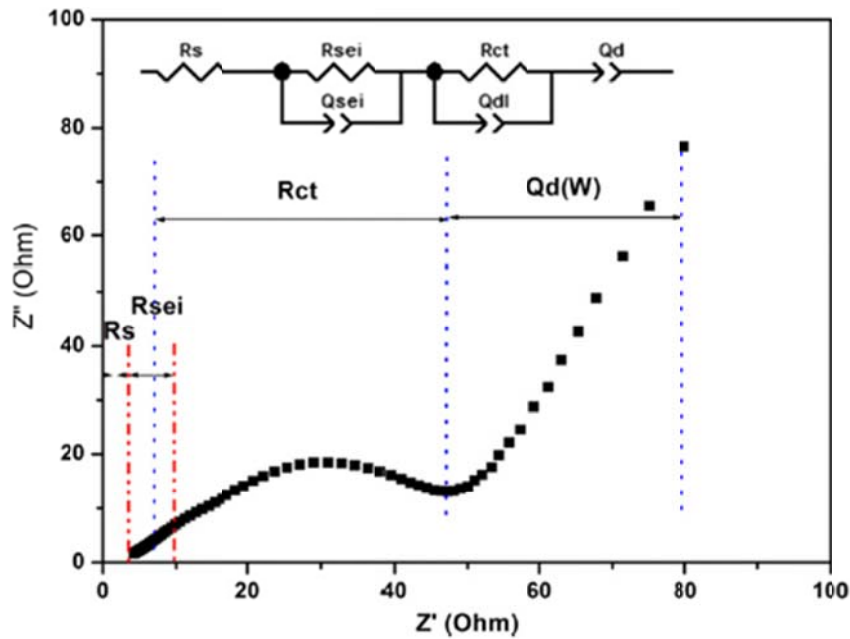


Figure 2.13. Electrochemical impedance spectroscopy (EIS) measurement and the equivalent circuit of the cathode half cell (LiCoO_2) [41].

2.5. Raman spectroscopy

2.5.1. The principles of infrared and Raman spectroscopy

All molecules are bonded together by chemical bonds with the flexible length and angle in between; therefore any change in the equilibrium position of the molecules leads to the vibration of molecules about their equilibrium states. Since the vibrational states of the molecules vary as a function of strength and geometry of the chemical bonds, it can be utilized for characterization of the bonds. There are three principal methods for study of vibrations between the molecules: infrared (IR) spectroscopy, Raman spectroscopy and inelastic neutron scattering. The electromagnetic field light is employed for the first two methods while the latter uses neutrons as the probe. IR and Raman spectroscopy are more popular techniques since they are simpler and cheaper ones.

The electromagnetic radiation at appropriate frequency can be absorbed (IR spectroscopy) or being scattered (Raman spectroscopy) by molecules. Absorption happens when the frequency of the irradiated light (in the infrared region of electromagnetic spectrum) is exactly the same as the normal modes of vibration. The absorbed energy can later be released either by heat (phonon) or re-radiation. This mechanism is employed in infrared (IR) spectroscopy by passing the infrared radiation through the sample. The frequency and the fraction of absorption in the IR spectrum indicate the normal vibrational modes of the molecules of the sample.

Scattering of the electromagnetic beam might be elastic, without frequency change, or inelastic with the change of frequency. Elastic scattering is called Rayleigh scattering which might occur either from inhomogeneities or in a homogeneous medium even without any molecular vibration. The Raman scattering is an inelastic scattering with a higher or lower frequency than the frequency of the incident beam. The change in the frequency is equal to one of the modes of vibration of the molecules. The scattering with higher frequencies is called Anti-Stokes Raman scattering and the one with lower scattering frequency is named Stokes Raman

scattering. The Stokes Raman scattering is stronger than Anti-Stoke scattering [43]. The transition between the vibrational states is presented in Fig. 2.14.

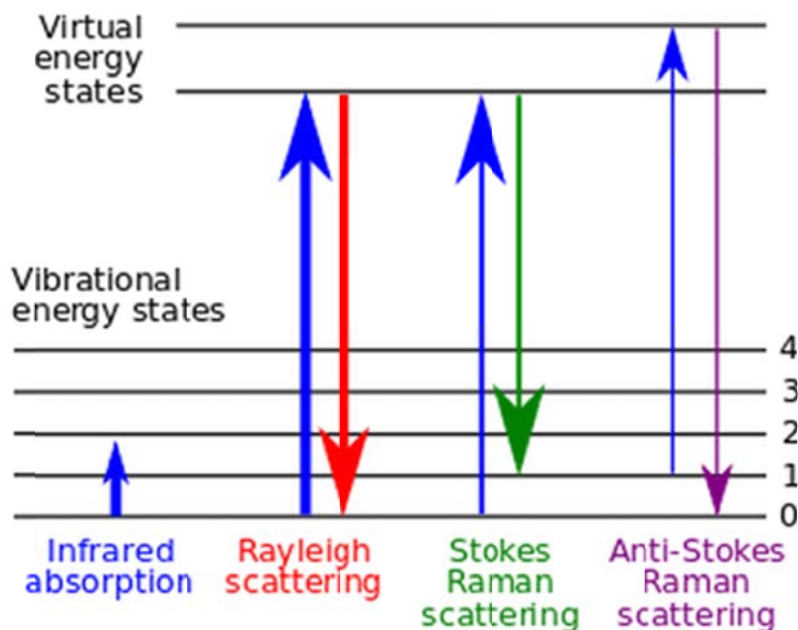


Figure 2.14 Schematic vibrational energy levels and correspond transitions. The thickness of the arrows are indicative of the signal strength of the transitions.

The vibrational modes can be classified in four types: Stretching (ν), in planar bending (δ), Out-of-planar bending (γ), and Torsion (τ) vibrations. The vibration frequency depends on the types of vibration and decreases with increasing the number of involved bonds. Although, large molecules like polymers might present special types of vibration, the vibration can be derived from the four mentioned types of vibration [44].

Depending on the symmetry of the molecule, all the vibrational modes are not active and the active modes in Raman and IR spectroscopy are called Raman-active and infrared-active modes. Therefore, the IR and Raman spectroscopy are complementary methods for getting the maximum possible amount of information. However one of the methods might be more useful for a particular application. Although the principles of infrared and Raman spectroscopy are complicated, simply speaking the IR-active modes of a molecule possess an

oscillating electric dipole moment while the Raman-active modes should have a oscillating electrical polarisability [43].

2.5.2. Application of Raman spectroscopy in the characterization of Li-ion batteries

Raman spectroscopy is a sensitive characterization technique to investigate the structural properties of both electrodes and the electrolyte solutions in the lithium ion cell. Many research groups have utilized Raman spectroscopy to study the surface phenomena of the electrodes [45, 46], and also the structure of the electrolyte systems including ion-ion and ion-solvent interactions in aprotic media [47-49]. Different approaches have been attempted for data acquisition and analysis[50, 51]. Despite recent significant advances, extraction of the relative information from the electrodes, which have been examined primarily ex-situ, still remains a challenge due to the evolving environmental conditions and non-equilibrium reactions occurred during the characterization[50]. In-situ Raman spectroscopy is a direct spectroscopic technique which provides structural and chemical information in batteries and opens up a new venue for real-time investigation of dynamic reactions evolving at the interface between the cell components.

2.5.2.1. Raman spectroscopy of the electrolyte

The ionic structure of the electrolyte and the ion-solvent interaction for different salt systems at various concentrations are very important since they provide useful information for the optimization of the electrolyte systems. Spectroscopic studies of the molecular structure of the lithium salts and organic solvents along with different conventional liquid electrolyte systems have been reported by several research groups [27, 49, 52]. The Raman shift varies based on the concentration and type of the dissolved salt in the electrolyte [27]. Since the conductivity of the electrolyte is proportional to the salt concentration (session 2.1.2), the correlation between the conductivity and the Raman shift can be concluded.

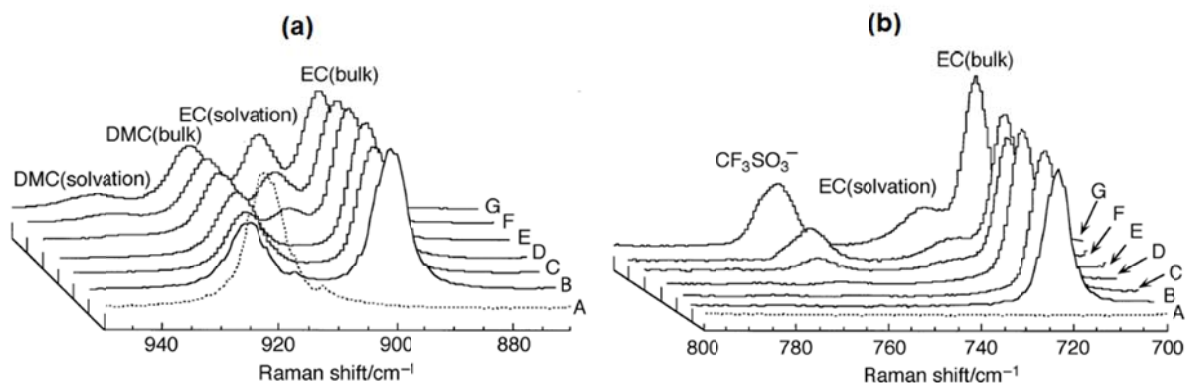


Figure 2.15 (a) Raman spectra for symmetric stretching vibration band of C–O single bond and (b) the symmetric ring deformation of EC in the LiCF_3SO_3 system. (A) Solvent DMC, (B) solvent EC+DMC (50 : 50 by volume), (C)-(G) EC+DMC dissolving LiCF_3SO_3 (C: 0.05, D: 0.1, E: 0.5, F: 1.0, G: 1.5 mol dm^{-3}) [27].

Lithium ions interact with the solvent molecules even in the mixed solvent systems of common electrolyte solutions like: (EC+PC/ LiClO_4), (DMC+EC/ LiPF_6) and (DMC+EC/ LiCF_3SO_3) [27, 49]. The interaction of lithium ion with the solvent molecules leads to a shift to higher wave numbers in the Raman spectra of the bulk solvent. Fig.2.15. shows the Raman spectra of the (DMC+EC/ LiCF_3SO_3) electrolyte system at different salt concentrations. Lithium ions interact with the solvent molecules and affect the solvent bonds including C–O and C=O bonds.

The interaction of lithium ions with the solvent molecules produces solvation bands as the concentration of the salt increases. The bands at about 900cm^{-1} and 920cm^{-1} are related to symmetric stretching vibration band of C–O single bond in EC and DMC molecules. As the salt concentration increases, the EC and DMC solvation bands (C–O single bond) form at the wave numbers of 905cm^{-1} and 930cm^{-1} , respectively, as shown in Fig.2.15 (a). The band at about 720cm^{-1} corresponds to ring-C=O bending mode in Fig.2.13 (b). By increasing the salt concentration, the interaction between the Li^+ cations and EC molecules leads to the formation of the EC solvation band at higher wave numbers (730cm^{-1}) adjacent to the correspond bulk

bands. The band at about 760 cm^{-1} is assigned for the combined SO^{-3} and CF_3 groups of the CF_3SO_3^- anion [53, 54]. It provides information about ion-ion interaction (ion association), ion-pair and ion-aggregates [53] between Li^+ and CF in high concentrated electrolytes. The relative intensity is defined by Eq.2.10.

$$I_r = \frac{I_s}{I_s + I_n} \quad (2.10)$$

where I_r is the relative intensity, I_s and I_n are intensity of the solvated and non-solvated molecules respectively. The concentration of dissolved salt has a linear relationship with the relative intensity Fig. 2.16.

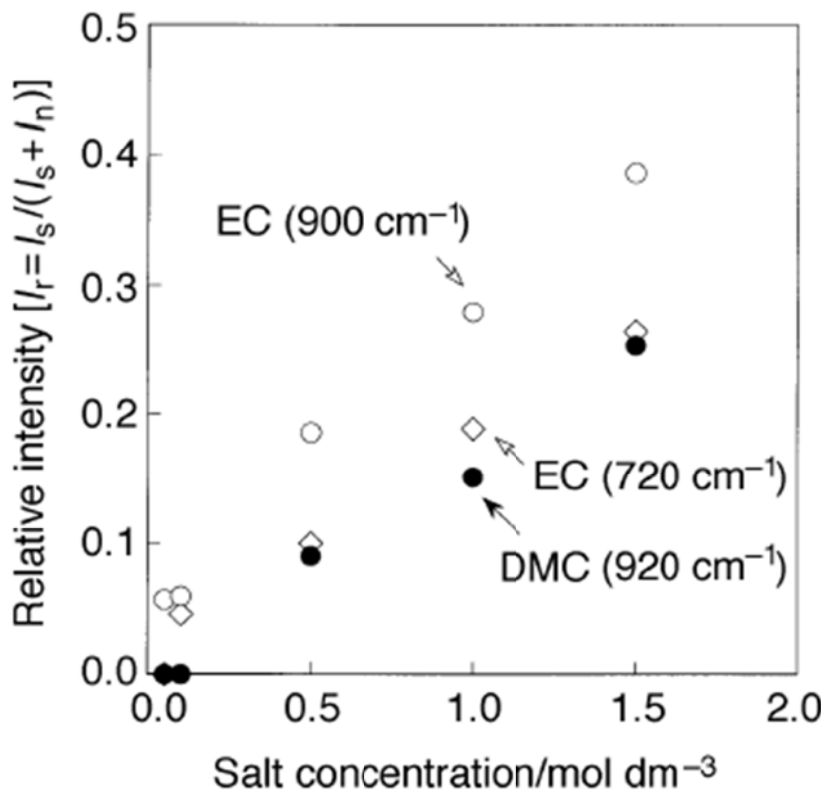


Figure 2.16 The variation of the relative intensity with salt concentration change in the $\text{LiCF}_3\text{SO}_3/(\text{EC}+\text{DMC})$ system. EC (720 cm^{-1} (\diamond)), (\circ) EC (900 cm^{-1}), (\bullet) DMC (920 cm^{-1}) [27].

2.5.2.2. Raman spectroscopy of the active material

The surface reactions of the electrodes can also be studied by Raman spectroscopy. The Raman mapping technique has been used for the characterization of LCO cathodes and MCMB anodes[51]. It provides compositional distribution of a wide area on the surface of the electrodes. The compositional distribution can be explained by band position, line widths, and intensity ratios in the mapping technique. On the cathode side, the distribution of LCO and carbon additive as well as the corresponding properties was investigated. Fig.2.17 (A) and (B) shows the typical Raman spectra obtained from the LCO cathode along with the spectra of four different cathodes. The A_{1g} and E_g bands are indicative of $LiCoO_2$; the D, G and 2D bands correspond to the carbon additive. As only oxygen atoms involve in the A_{1g} vibrational mode, it is useful for the description of $LiCoO_2$ properties. Also the amount of lithium in the crystal structure is determined by the band position of A_{1g} . The intensity ratio of $I_{A_{1g}}/I_{2D}$ has been utilized to determine the distribution of the $LiCoO_2$ in the cathode. Also $I_{E_g}/I_{A_{1g}}$ was assigned to the orientation of the LCO crystallites on the surface of the cathode. I_D/I_G is indicative of disordered carbon to ordered graphitized carbon and the line width of the carbon bands define the type and quality of the carbon additive. Different cathodes show specific distribution of vibrational modes regarding their special composition (Fig.2.17B).

The same approach was implemented for the anode side (Fig.2.17C). Raman mapping of the MCMB anode was employed to calculate the distribution of correlation length (L_a) using Eq. 2.11.

$$L_a = \frac{1}{[I_D/I_G] \times 22.82/100} \text{ nm} \quad (2.11)$$

L_a is indicative of the structural order in the plane of graphite sheets in carbonaceous material[51].

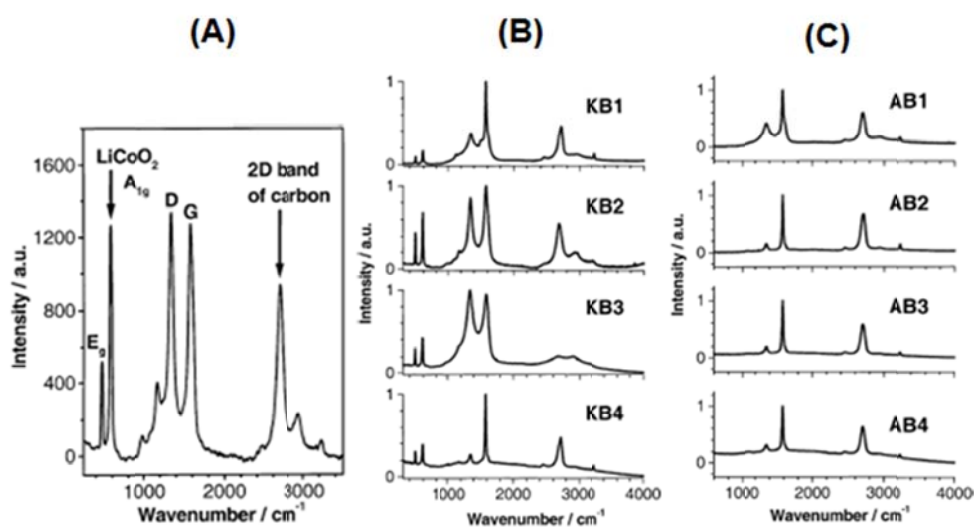


Figure 2.17 (A) Average Raman spectra of an LCO cathode sheet. (B) Raman spectra of four different cathode and (C) anode sheets calculating by averaging the individual spectra of a mapped area on the surface of the electrodes [51].

Mapping the anode surface for calculating the average distribution of L_a is similar to calculation of intensity ratio of I_D/I_G to define how disordered and ordered carbon variety on the surface. Also average line width and intensity of the bands varies for different samples. Since the compositional distribution of each electrode is unique, the spectra act as the finger print of the corresponding electrode which is suitable for distinguishing special properties and quality control application.

LiFePO_4 shows two active ν_1 (950 cm^{-1}) and ν_2 ($1000 \sim 1070 \text{ cm}^{-1}$) vibrational modes corresponding to symmetric and anti-symmetric stretching modes [55]. The bands are intermolecular vibrations of PO_4 groups which are sensitive to the existence of lithium ions in the unit cell [56]. Therefore, the extraction or insertion of lithium ions to the unit cell during charge and discharge can be detected by probing ν_1 and ν_3 modes. As has been reported, ex-situ Raman study of Li_xFePO_4 ($0 \leq x \leq 1$) showed that reducing the lithium content, x , from 1 to 0.75 slightly changed the peak profile of the 950 cm^{-1} band and also generated new weak bands at about ($911, 1000\text{-}1050 \text{ cm}^{-1}$) [55]. Several bands of FePO_4 ($911, 960, 1124, 1064$ and

1080 cm^{-1}) occur at significantly different intensities and wavenumbers than those of LiFePO_4 (Fig.2.18).

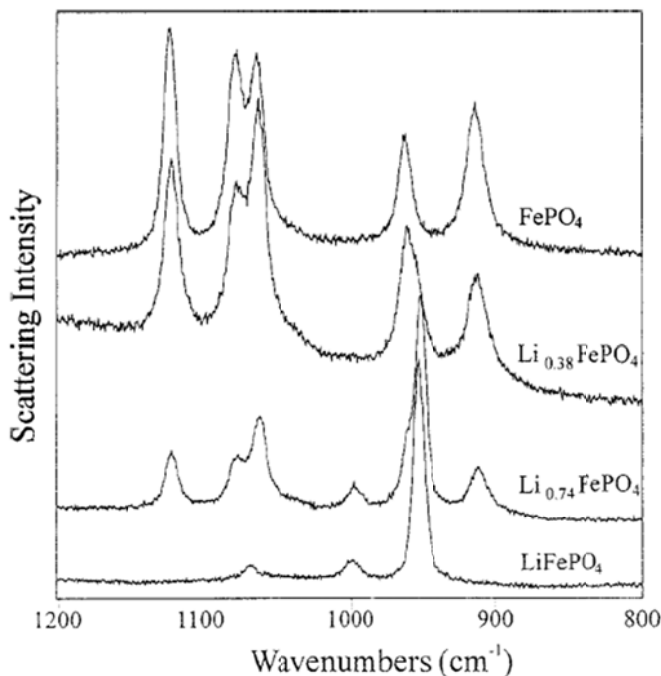


Figure 2.18 Variation of ν_1 and ν_3 modes in the Raman spectra of Li_xFePO_4 ($0 \leq x \leq 1$) [55].

The effect of laser power on the Raman spectra of two carbon-coated nano-powders of LiCoPO_4 and LiFePO_4 olivine cathode materials has also been reported [57]. Exposing the Raman laser beam to the surface of LFP cathode might lead to decomposition of LiFePO_4 according to the following equation,

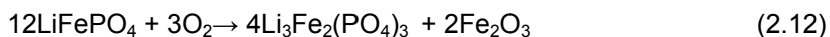


Fig.2.19 shows the laser power effect on the Raman spectra of C- LiFePO_4 cathode. In addition to decomposition of LiFePO_4 , carbon gasification also occurs which leads to the change in the intensity and profile of the G and D bands of carbon. As laser power increases the decomposition proceeds even without the existence of oxygen (in helium atmosphere). In this case the required oxygen for the oxidation reaction comes from the decomposition of

phosphate groups in lithium iron phosphate. The peaks at 217, 277, 395, and 600-650 cm^{-1} are assigned to iron oxide, from the decomposition of LiFePO_4 .

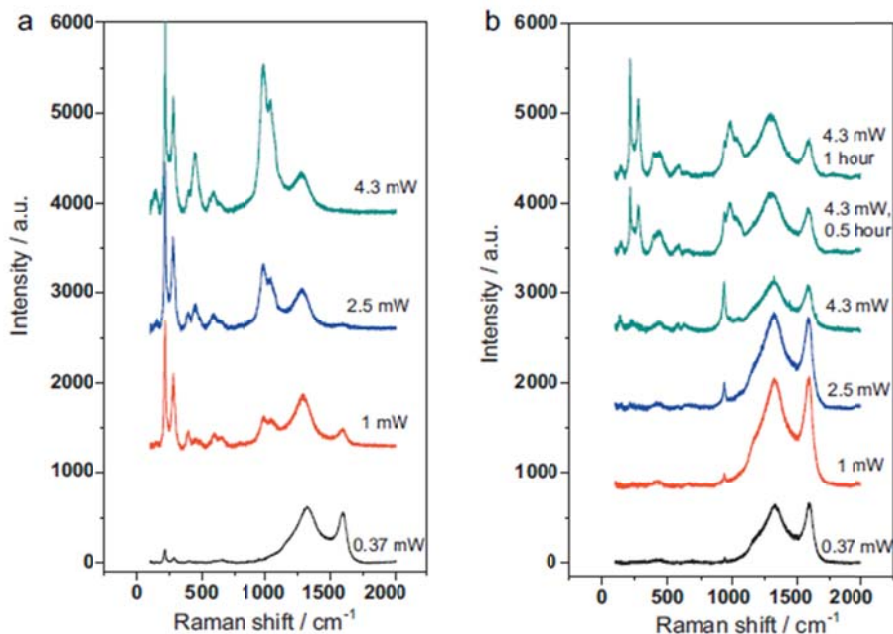


Figure 2.19 The collected Raman spectra of LiFePO_4 carbon coated olivine powder at different laser powers. He-Ne (633cm^{-1}) laser source was utilized (a) in air and (b) in helium (99.99%)[57].

Since ex-situ Raman spectroscopy provides information of equilibrated situations of the cathode, extracting correct non-equilibrated information and applying to real situations of working electrodes are challenging. Battery components undergo a relaxation procedure after opening the battery for ex-situ study. Despite the relaxation procedure, as mentioned before laser power affects LFP materials which required additional care and is not considered in some studies. Fig.2.20 shows the result of ex-situ Raman spectra of C- LiFePO_4 at various states of charge [58]. As mentioned before, the iron oxide bands have been probably generated due to the decomposition of active material during the ex-situ Raman experiment which may not exist at real time situations.

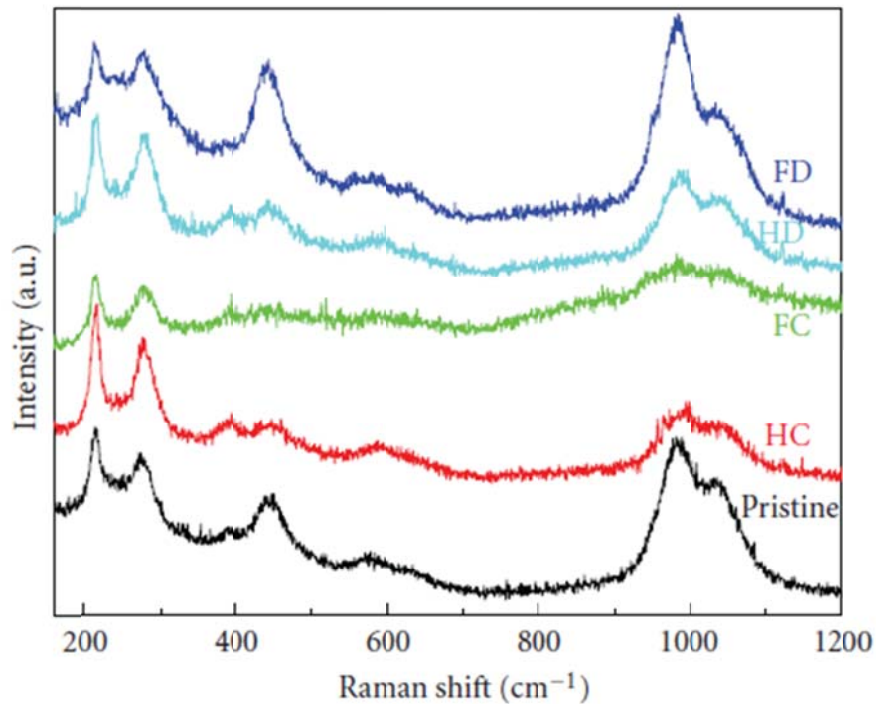


Figure 2.20 Raman spectra of C- LiFePO₄ powder at various stages of charge – discharge process (half charge (HC), full charge(FC), half discharge(HC) and full discharge(FD)) in frequency range 150 to 1200 cm⁻¹[52].

In-situ Raman study of the electrodes provides a real time picture of the complex situations taking place in the batteries. However, investigation about surface reaction of C-LiFePO₄ cathodes at working condition has been a challenge. Since the penetration of the Raman laser beam to the surface of the LiFePO₄ particles is blocked by the carbon coating, detection of ν_1 mode of LiFePO₄, which is inherently an intense peak, is difficult [59]. In addition to the carbon coating, the existing electrolyte diminishes the intensity of ν_1 mode coming from LFP.

2.5.2.3. Raman spectroscopy of the conductive carbon

Construction of the electrodes requires addition of carbon additive for making supportive and electronically conductive network between the particles. Therefore, both quality and quantity of additive carbon affect the performance of the battery. The evaluation of carbon

is reported by considering structural factors such as sp²/sp³ ratio and disordered/graphene (D/G) determined by Raman spectroscopy, and H/C ratios determined from elemental analysis which strongly influence the conductivity and rate behavior. Hydrocarbons are usually used as the source of carbon, and a better decomposition of the carbon sources, leads to lower H/C ratios in the final product with higher conductivity [60].

Crystalline graphite has a layered structure and shows a high electrical conductivity in the basal planes which are held together with weak Van der Waals inter-planar forces. Single crystal graphite belongs to the D_{6h}^4 symmetry group, and vibrational modes are of the types $2E_{2g}$, $2B_{2g}$, E_{1u} , and A_{2u} (see Fig. 2.21). [61] The two E_{2g} modes are Raman active and have been identified by the Raman band at 1582 cm^{-1} and a low-frequency neutron scattering feature at 47 cm^{-1} ; while the E_{1u} (1588 cm^{-1}), and A_{2u} (868 cm^{-1}) are IR active and observable using IR reflectance. The B_{2g} modes are optically inactive, but have been observed by neutron scattering at 127 cm^{-1} . Highly ordered pyrolytic graphite (HOPG) exhibits only the 1582 cm^{-1} band in the region between 1100 and 1700 cm^{-1} , but also shows second order features between 2400 and 3300 cm^{-1} [61].

When the microcrystallites size of the graphite decreases ($L_a < 1000\text{ Angstrom}$), a new feature which is called D band appears at about 1360 cm^{-1} . Although the origin of D band has been the subject of many controversies, it is usually assigned to the A_{1g} mode that is associated with the symmetry breakage at the edges of graphite sheets [60, 61]. Therefore, as the size of microcrystallites decreases, the D band character would be more pronounced.

Carbonaceous materials form in different degree of graphitization and generally the E_{2g} mode of crystalline graphite tends to be broaden and form G band character (at about 1590 cm^{-1}) as the degree of graphitization decreases. D band is an inherent nature of graphite which always contains different degree of symmetry breakage of basal planes.

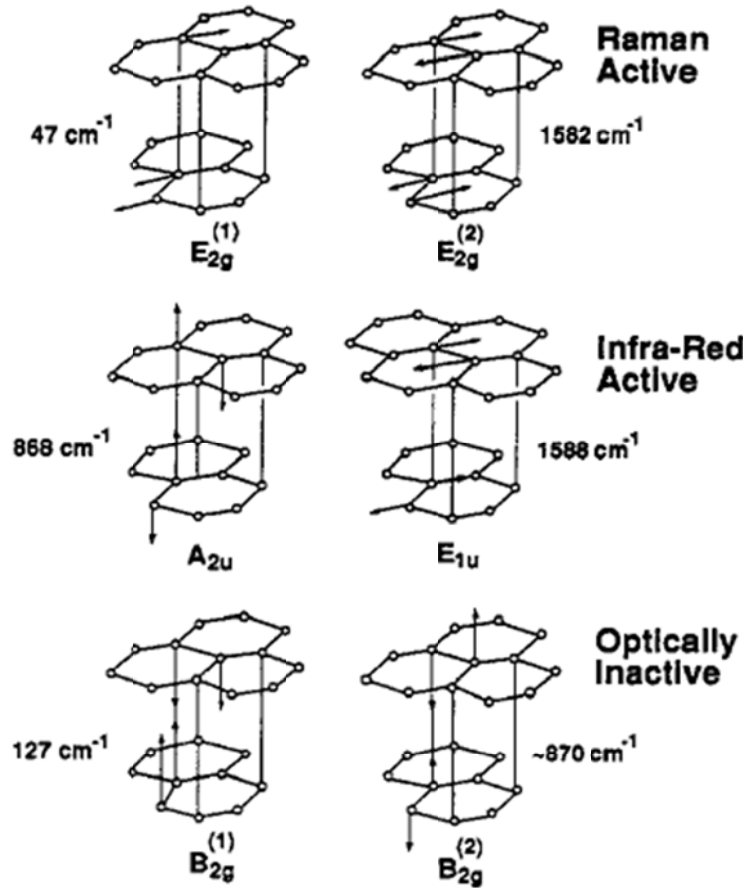


Figure 2.21 Vibrational modes for single-crystal graphite. The B_{2g} frequency is predicted but not yet observed experimentally[61].

The variation of the width and intensity of the D and G bands is related to the growth and the size of different carbon phases, the presence of functional groups, and impurities. The G band tends to broaden and shift toward higher frequencies with decreasing intraplanar (L_a) and interplanar (L_c) microcrystallite dimensions [60]. The empirical linear relationship between $1/L_a$ and D/G is a useful means to determine the average L_a for a given carbon sample.

Fig. 2.22 shows the Raman spectra of different types of carbons. A Gaussian peak fit was applied for spectra deconvolution and to minimize the error with four fitting bands considered.

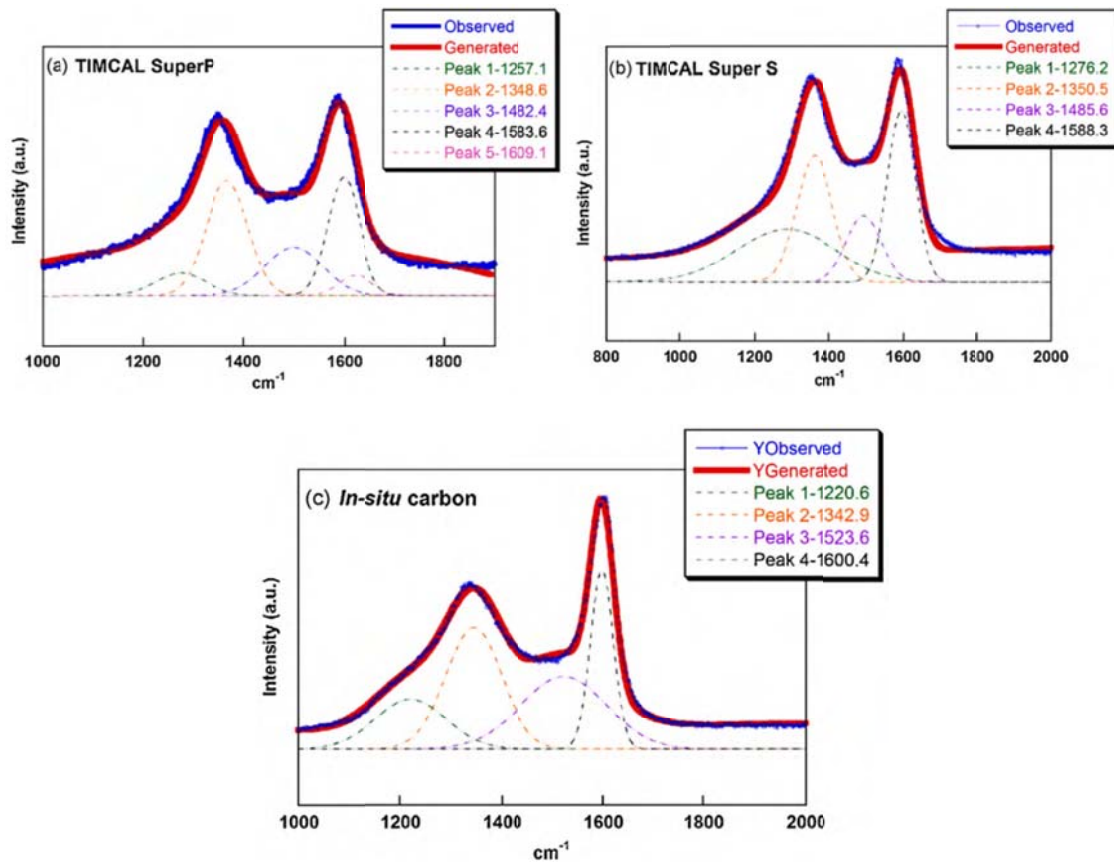


Figure 2.22 Raman spectra and spectrum deconvolution of (a) TIMCAL Super P, (b) TIMCAL Super S, and (c) in-situ carbon[62].

The four fitting bands are located at 1200, 1347, 1510, and 1585cm⁻¹ in the spectra; however, the position and intensities are dissimilar. The bands at 1194 and 1510cm⁻¹ have been reported for short-range vibrations of sp³-coordinated carbons (highly disordered carbon). [60, 63]. The integrated areas were calculated for all bands and used to define sp³ / sp² ratios. The result was similar for the commercial samples while the in-situ carbon shows a higher disordered carbon. The C- LiFePO₄ cathodes with different types of carbons show enhanced electrochemical performance as composite content increases. However, a significant increase in carbon content reduces the specific capacity of the electrode.

The optical skin depth of the Raman laser beam to the electrode material diminishes as the conductivity of carbon additive increases according to the following equation,

$$\delta = \frac{c}{\sqrt{2\pi\mu\sigma\omega}} \quad (2.13)$$

where σ is the electrical conductivity of the samples, μ is the permeability and ω is the optical frequency and c is the light speed [64]. Since ω is proportional to the reciprocal of the laser wavelength, using higher wave length increases the penetration depth. The position of the D band has been reported to shift from 1360 cm^{-1} to 1330 cm^{-1} when the wavelength of Raman laser (λ) was increased from 488nm to 647nm. Variations in λ , changes the Raman skin depth leading to variation in the spectrum if the carbon[61].

CHAPTER 3

EXPERIMENTAL

3.1 Introduction

Batteries generally have a simple structure. They are made up of cathode or positive electrode, anode or negative electrode, an ionic conductive medium as the electrolyte, and separator, a porous layer without electronic conductivity, between the electrodes. Despite the simplicity, utilizing the optimum operating condition requires considering many details that might affect the chemical reaction of the cell. Especially in secondary or rechargeable batteries, complex reactions might happen during different working conditions. Therefore, to prevent any inappropriate reactions during cycling, the preparation of the components and assembling procedure must carry out in a perfectly controlled condition. The lithium ion batteries are very sensitive to the presence of moisture or oxygen as the reactive lithium immediately reacts with even a small amount of oxygen or water in the li-ion cell. Besides, the irreversible reactions of LiPF_6 -based electrolytes and moisture generate HF in the electrolyte and also produces inorganic solid electrolyte interface (SEI) on the anode surface. As a result, energy density loss and safety concerns arise, and careful attention is required to prevent the unfavorable consequences.

3.2 Making the li-ion battery

3.2.1. Preparation of the cathode

Solid-state method was employed to synthesize carbon-coated LiFePO_4 particles in a two-step heat treatment up to $700\text{ }^\circ\text{C}$ in an argon atmosphere [12]. Carbon coated LiFePO_4 was used as the active material, graphite and carbon mixture (Timcal Super P Li) and poly

vinylidene fluoride (PVDF, Kynar, HSV900, Elf-Atochem) were used as the conductive material and binder, respectively. Different compositions of C-LiFePO₄, conductive carbon, and binder were mixed thoroughly in 1-Methyl-2-Pyrrolidinone (NMP, Acros Organics) for 12 hours to form a homogenous paste. The resultant paste was coated on top of an Al foil using a doctor blade (Gardco) and then dried in an oven at 120 °C. The cathode was cut and some of them were pressed and then dried at 120 °C for 48 hours. The maximum thickness of the applied paste was adjusted vs. the amount of the carbon in the composition of the cathode. The maximum blade gap of 15 and 20 were utilized for the cathode with 20 and 10 wt% carbon respectively because the cathodes with higher blade gaps generate cracks after drying. The surface of the Al foil was rubbed with a HB pencil and then wiped carefully to put a thin layer of graphite onto the Al foil and prevent the detachment of the cathode material from the Al foil after pressing. The composition and applied pressure of the cathodes are summarized in table 3.1.

Table 3.1. The composition and the processing conditions of different cathodes. LiFePO₄ is made by using the solid state method [12].

Code	C-LiFePO ₄ (A) (wt%)	Binder (B) (wt%)	Carbon additive (C) (wt%)	Blade gap	NMP/(A+B+C) (wt/wt)	Pressure Kg/cm ²
C2	90	8	2	15	2.5	500
C10n	80	10	10	15	2.9	0
C20n	65	15	20	10	3.25	0
C10	80	10	10	15	2.9	500
C20	65	15	20	10	3.25	500
C10p	80	10	10	15	2.9	2500
C20p	65	15	20	10	3.25	2500
R	90	8	2	15	2.5	500

The coating procedure was carried out on a pre-punched Al foil for making the cathode of the in-situ experiment that is explained in chapter 4. The holes ($d \approx 0.3\text{mm}$) through the foil were made with a set of pins that was fixed with an epoxy resin (Fig. 3.1 A). The Al foil was punched by applying a slight pressure against a soft polymer base and after the coating & drying, the extra material in the back of the foil was removed carefully (Fig. 3.1 B).

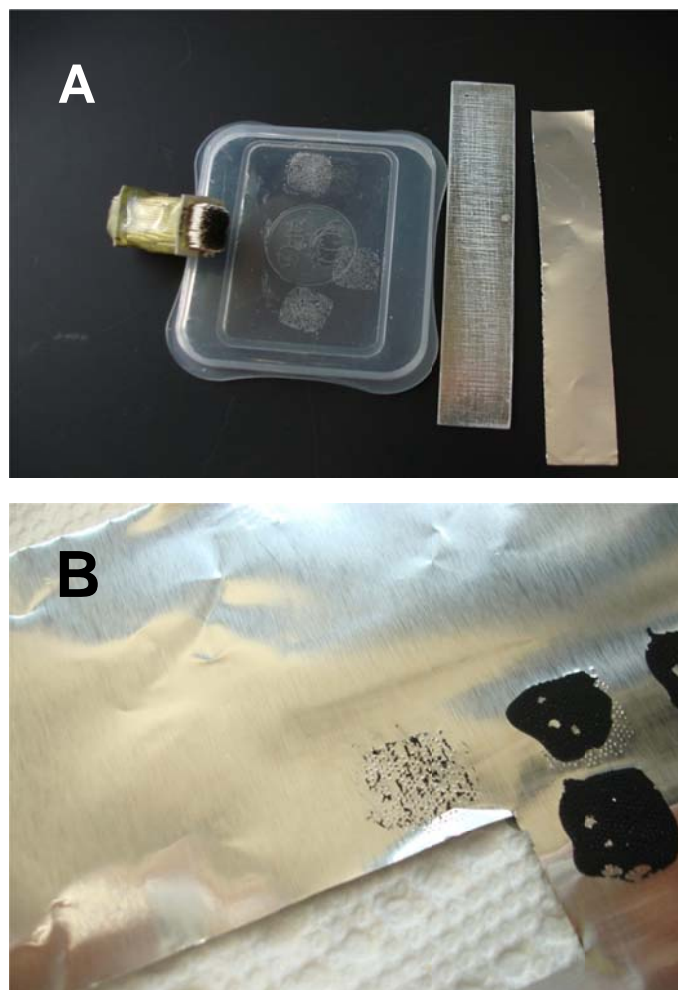


Figure 3.1 (A) The pin set was used to make tiny holes through the Al foil. (B) the extra material removed from the back of the coated foil.

3.2.2. Preparation of the anode

Lithium metal was utilized as the anode of the li-ion cell. The preparation of the anode was performed inside a glove box (MBROUN) to prevent oxidation of the lithium. A steel mesh (100 meshT316, Industrial Netting) was used as the current collector. It was cut, sonicated in acetone and dried before being transferred to the glove box. Lithium foil (1.5mm, Sigma Aldrich) was cut by a scissor and was scratched on one side by a spatula to remove the oxide layer. The

shiny surface was pressed against the steel mesh between two steel plates by using a clamp. The other surface of the lithium was also scratched to reach the shiny surface and after trimming, the set was used as the anode of the li-ion cell. The area of the lithium metal was selected to be two times of the area of the cathode for all of the cells.

3.2.3. *Electrochemical cell design*

Fig.3.2 shows the design of the cases for electrochemical tests. The electrolyte reservoir was made by glass. The transparent feature of the reservoir provides optical access to the component of the cell so that conditions like corrosion of the current collectors or generation of gas can be easily detected. An epoxy connector was designed for making thread to tie up the cap at the end of the reservoir. The connection terminals were made by steel inside the epoxy connector. The cell was cleaned to remove any excessive epoxy inside the reservoir and placed in an oven at 80 °C for six hours for the polymerization of the epoxy. A stand was made for the case to maintain the structure vertically and prevent penetration of the electrolyte to the terminals. The cell was dried at 80 °C overnight and transferred to the glove box for assembling the Li-ion battery. The type A case was designed initially in which the case reservoir had a narrow slit so that the thickness of the two electrodes and the separator matched with the reservoir slit width (Fig.3.2 A). The B type case with wider slit was made to facilitate the assembling procedure Fig.3.2(B). To assemble the battery components in the type B case, the cathode, separator and anode were placed in between two thin glasses and the set were put inside the case. A piece of PTFE tape was used to make the electrodes in touch with separator and finally after fixing the connections in place, the electrolyte was added. Also the same approach was followed to design and make a case with three terminals for the Cyclic Voltammetry (CV) test.

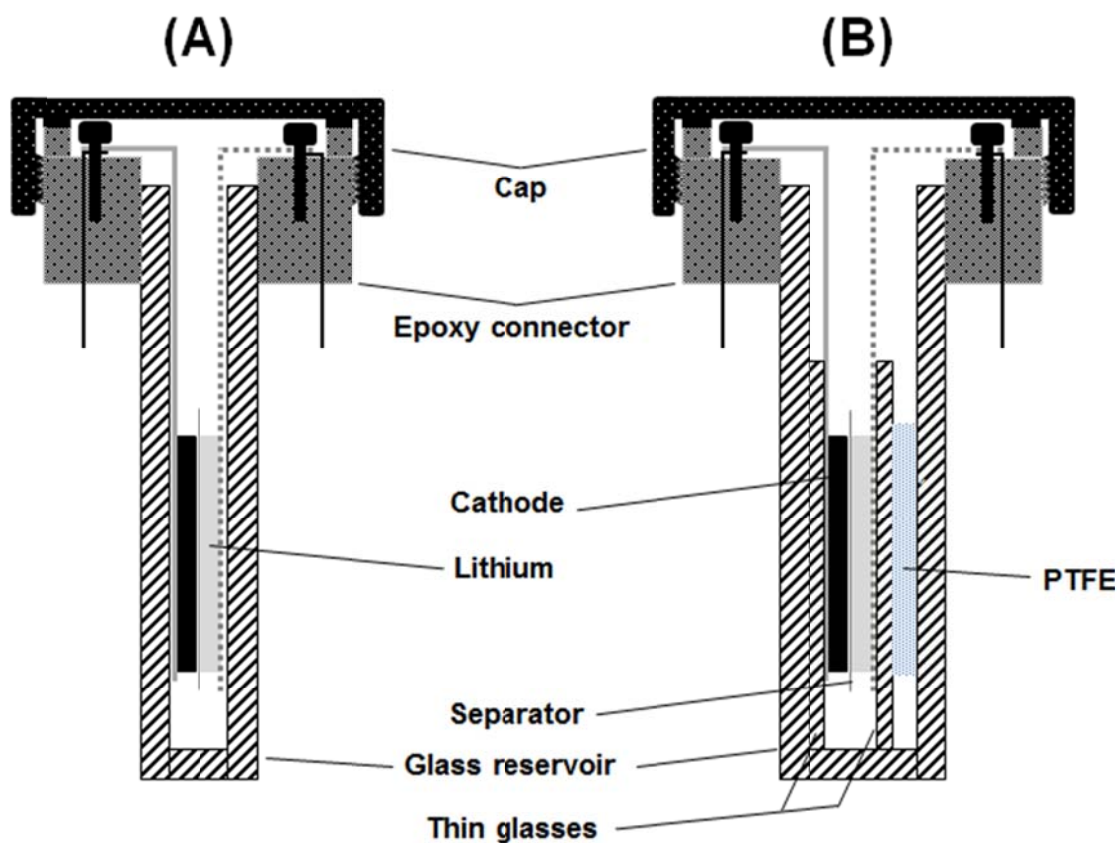


Figure 3.2 Schematic representation of li-ion experimental cell

Fig.3.3. shows the glass reservoir and the epoxy connectors that were made separately for assembling the B type cases. To make the epoxy connectors, a prototype of the designed connector was made, and then RTV silicon was used to make the mold for the epoxy connectors. The silicon rubber mold was used for making multiple epoxy connectors by using epoxy resin.

3.2.4. Preparation of the electrolyte

A mixed solvents EC+DMC (1:1 by volume, Sigma Aldrich) containing 1.0 M LiPF_6 (Sigma Aldrich) was utilized as the electrolyte. The anhydrous EC and DMC and the LiPF_6 salt were stored inside the glove box to prevent any contamination by the moisture. EC is a transparent solid at room temperature with the melting point of 34-37 °C and should be warm up

inside the glove box and then the solution was added to the LiPF_6 . The electrolyte was stored inside the glove box and stored away from the sun light. The presence of a small amount of moisture in the electrolyte is inevitable, and every time by opening the container, even inside the glove box, the water content might increase slightly. Hence, usage of the remaining electrolyte after a few weeks was discontinued and again fresh electrolyte was made.



Figure 3.3 The glass reservoir and the epoxy connectors were made separately and then attached together to form the complete structure of the B type cases.

3.2.5 Assembling the cell

The cell was assembled inside the Argon filled glove box. A gas purification unit was used for absorbing the moisture and oxygen inside the glove box. The atmosphere of the glove box was circulated through the gas purification unit to reduce the moisture and oxygen of the box. The circulation was run for a few hours before starting the work. Separator, paper towels and all things that might grasp moisture from the ambient atmosphere were stored inside the

glove box to reduce the contamination. The atmosphere of the glove box was checked by exposing the shiny surface of a fresh cut lithium metal to the atmosphere. Any color change on the surface was indicative of the contamination with water or oxygen, and then more circulation is required to reach a good working atmosphere.

3.3. Electrochemical behavior

3.3.1 CV test

The cyclic voltammetry test was performed in a transparent cell with three electrodes (Fig.3.4).

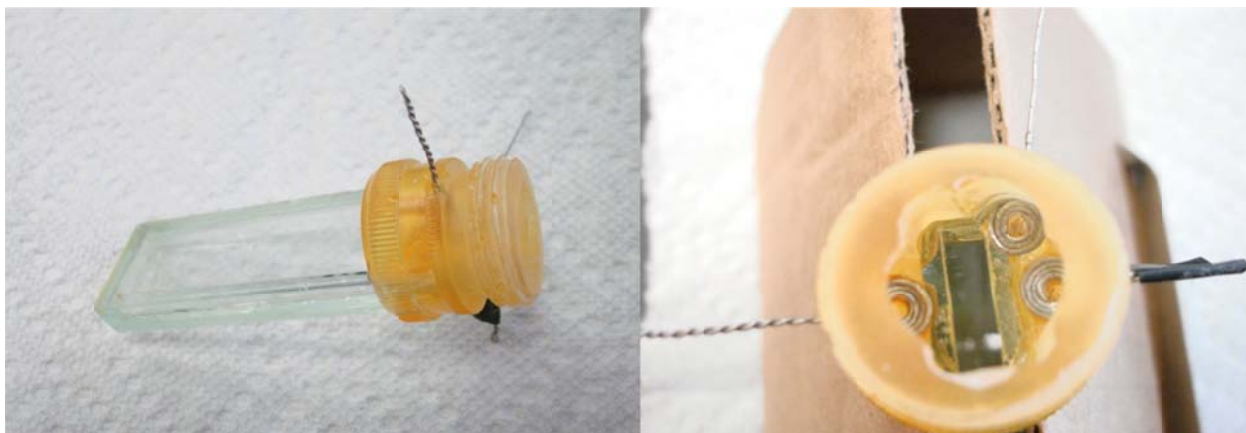


Figure 3.4 The transparent cell with three connection terminals, used for the CV test.

The working electrode placed inside the case with the composition of C10 which is mentioned in the table 3.1. Lithium metal was pressed against the steel mesh and used for both reference and counter electrode. Two separators were used to prevent short circuit between the components of the cell. The electrolyte composition is mentioned in section 3.1.3. The scan rate of 1mV/sec applied during the five cycles and the potential of the reference lithium selected as 0.005V. The CV results for the first five cycles after making the cell is demonstrated in Fig.3.5.

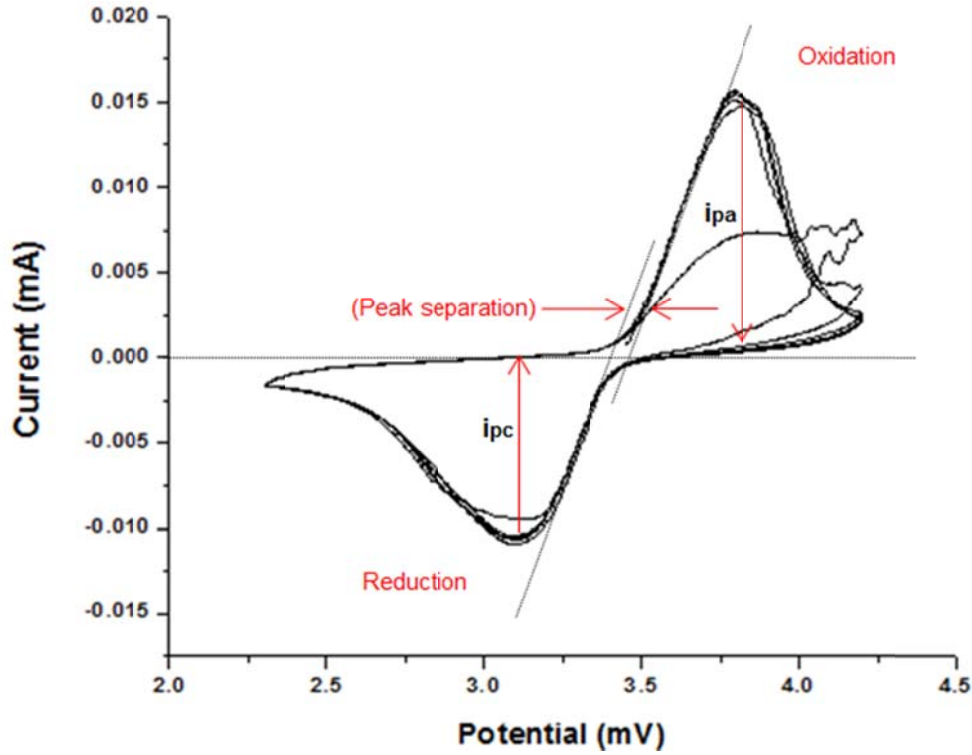
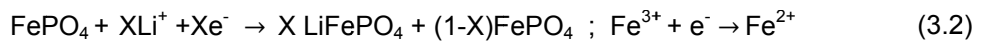
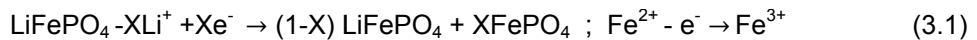


Fig.3.5 The cyclic voltammetry test for the first five cycles after making the cell.

CV plots (or diffusivity plot) can be used to define a Li-ion cell respond to various charge/discharge rates [39]. Generally, as the scan rate increases the features observed at lower rates diminish or disappear also the peak current decreases (capacity decreases). Therefore, for higher diffusivity, the CV features show a smaller amount of faint as the scan rate increases. Also the peak separation increases with scan rate [65]. Despite the scan rate, all the CV profiles overlap at the beginning of charging and discharging. As sweeping voltage increases, current increases or vice versa. The oxidation reaction of $\text{Fe}^{2+} \rightarrow \text{Fe}^{3+}$ occurs in cathode during the charge with Li extraction (anodic reaction) Eq (3.1). The reduction reaction of $\text{Fe}^{3+} \rightarrow \text{Fe}^{2+}$ happens through discharge with Li insertion (cathodic reaction) Eq (3.2).



A reversible reaction shows a symmetric anodic and cathodic peaks with a true separation of 58mV at 25 °C which corresponds to an extremely small scan rate [65].

3.3.2. Cycling tests

The charge and discharge behaviors were characterized between 2.5 and 4.0 V by a multi-channel battery tester MTI Corp. All the measurement were carried out in the ambient temperature.

3.3.3. Electrochemical Impedance Spectroscopy (EIS)

A potentiostat (PARSTAT2273) was used for the impedance measurement. EIS was utilized by applying an alternative voltage of 5 mV in the frequency range from 10 KHz to 10 mHz. The measurements were performed a few hours after completion of the charge or discharge cycle.

3.4 Characterization

3.4.1. XRD

X ray diffraction pattern of LiFePO₄ powder D500 of synthesized LiFePO₄. (Fig. 3.6).

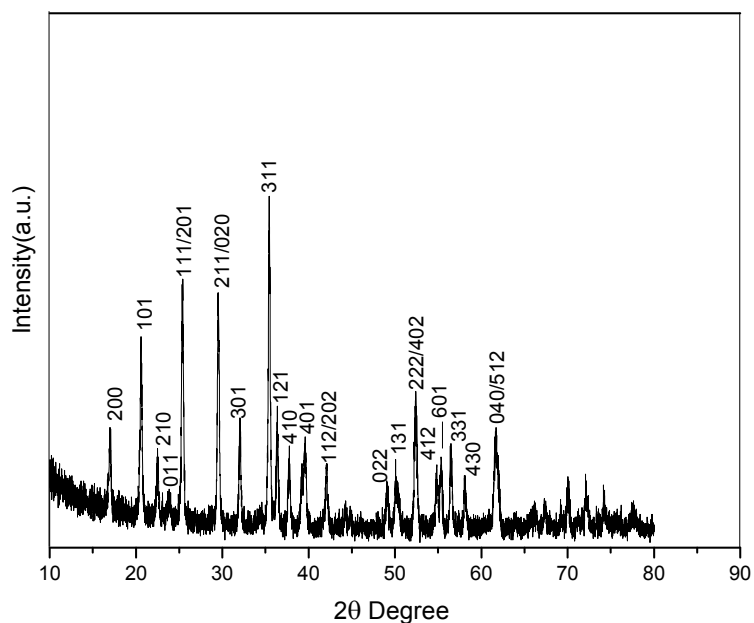


Figure 3.6 XRD pattern of LiFePO₄ powder synthesized with solid state method.

3.4.2 SEM

Scanning electron microscope (HITACHI S-3000N) was used for identification of the surface features and microstructure of the cathode surface and the electrode cross section.

3.4.3 Raman spectroscopy

Thermo Scientific DXR Raman microscope with a 532 nm excitation laser source, was used. Raman spectra were collected either from individual spots or a mapped area on the surface of the cathode. All the spectra were collected for the wave numbers from 50-2000 cm^{-1} at 25 °C. Two different approaches were utilized for collecting the spectra: ex-situ and in-situ Raman spectroscopy.

3.4.3.1. Ex-situ Raman spectroscopy

The Ex-situ Raman spectroscopy was implemented in the ambient atmosphere either for a spot or a mapped area of the cathode. The laser power was adjusted to 2-3 mW for collecting the Raman spectra of the cathode, carbon additive, EC and DMC. The effect of laser power on the decomposition of the cathode was performed by applying different laser powers from 2.5-10 mW to the surface of the cathode.

Table3.2. The setup of the Raman spectroscopy for Ex-situ experiments.

Ex-situ experiments	Spot size (μm)	Laser power(mW)	Exposure time(s)	Photobleaching time (s)	Magnification
Spot spectra	2.1	2-10	32	30	10X
Area mapping	2.1	10	16	30	10X

The mapping technique was employed to investigate the compositional change on the surface of the cathode and also to define the appropriate position for in-situ Raman spectroscopy. Before assembling the battery for the in-situ experiment, four adjacent area of $150 \times 150 \mu\text{m}^2$ were mapped with the laser power of 10 mW and the area with appropriate composition was studied for in-situ Raman spectroscopy. Also the compositional distribution of 16 sub-areas of $(20 \times 20) \mu\text{m}^2$ within the total area of $(80 \times 80 \mu\text{m}^2)$ on the cathode surface were

investigated . The set up for collecting the data in the ex-situ experiments is summarized in table 3.2.

3.4.3.2. In-situ Raman spectroscopy

Fig.3.7 shows the setup of the in-situ experiment. The charge and discharge behaviors were characterized by a multi-channel battery tester between 2.5 and 4.0 V while the in-situ Raman spectroscopy was conducted. The charge and discharge were performed at 0.4C rate except at the end of the charge in which a constant voltage was applied at 4.0V. The setup of the Raman spectroscope as shown in Table 3.3.

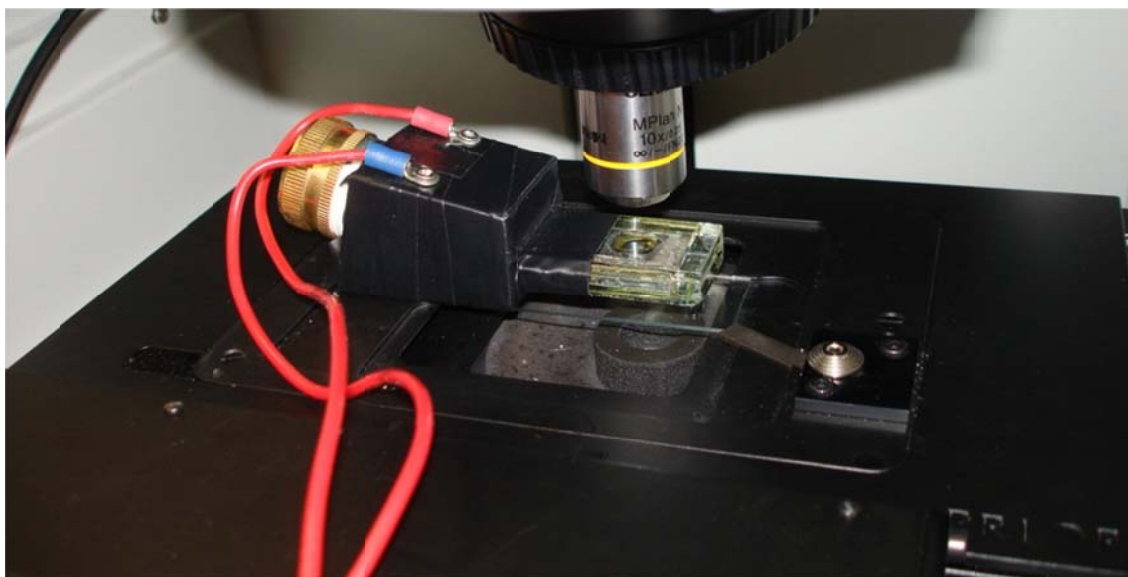


Figure3.7 The setup of the in-situ experiment. After placing the case in appropriate position, the wires were passed from a hole through the instrument cover and connected to the charger for cycling.

Table3.3. The setup of the Raman spectroscope for the In-situ experiment.

Wave length (nm)	Spot size (μm)	Laser power (mW)	Exposure time (s)	Photobleaching time(s)	Magnificathion
532	2.1	2	`32	30	10X

CHAPTER 4

RESULT AND DISCUSSION

4.1 Introduction

In this chapter the initial steps for making the optimized LiFePO_4 cathode are described. Also the effect of additive carbon and pressure on the cell performance, the qualification of the conductive network of C- LiFePO_4 cathode, cycling behavior of the cathode with various carbon contents, and EIS are discussed. Subsequently, the optimized cathode with appropriate formula was used for in-situ Raman study in an operating Li-ion cell.

4.2 Improvement of the cell performance

4.2.1 Electrochemical cell design

The lithium ion cases have an air tight structure to provide an isolated system for the favorite reactions inside the case. Although cases for the routine experimental purposes are available in the market, the special case for in-situ Raman spectroscopy should be designed based on the requirements and available facilities. In order to achieve the technical ability for designing and building special cases, first the case for the routine electrochemical experiments was designed and built. Different cases were made to achieve the appropriate and stable performance of the lithium ion cell.

The structure of the designed cell is explained in the previous chapter (3.1.3). The electrolyte reservoir is made of glass because initially we planned to use glass window for the Raman spectroscopy. Besides, as explained in the experimental part, the transparent case is beneficial for visual access to the cell component and tracking the gas generation and possible current collector corrosion. The stability of the epoxy resin that was used for assembling the glass reservoir and making the connector was examined by storing a piece of cured epoxy

inside the electrolyte for a few days and no sign of degradation was observed. In case of the existence of the moisture in the system, hydrofluoric acid would be generated inside the electrolyte that would affect the glass. However, no corrosion was affected the surface of the glass reservoir during the usage of the cases that means the level of HF has been low.

The cap is a very important part because it should keep the system isolated over time and multiple usages. Two types of caps were used (a brass cap and a bigger size plastic cap) with reliable washers for sealing the cell. The washer was checked for any possible damages before assembling the battery.

4.2.2 Pressure effect

Batteries with pressed cathodes (C10p, C20p) and non-pressed cathodes (C10n, C20n) were assembled in the type A cases (Fig.3.3.A) to compare their charge/discharge behavior. The charge and discharge plots at different rates are demonstrated in Fig. 4.1 and Fig.4.2. The charging process of the cells with non-pressed cathodes occurred at higher charging potentials than those with pressed cathodes. Also the average discharge potentials of the cells with pressed cathodes are higher than those of the non-pressed ones. Therefore, increasing the pressure with the same amount of carbon additive leads to a higher voltage efficiency and narrower voltage window between charge and discharge. This is because applying pressure brings the particles more closer to each other which leads to a better electronically conductive network in the electrode. Hence electron transfer through the cathode would be facilitated.

Although pressing enhances the electronic conductivity of the cathode, it also reduces the size of the pores inside the pressed electrode which limits penetration of the electrolyte into the cathode. Therefore the amount of carbon and pressure should be optimized to meet the best working condition of the cathode. The improvement of the voltage efficiency by applying pressure is more pronounced for 10% carbon additive even in low discharge rates (Fig 4.1 A). The electronic network enhancement is demonstrated by a higher discharge voltage plateau and as a result of decreasing the internal resistance of the cell (chapter.2.3). Applying pressure

on the cathode with 10% carbon leads to a capacity reduction as a result of higher concentration polarization which indicates mass transport limitation. Pressing reduces the porosity in such a way that access of electrolyte to the active material is limited (Fig.4.1).

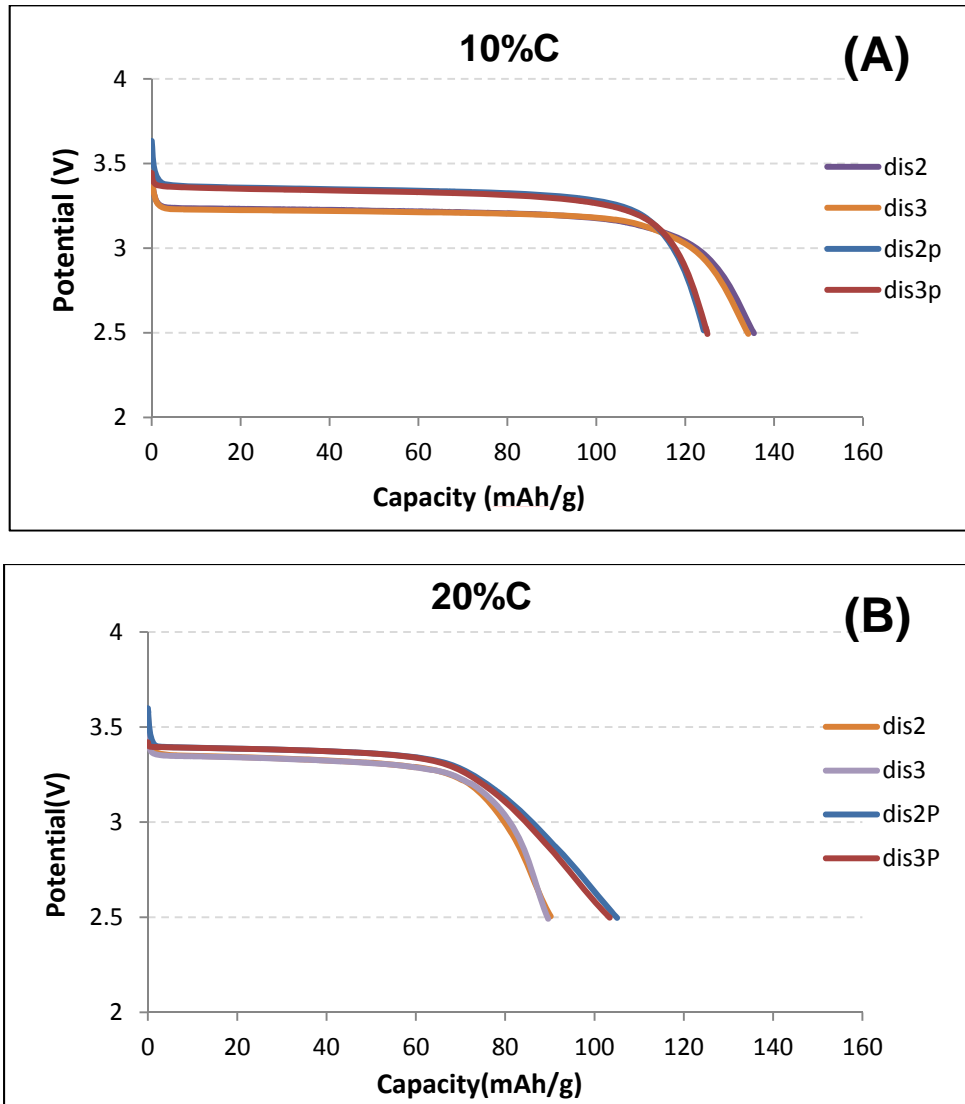


Figure 4.1 The effect of pressure on the performance of the cathodes with 10% carbon(A) and 20% carbon (B). The cathode was made without applying pressure in dis3 and dis4 and with applying 2.5 ton/cm² pressure in dis2p and dis3p. The charge and discharge rate of 0.1C was applied in all conditions.

On the other hand, in the non-compressed cathode with 20% carbon access of electrolyte to the LiFePO_4 particles may be already difficult (demonstrated by the reduced capacity compared to those with 10% carbon); applying pressure leads to an enhancement of the electronic conductivity and reduction of internal resistant polarization which slightly increases discharge plateau. Since much carbon exists between the active material particles, pressing enhances the electronic conductivity in the pores and provides enough space for Li diffusion. Consequently, capacity increases after pressing.

The difference in the discharge performance of the pressed and non-pressed electrodes is more pronounced at higher discharge rates. Fig. 4.2 shows the discharge behavior of the pressed and non-pressed cathodes with 20% carbon at 5C discharge rate. Although the potential plateau difference is not obvious at 0.1C Fig.4.1 (B), the difference at 5C is significant.

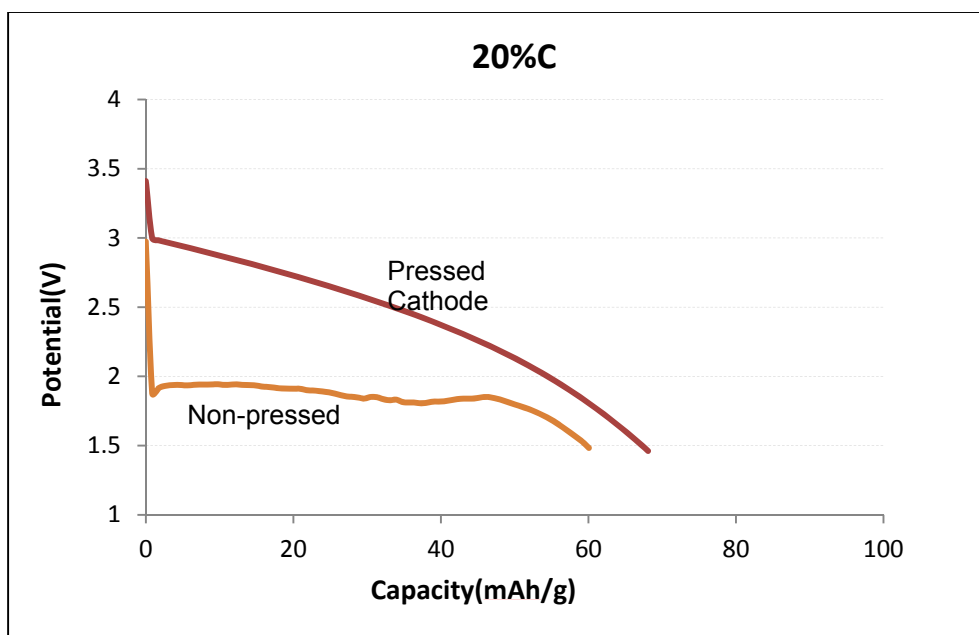


Figure 4.2 The effect of pressure on the performance of the LiFePO_4 cathode with 20% carbon at 5C discharge rate. The cells were assembled using the type A case. 2.5 ton/cm^2 pressure applied for making the pressed cathode.

The significant potential drop and unstable plateau for the non-pressed cathode shows the critical role of the enhanced electronic network of the electrode at high discharge rates since it shows more pronounced internal resistance polarization. On the other hand, the concentration polarization has a major role for the potential drop in the pressed cathode at 5C discharge rate. Therefore, the influence of different polarizations on the discharge behavior depends on the carbon content and the discharge rate.

4.2.3. Carbon additive effect

Despite the pressure, the quality and quantity of the additive carbon are also important in the performance of the batteries. Additive carbon provides appropriate porosity for the penetration of the electrolyte and at the same time acts as the electronically conductive matrix of the electrode. Increasing the carbon content of the cathode similar to applying pressure, improves the electronic conductivity which leads to a better voltage efficiency. The best condition in terms of voltage efficiency improvement at discharge plateau occurred when 20% carbon is used along with applying 2.5t/cm² pressure (Fig. 4.1 B and 4.2). The enhanced electronically conductive network of the C20p cell shows a reasonable trend in the electrochemical behavior of the cell at various discharge rates. Also the discharge behavior of the cathodes with 10% and 20% carbon additive at 1C discharge rate is demonstrated in Fig.4.3. The total capacity, and average discharge potential of the cathode with 10% carbon additive is lower than that of the 20 % carbon. The performance of the cathode with 10% carbon at 1C rate is affected with a higher internal resistance polarization as well as higher activation and concentration polarizations at 1C discharge rate.

The electrochemical performance of all the batteries improved after the first charge and discharge cycle. Generally, in the first cycle the penetration of the electrolyte into the pores of the cathode structure occurs, which in turn leads to the improvement of lithium ion diffusion through the carbon network and active material. This effect leads to a notable increase in the

energy efficiency from the first to the second cycle or a gradual improvement through the first few cycles.

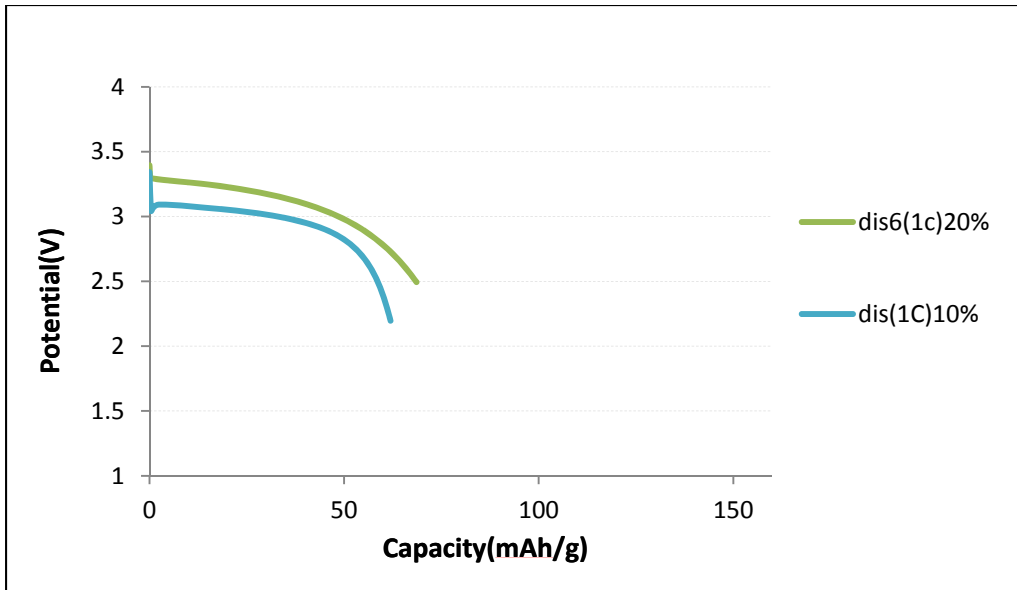


Figure 4.3 The discharge behavior of the cathode with 10% carbon (C10p), and 20% carbon (C20p) at 1C discharge rate for the pressed cathodes at 2.5 (ton/cm²).

Fig.4.4 shows the discharge capacity of the pressed cathodes with 10% and 20% additive carbon at different discharge rates. The charging process was carried out at 0.1C rate in all situations. The discharge capacity of C10 with 10% carbon additive is more affected as the discharge rate increases. By increasing the discharge rate from 0.1C to 1C, the capacity of the C10 cathode decreases to about 50% of its initial capacity. However the C20 cathode with 20% carbon additive content shows the capacity drop of about 20% and 30% at the discharge rate of 1C and 5C, respectively. The discharge capacity of the cathode with 20% carbon additive is better at high rates while at low discharge rates 10% shows a better discharge capacity.

The precise comparison of the electrodes which are made with different amount of carbon content, binder and volumetric energy density requires more detailed experiments such as measuring the porosity and investigating the microstructure of the electrodes; however, they

were dismissed because the main focus of this work is to find appropriate working conditions of our cases.

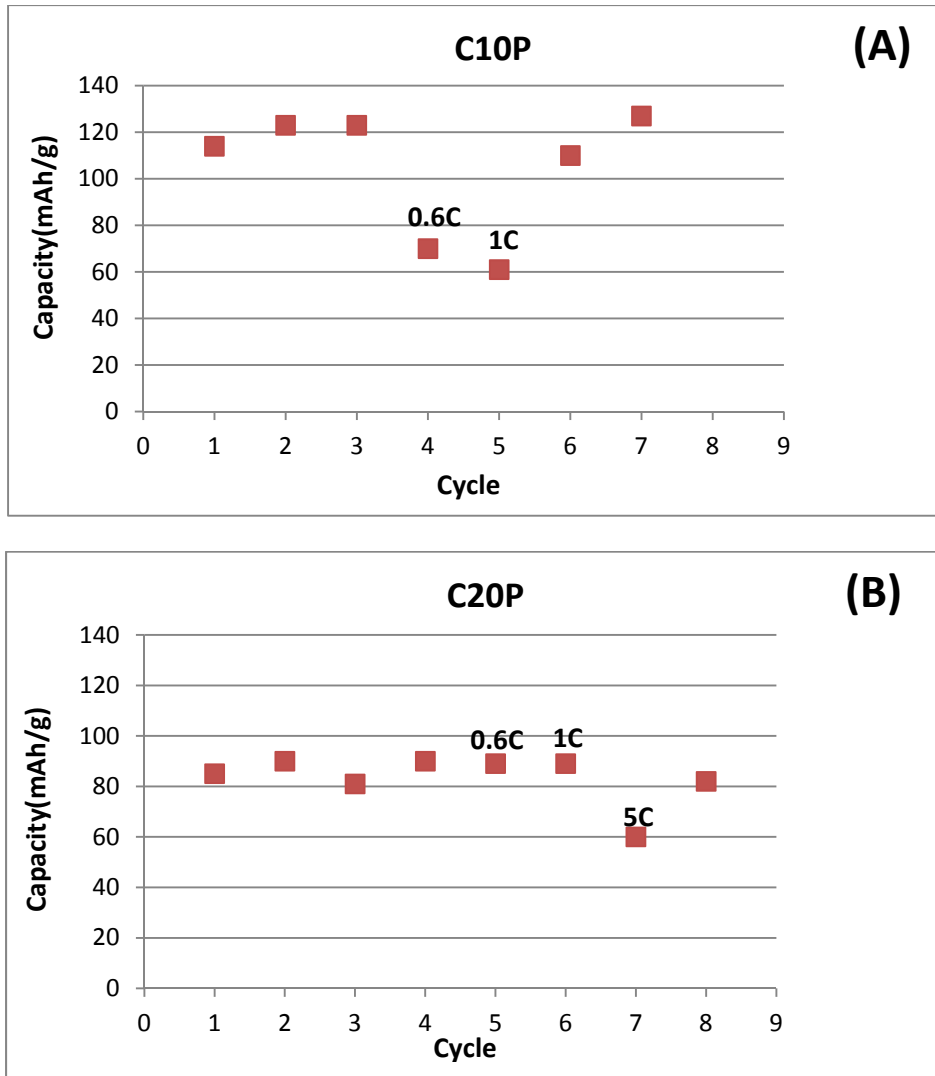


Figure 4.4 The variation of the capacity at different charge and discharge rates for the cathodes with (A) 10% and (B) 20% carbon. Both cathodes were pressed by applying 2.5 ton/cm². The discharge rate of 0.1C was applied during the discharge for the unmarked points in the discharge cycles.

In order to more accurately investigate the effect of carbon additive in the cell performance, a new series of experiment was set up by using fresh electrolyte, new lithium foil

and B type cells (Fig.3.2. B). The charge and discharge behavior of the cells with cathodes containing 2%,10% and 20% additive carbon (C2, C10 and C20) are demonstrated in Fig. 4.5. All the cells were assembled at the same time to provide a similar assembling condition. The area of the cathodes was fixed at $1.5 \times 1.5 \text{ cm}^2$ for all of the cells. After a few cycles from the beginning of the test at 0.1C rate, the capacity of the C10 cathode was about 142mAh/gr which is higher than those of the other two cells. However by increasing the charge and discharge rate to 0.5C, the capacity of C10 reduces to 99 mAh/gr and also difference between the total capacities reduces. The capacity of C2 comes to the second place 88mAh/gr and C20 shows the least amount of capacity 86mAh/gr. Considering the voltage efficiencies, the 10% carbon cathode shows the least efficiency. While the voltage efficiency of C2 and C20 is almost the same from the beginning to the end of the charge and discharge process but still 2% carbon shows a better voltage efficiency especially at the end of the charge and discharge.

Farther increasing the charge and discharge rate to 1C, 10% carbon shows the worse performance with a capacity of 62mAh/gr with the least voltage efficiency among the others. C2 shows the best capacity of 78 mAh/gr and the best voltage efficiency and the capacity of C20 is 68 mAh/gr with a voltage efficiency better than C10 but less than C2.

Although C2 contains the lower amount of carbon additive, it shows the lowest internal resistance polarization with higher voltage efficiency among the two other cathodes (C10 and C20). One reason for this behavior might be considered as the quality of corresponding carbon matrix of this cathode.

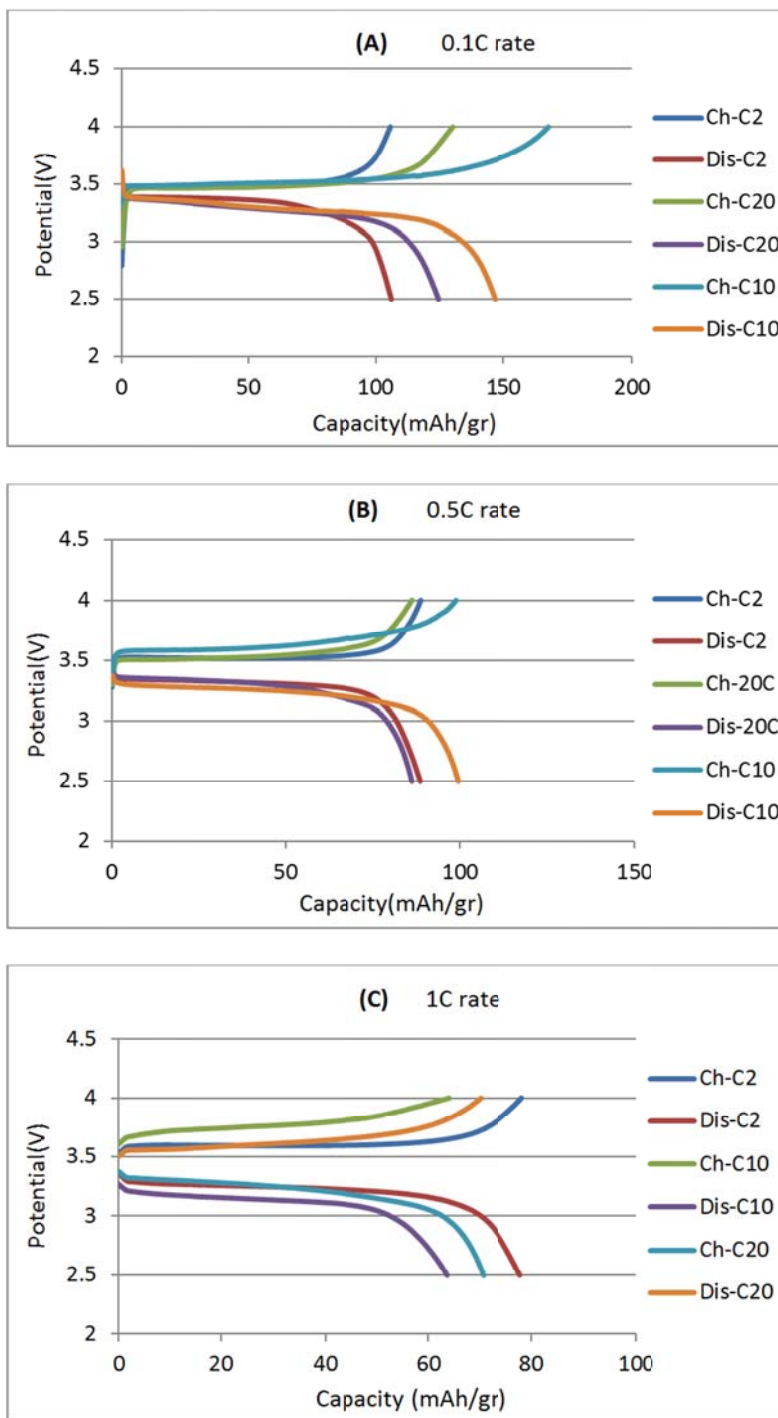


Figure 4.5 Electrochemical charge and discharge plots of the cells with C2, C10 and C20 cathodes. The charge and discharge performed at (A) 0.1C, (B) 0.5C and (C) 1C rate. The red numbers at the bottom of the figures are the average capacity in mAh/gr.

Fig.4.6 shows the deconvolution of carbon peak for the C2 and C10 cathodes. The Gaussian fit was used considering six different peaks for a perfect fit. The peaks were considered as G band at about 1585 (cm)^{-1} , D band at 1350 (cm)^{-1} and truly disordered sp^3 bands at 1190 (cm)^{-1} , 1490 (cm)^{-1} and 1620 (cm)^{-1} . I_D/I_G and sp^2/sp^3 were calculated by integrating the area under correspond vibrational bands (Table 4.1).

Table 4.1. Corresponding amount of sp^2/sp^3 and I_D/I_G for C2 and C10 cathodes.

Composition	sp^2/sp^3	I_D/I_G
C2 (2% carbon additive)	0.245	1.99
C10 (10% carbon additive)	0.213	2.32

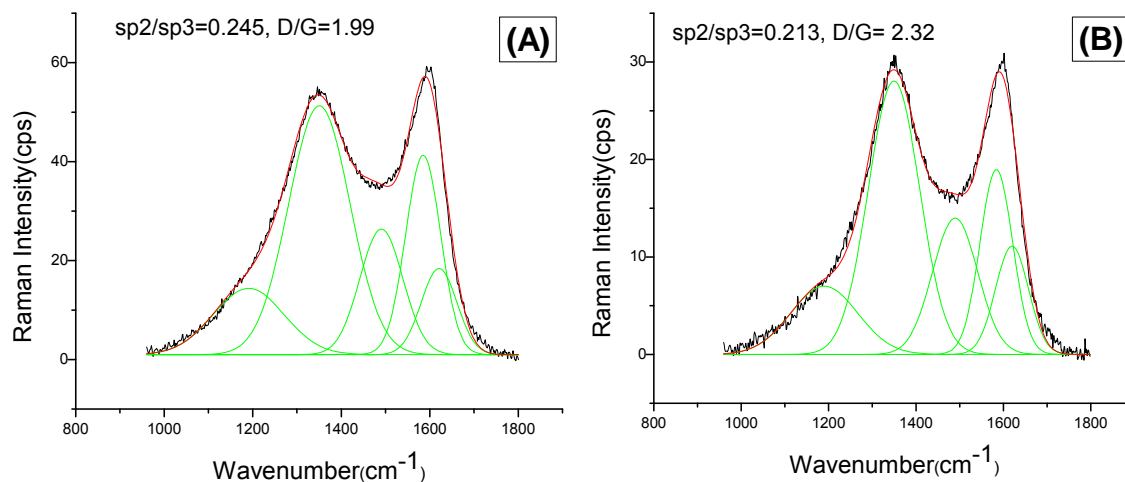


Figure 4.6 Peak deconvolution of carbon fresh electrodes (A) electrode with 2% carbon (C2), (B) electrode with 10% carbon (C10).

The value of I_D/I_G can be employed to compare the crystallite size of graphite in the carbonaceous materials. Although the origin of the D band has been an issue of controversy, it is frequently considered for the symmetry breakage at the edge of graphite basal plane. As the crystallite size of graphite reduces I_D increases (see section 2.3.2.3), the higher value of I_D/I_G for C10 than that of C2 indicates a smaller graphite crystallite size for C10. As C2 has an open

micro structure (see Fig.4.7 C and D), the carbon coating in the C-LiFePO₄ particles more affect the spectra and the difference is related to a larger crystallite size of the carbon coating. Also the ratio of sp²/sp³ which is potentially beneficial for a better electronic conductivity is higher in C2 than that of C10.

Table 4.2. Capacity drop of cathodes by increasing the discharge rate with different carbon additives.

Carbon additive (wt%)	2%(C2)	10%(C10)	20%(C20)
Capacity drop (%)			
0.1C→0.5C	18	30	25
0.5C→1C	9	37	21

In the cathode with 2% carbon additive, the loading of active material is more, which in turn dictates a relatively higher density of the cathode. The pressing of the electrode in the fabrication process makes the particles compact. Hence, C-LiFePO₄ particles form a structure without enough surrounding carbon additive to provide an appropriate conductive network for all LiFePO₄ particles (see Fig.4.7). The large pores size of C2 and isolation of some regions from the conductive network leads to a low capacity of C2 at 0.1C discharge rate. Despite the lack of conductive network in some regions, the existing electronic network of C2 which is mainly provided by the carbon coating on the surface of LiFePO₄ particles has a relatively better conductivity than C10 and C20. As a result, the capacity fading of C2, by increasing the discharge rate, is less than the others (Table 4.2.).

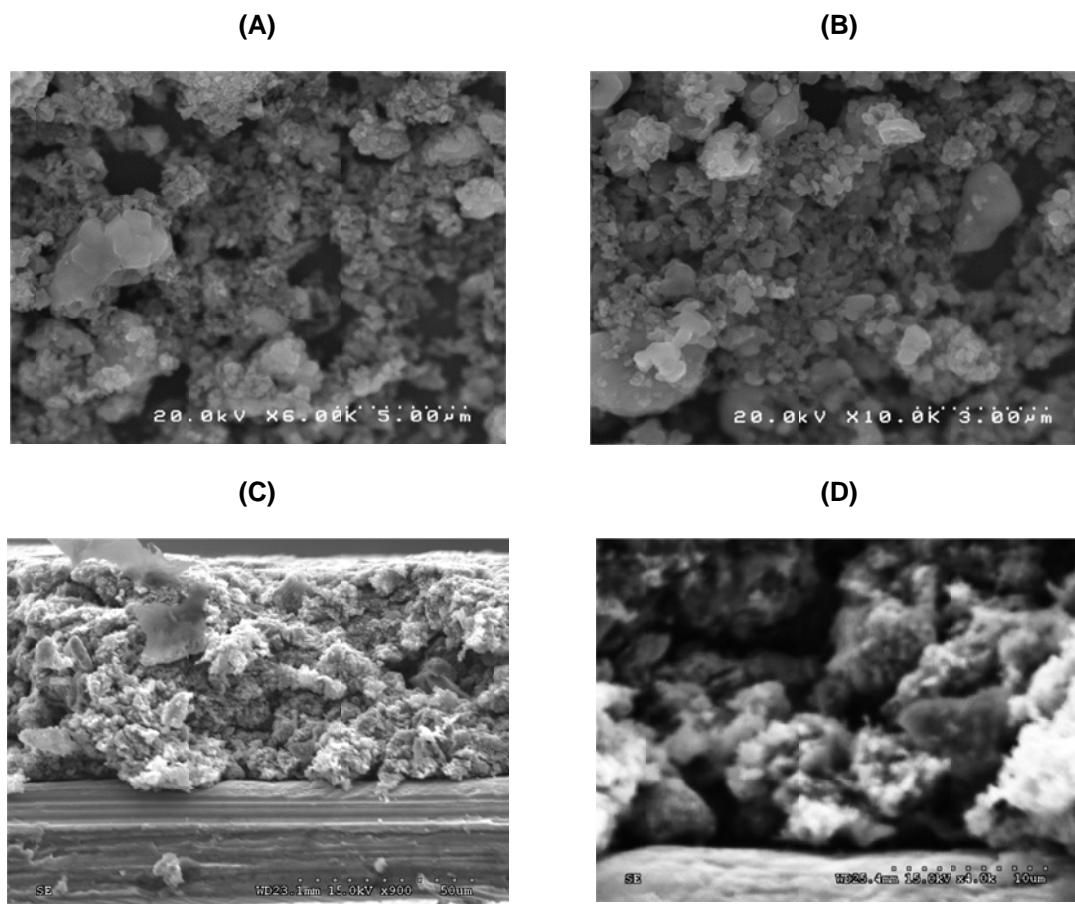


Figure 4.7 (A) and (B) SEM image of synthesized material with solid state method without additive carbon. (C) and (D) SEM image of the cross section of fresh C2 cathode. The pores structure of the cathode is demonstrated in different magnifications indicating insufficient carbon around the active material.

The capacity drop of C10 at higher discharge rates is more than the other two cathodes due to the weakly compacted carbonaceous material. The carbon additive of C10 fills the pores as well as inter-particle spaces; however, the conductive network is not appropriate for high discharge rates. The electronic network of C20 is better than C10. The packed structure of carbon additive of C20 provides a better electronic conductivity than C10; however; its compact structure prevents the electrolyte penetration. Since the ionic conductivity is also important for the performance of the cathode, the ionic conductivity for the cathodes with more open pores

would provide a better access of the electrolyte to the active material which is beneficial for the cell performance. Later in section (4.4.5), we will discuss how the concentration change in the surface of the cathode might affect the ionic conductivity and consequently the performance of the cell.

Fig.4.8. shows the performance of the cells at different discharge rates. The capacity fading of C2 is the least among all the cathodes, regarding the properly connected conductive network of majority of particles. Also C10 shows the most capacity fading as the discharge rate increases. The conductive network of the cathode should be optimized based on the working condition of the cell to maximize the volumetric density with the optimized performance.

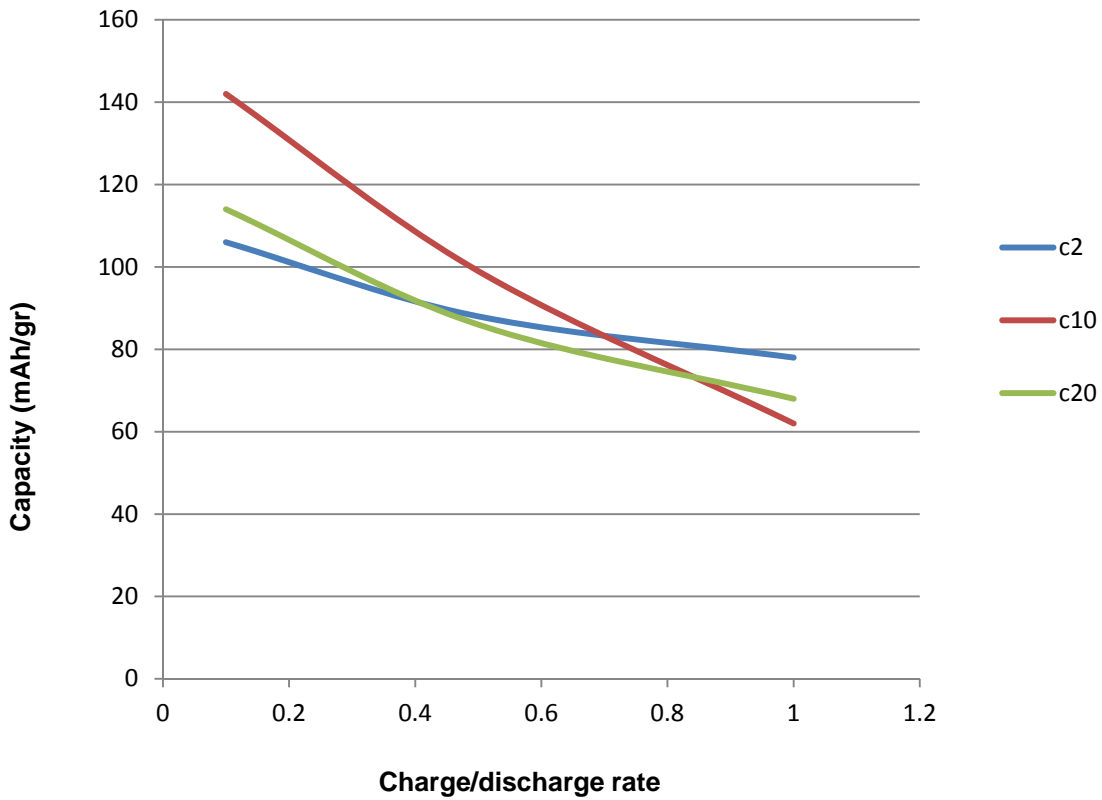


Figure 4.8 Total discharge capacity of C2, C10 and C20 cathodes in different discharge rates. The cells were assembled in type B cases.

In fact to reach the best performance, all the conductive components of the cell should be optimized. Ionic and electronic conductivity are inter-related parameters which widely affect the cell performance also the influence of them to the total conductivity depends on the discharge rate. The high capacity fading of C10 at high rates is due to its weak electronic network and insufficient open pores structure to maintain a good performance in high rates. Consequently it shows the higher internal resistance and concentration polarizations as the discharge rate increases. C20 shows a less internal resistance polarization and a better rate performance than C10. The abundance of carbon provides a good electronic network with a

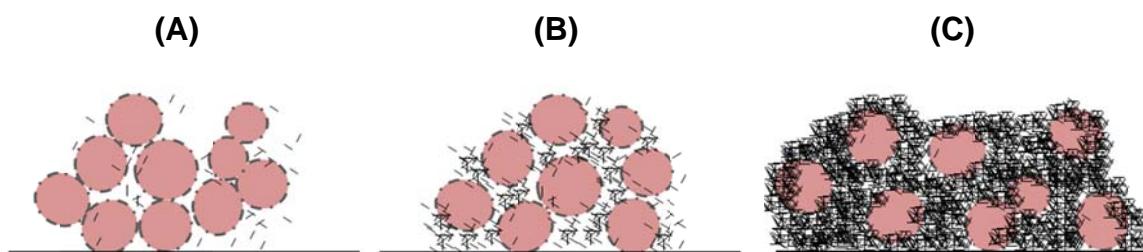


Figure 4.9 Schematic representation of the cathodes with different carbon content.(A), (B) and (C) show cathodes with 2% , 10% and 20% additive carbon respectively.

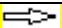

small pore size which reduces electrolyte penetration into the particles which reduces the total capacity. Therefore, the internal resistance and concentration polarizations are less affected at higher discharge rates. C2 has an open pore structure with a high quality but insufficient electronic network which is mostly provided by carbon coating. So initially the capacity is low because all the active material is not well connected to the current collector but its rate performance is the best (due to direct contact of particles with high quality carbon). A schematic representation of the cathodes with various carbon contents is shown in Fig.4.9.

4.2.4. Effect of additive carbon on the cycling behavior

To investigate the carbon additive effect on the cyclic behavior, C2 and C10p type cathodes were cycled at different rates with the testing condition summarized in Table 4.3. The capacity fading of the cells at the charge/ discharge rate of 1C during cycling is demonstrated in

Fig. 4.10. The capacity fading of C10p cathode with 10% carbon content during the 420 cycles at 1C rate is about 29% while the capacity fading of C2 type cathode is about 51% only during 264 cycles at 1C rate. The capacity fading of C2 has been 1.6 times more than that for C10p type cathode. Therefore the carbon additive not only affects rate performance of the cathodes but also it has a remarkable role on cyclic performance of the cell; therefore, the optimized interface between the carbon additive and active material improve the cyclic performance of the cathode.

Table 4.3. Cyclic tests on C2 and C10p type cathodes.

Cathode type 		
Cycle test 	C2	C10p
0.1C rate cycles	3	5
0.3C rate cycles	0	56
0.4C rate cycles	0	28
0.5C rate cycles	10	2
1C rate cycles	264	420
2C rate cycles	0	2
Total cycles	277	519
Capacity loss	82-40 (mAh/g)	79-56 (mAh/g)
(at 1C rate)	51%	29%

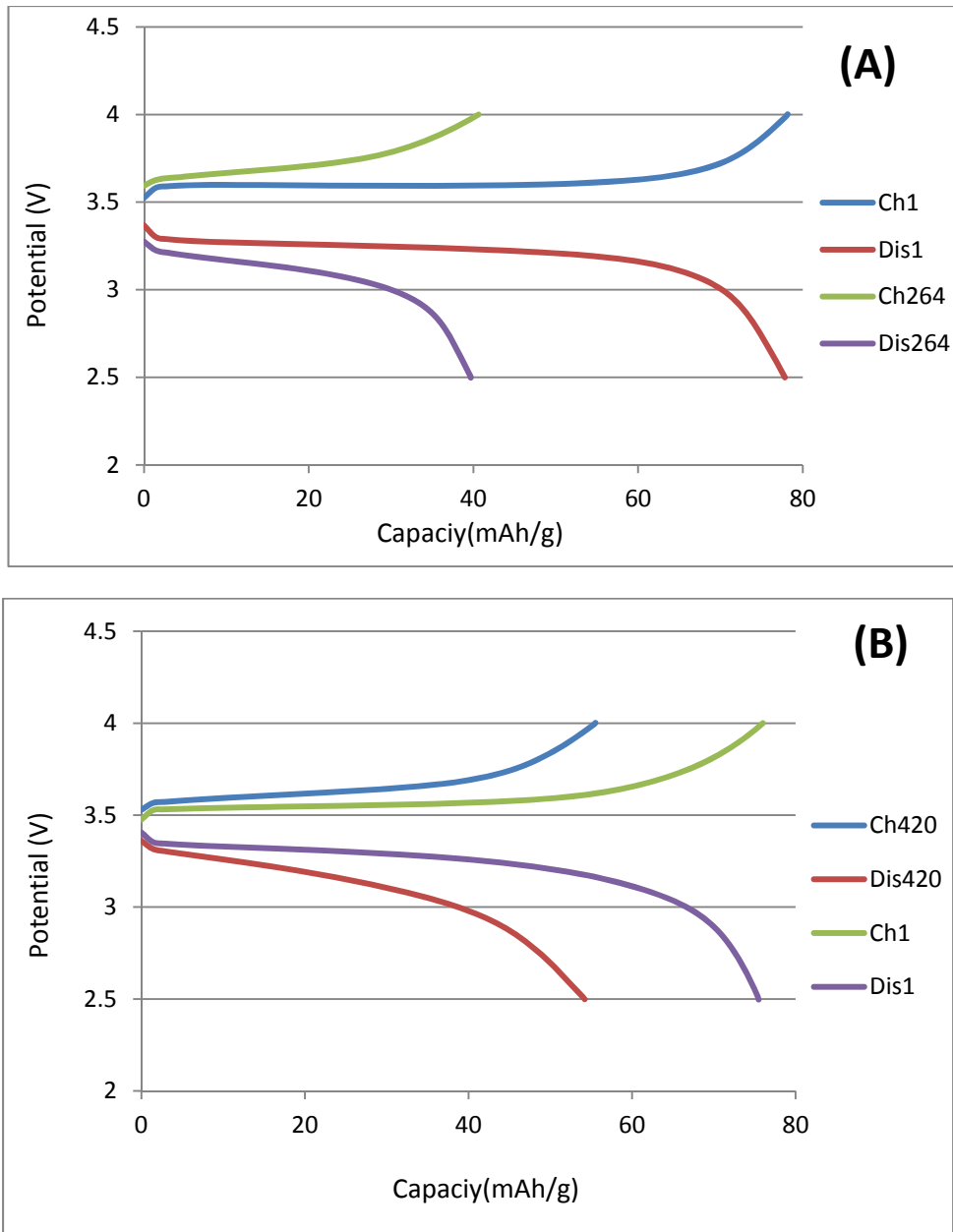


Figure 4.10 Cyclic behavior of (A) C2 cathode with 2% carbon additive during 264 cycles, and (B) C10p cathode with 10% carbon additive during 420 cycles. Both capacity fading were studied at 1C rate.

Raman spectroscopy of carbonaceous material of fresh and aged (C2 and C10p) cathodes is demonstrated in Fig.4.11. The Lorentz fit was used for peak deconvolution. The

peaks were considered as G band character at about 1585 (cm)^{-1} , D band at 1350 (cm)^{-1} and truly disordered sp^3 bands at 1190 (cm)^{-1} , 1490 (cm)^{-1} and 1620 (cm)^{-1} .

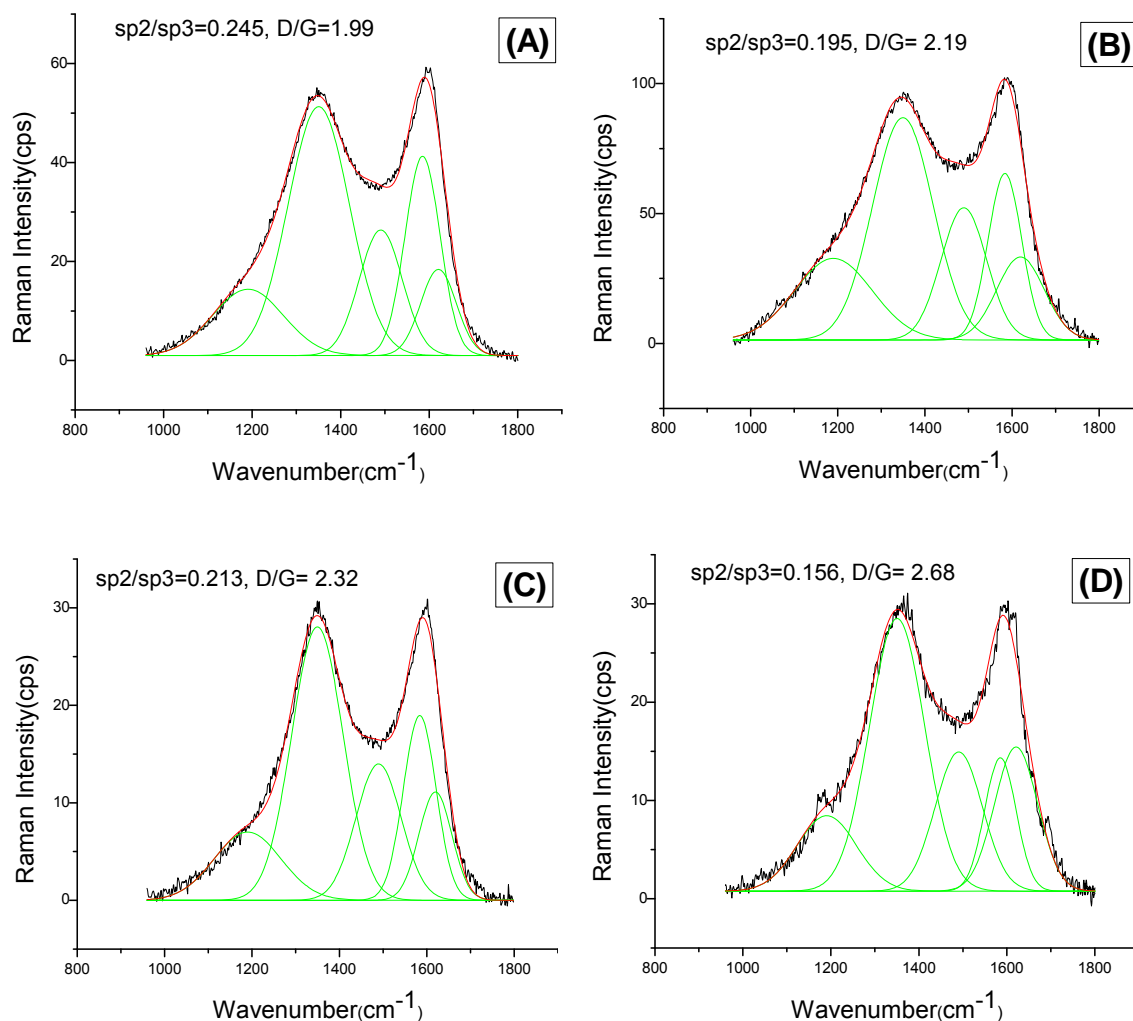


Figure 4.11. Raman spectra of carbonaceous materials with corresponding SP^2/SP^3 and I_D/I_G . (A) fresh electrode with 2% additive carbon C2, (B) Aged electrode with 2% additive carbon C2, (C) fresh electrode with 10% additive carbon C10p, (D) Aged electrode with 10% additive carbon C10p.

Carbon content of both types of cathode changes over cycling. The aged cathodes show higher I_D/I_G parameters after cycling and a lower SP^2/SP^3 . As a result of aging process the pulverization of the conductive carbon occurred and graphitized G band character changed to sp^3 type carbon which leads to an overall weaker conductive network of the aged cathodes.

Therefore, C2 with only 2% carbon additive shows a faster capacity fading over cycling than C10p (Fig.4.12).

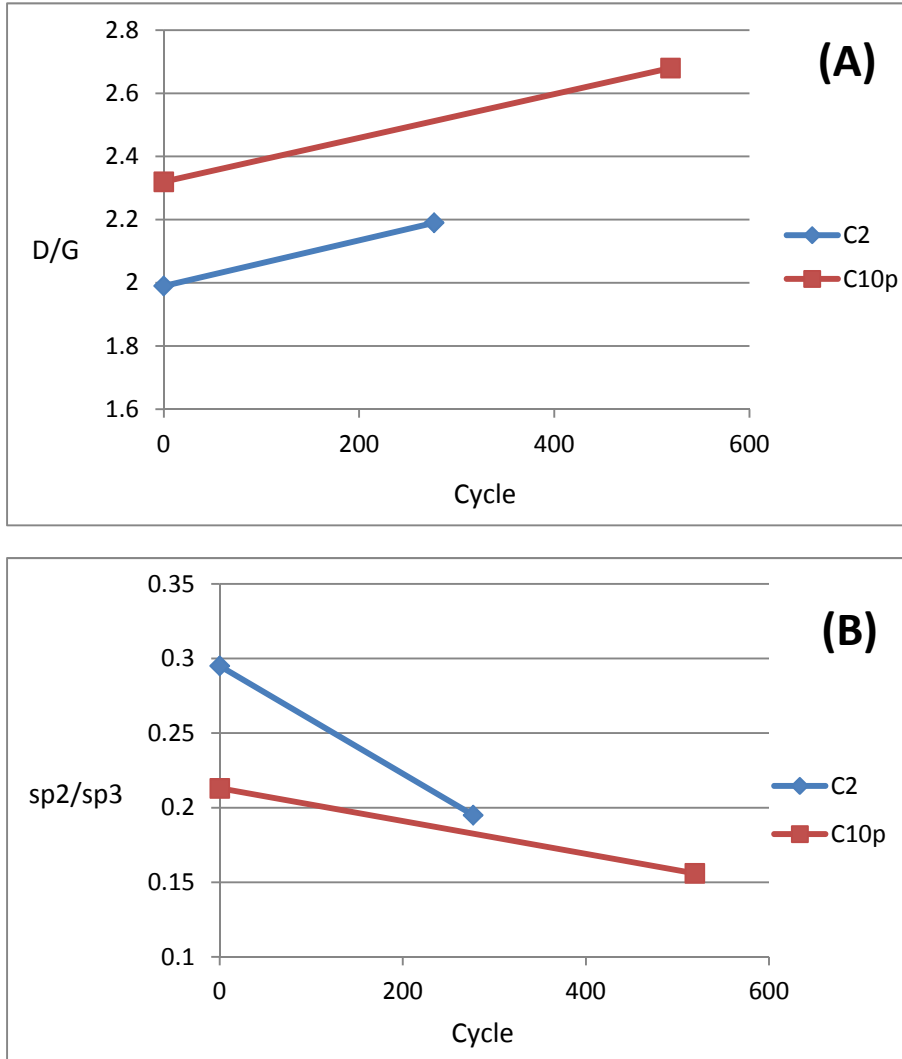


Figure 4.12 Carbon additive variation over cycling for C2 (with 2% carbon additive) and C10p (with 10% carbon additive) cathodes. Variation of (A) I_D/I_G and, (B) SP^2/SP^3 over cycling.

The supportive effect of carbon additive and pulverization was investigated by SEM images of aged and fresh cathodes. The microstructures of the fresh C10p and C2 cathodes with 10% carbon and 2% carbon, respectively, are compared in Fig.4.13.

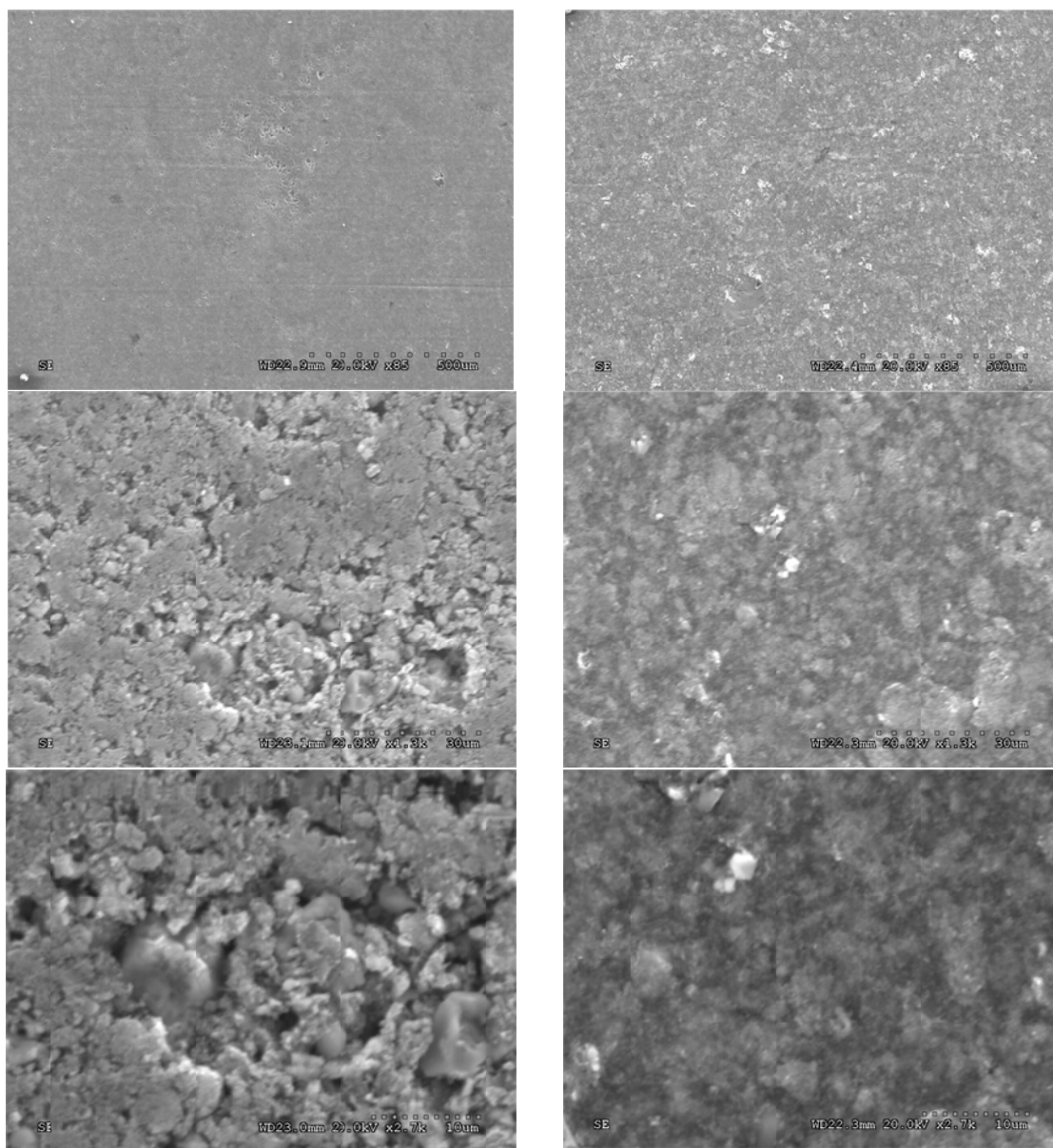


Figure 4.13 SEM image with different magnification of C2 cathode on the left side and C10p cathode on the right side.

The carbon additive of C10p fills the pore regions of the cathode and provides a supportive conductive network and reduces the capacity loss over cycling. SEM image of the C10p after more than 500 cycles is shown in Fig.4.14. The cathode was washed with DMC and dried before taking the SEM image. Formation of the cracks on the cathode may be due to the pulverization and reduction of the particle size of the cathode material. The cracks were formed after drying when the solvent removed from the inter-particle spaces.

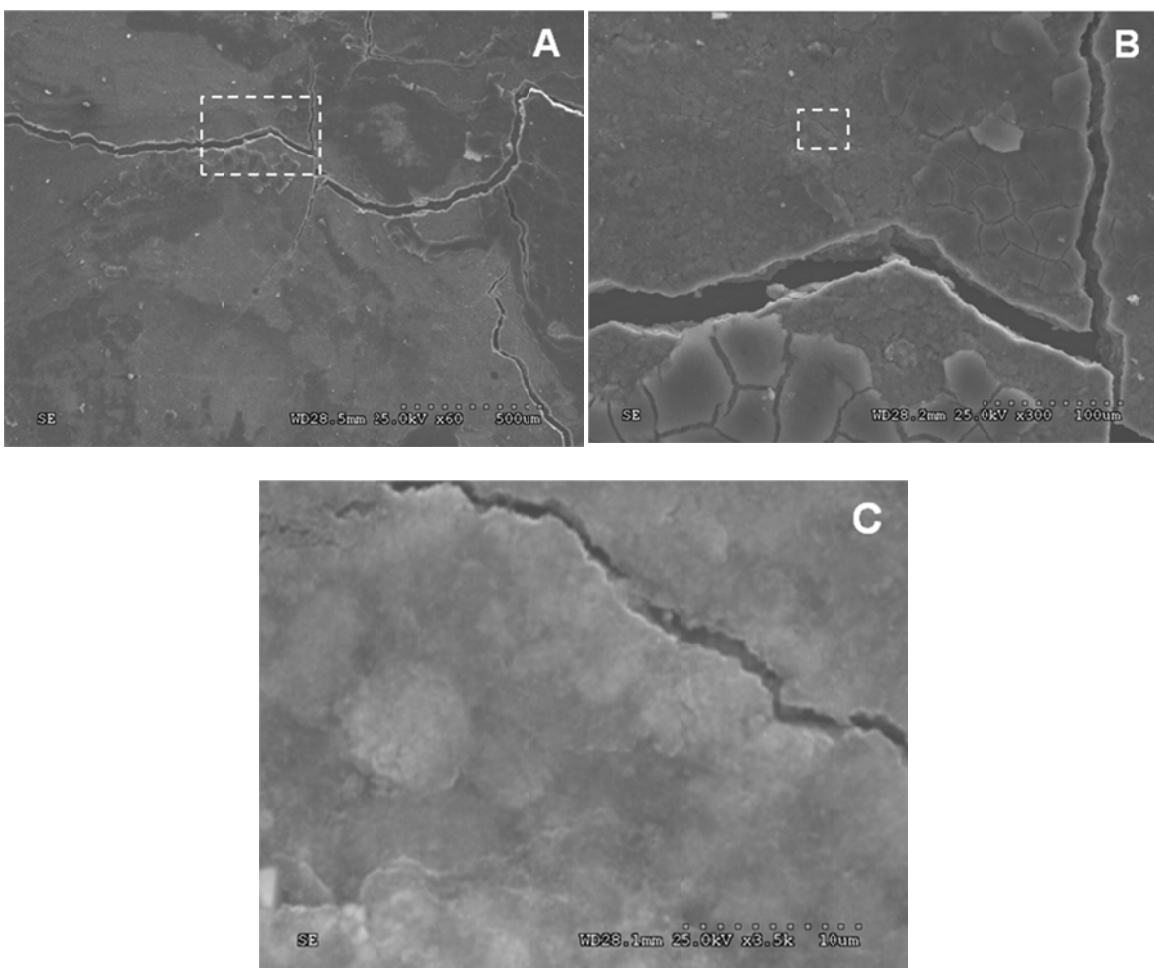


Figure 4.14 SEM image of C10p cathode after more than cycles. The reduction of the particle size of the cathodes leads to the formation of the cracks in the cathode. The indicated area in (A) and (B) are demonstrated in (B) and (C) respectively with higher magnification.

4.3 Electrochemical Impedance Spectroscopy

Fig.4.15 shows the Nyquist plots of the C10 and C20 cathodes after the charge and discharge at 0.1C and 1C rates. The AC impedance behavior is similar to the model that has been suggested for LiCO_2 [41] (Fig.2.13). Since the impedance was measured for whole cell, the Nyquist plots show the behavior of both cathode and anode electrodes; therefore interpretation about the behavior of individual electrochemical elements of the electrodes might be challenging. In fact, two Nyquist plots of cathode and anode are superimposed to form the existing plots. However, comparison of the Nyquist plots provides useful information about the cathode behavior because other components of the cells are the same for all experiments.

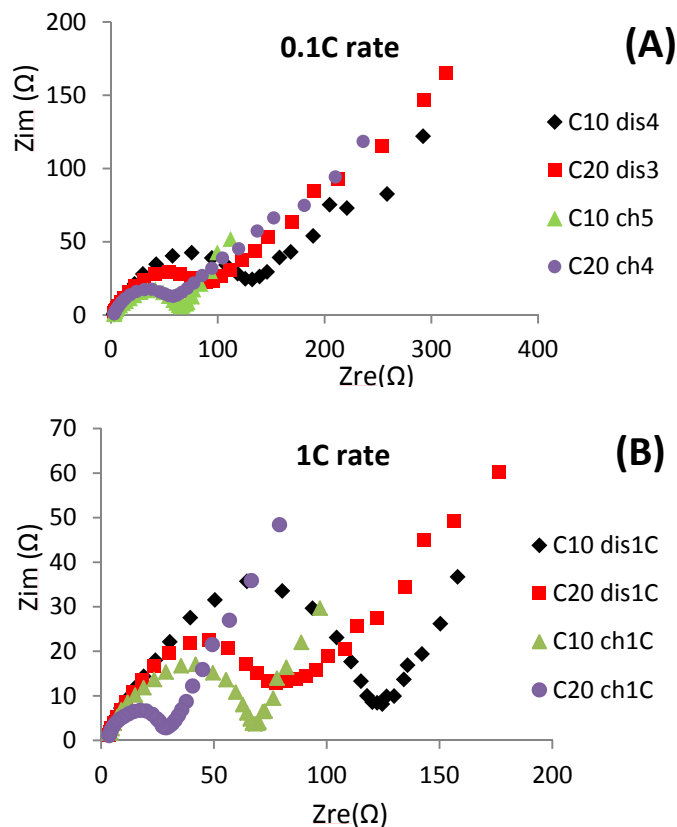


Figure 4.15 The Nyquist plot of C10 and C20 in the frequency range of 10 KHz –10 mHz. Charge and discharge was performed at (A) 0.1C and (B) 1C.

The measured resistance at very high frequency region corresponds to the ionic resistance of the electrolyte that was about 2-3 Ω in the beginning of the tests. The resistance of the electrolyte increased over cycling due to the existence of unavoidable moisture in the cell and formation of HF (Eq.2.1-2.4). As a consequence, the reaction between HF and LiPF_6 changes the optimized electrolyte concentration and ionic conductivity of the electrolyte (chapter 2.1.3).

The charge transfer resistance and capacitance of double layer are defined by the medium frequency semicircles which are reduced by increasing the carbon additive of cathode, also by charging the cell. The charge transfer resistance arises from kinetics hinder the electrochemical redox reactions in the electrode-electrolyte interface (Eq.2.6). In fact both electronic and ionic conductivity in the interface affect the charge transfer resistance. As Fig.4.14 shows C20 shows a lower charge transfer resistance than C10. Increasing additive carbon provides more sites for transferring electron between the active material and lithium ions in the interface which in turn reduces the charge transfer resistance. Also, the charge transfer resistance in charge state is less than discharge which might be related to a better ionic conductivity of the charged electrode. In fact, charged particles contain more FePO_4 ($D_{\text{Li}} = 1.27 \times 10^{-16} \text{ cm}^2 \text{ s}^{-1}$) than LiFePO_4 ($D_{\text{Li}} = 8.82 \times 10^{-18} \text{ cm}^2 \text{ s}^{-1}$) [6] on the particle surface. Charge and discharge at higher rates also increase the charge transfer due to the pulverization of conductive carbon in high rates (chapter 2.2). The charge transfer resistance of C2 cathode is relatively lower than that of C10 and C20. As a consequence, C2 shows relatively higher voltage efficiency and average discharge potentials at different rates (Fig. 4.16). The impedance behavior of C2 is similar to C10 and C20; however, charge transfer resistance shows less increase over high rate charge/ discharge in C2 than C10 and C20 due to the better conductive network of C2 than C20 and C10.

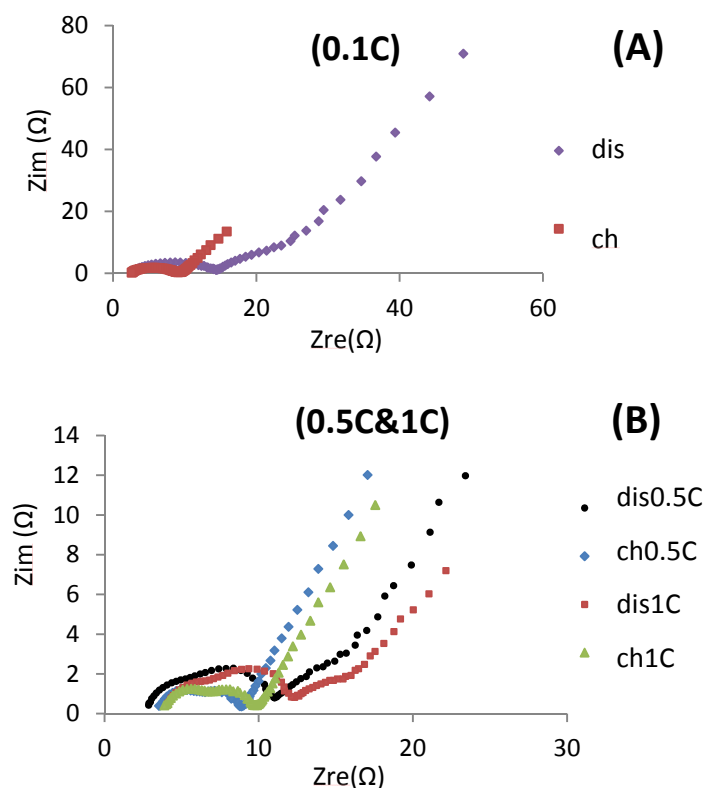


Figure.4.16. The Nyquist plot of C2 in the frequency range of 10 KHz –10 mHz. Charge and discharge was performed at (A) 0.1C rate and (B) 0.5C and 1C rate.

4.4 In-sit Raman spectroscopy of the surface of LiFePO_4 cathode in a working Li- ion battery

4.4.1. Introduction

Raman spectroscopy is a sensitive characterization technique to investigate the structural properties of both electrodes and the electrolyte solutions in the lithium ion cells. Many research groups have utilized Raman spectroscopy to study the surface phenomena of the electrodes [45, 46], and also the structure of the electrolyte systems including ion-ion and ion-solvent interactions in aprotic media [47-49]. Different approaches such as Raman mapping have been followed for data acquisition and analysis [50, 51]. Most of the previous works employing Raman spectroscopy on battery diagnosis were either ex-situ studies or not optimized for battery performance. The obtained results were thus not representative and difficult to apply to normal batteries, e.g., those operated in electric vehicles. In-situ Raman

spectroscopy provides real-time structural and chemical information in an operating battery and opens up a new venue for the investigation of dynamic reactions at the interface between the cell components. However, despite recent significant advances, extraction of the relative information from the electrodes, which have been examined primarily ex-situ, still remains a challenge using in-situ Raman due to the evolving environmental conditions and non-equilibrium reactions occurred during the characterization[50].

In this work, in-situ Raman spectroscopy is used for the first time, the variant electrolyte concentration on the C-LiFePO₄ particle surface was probed during a charge-discharge cycle. Structural changes of cathode materials during the in-situ Raman study and battery tests are also discussed.

4.4.2. Electrochemical cell design

Fig. 4.17 shows the cell for the in-situ Raman experiments. The experimental cell was made of an airtight cavity of glass as the electrolyte reservoir, an epoxy connector, and a sealant cap. The conductive terminals of the cell were made of steel for both the cathode and anode connections. Single crystal NaCl (Edmund Optics) attached to the cell was used as the transparent window for the laser pathway.

As Fig. 4.17 shows, our cell configuration prevents the cathode surface to be covered with an excessive amount of electrolyte which consequently facilitates the penetration of the laser beam and therefore detection of active material as well as adjacent electrolyte on the cathode surface.

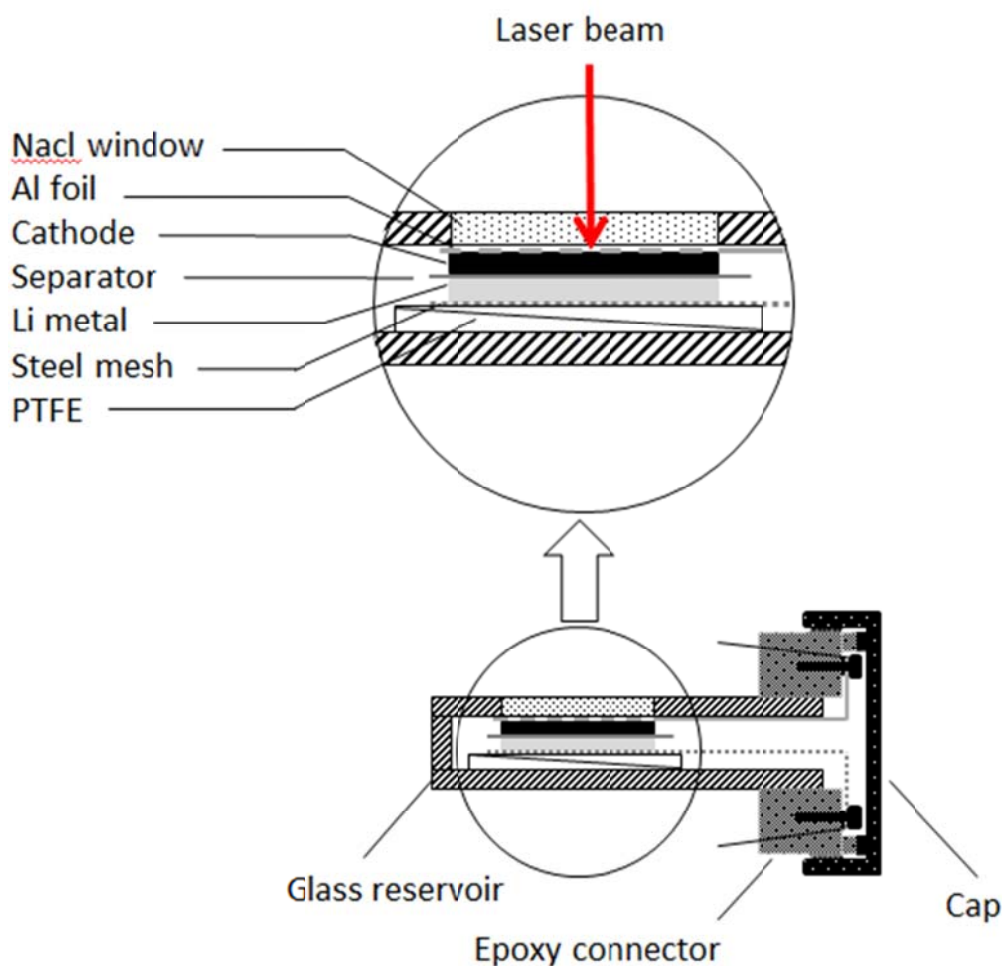


Figure 4.17 Schematic representation of in-situ Raman experimental cell

4.4.3 Carbon removal from the cathode surface

Though the amount of electrolyte on the surface of the cathode is minimized, the penetration of the laser beam to the surface of LiFePO_4 particles may still be blocked by the carbon coating which has been routinely applied to increase conductivity. In addition, the conductive carbon coating may also diminish the intensity of the active vibrational modes of LiFePO_4 [59].

Fig.4.18 A shows the typical Raman spectra of the carbon coated LiFePO_4 which represent a strong G band (1580 cm^{-1}) carbon, with sp^2 hybridization state [62], than the D band (1340 cm^{-1}) corresponding to disordered carbons.

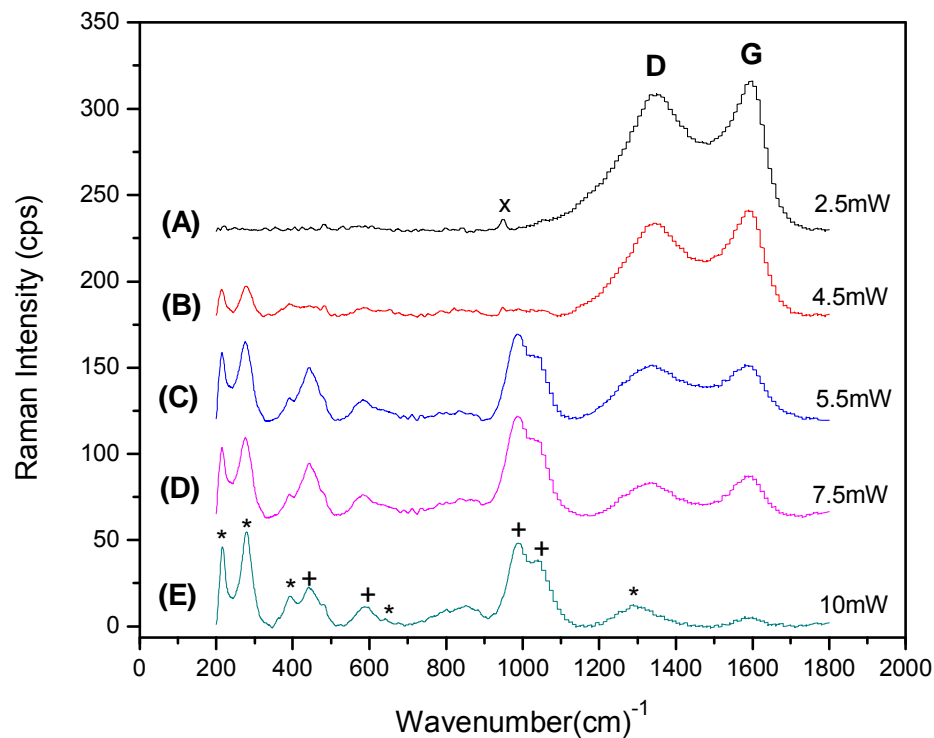
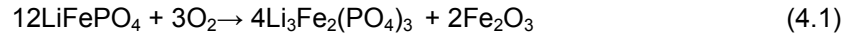


Figure 4.18 (A) - (E) Raman spectra of the C- LiFePO₄ as a function of laser power. Fe₂O₃ and γ -Li₃Fe₂(PO₄)₃ bands are marked by (*) and (+) symbols, respectively. LiFePO₄ peak is marked with (x). The laser beam of 532 nm with a spot size of 2 μ m was exposed to the surface of the cathode for 7 min.

The sp²graphitized carbon is beneficial for increasing conductivity of the LiFePO₄ particles; however, high electrical conductivity may reduce the optical skin depth δ (equation 2.4) of the incident laser beam. Consequently, the Raman scattering intensity decreases with increasing the conductivity. Raman laser beam was utilized to partially decompose and reduce the thickness of the carbon coating in the selected area on the cathode surface. In order to investigate the carbon removal process, Raman spectra were obtained from the same spot of the cathode at different laser powers. Figs. 4.18 A-E represent the oxidative effect of the incident laser beam on the cathode in the air atmosphere. As the laser power increases, the intensity of both the G band, sp² graphitized carbon, and the D band, amorphous carbon, decrease as the consequence of carbon gasification. The G band carbon was rapidly removed by the increase of the laser power and at 10 mW power, the remaining graphitized carbon is

negligible. On the other hand, the intensified peaks at the wavenumbers of 488, 990 and 1040 cm^{-1} are formed with the increase of the laser power due to the product $\gamma\text{-Li}_3\text{Fe}_2(\text{PO}_4)_3$ [57], from oxidative decomposition of LiFePO_4 via the following reaction:



Our results are in agreement with the observation reported by E. Markevich et al.[57]. The peaks at 217, 277, 395, and 600-650 cm^{-1} are assigned to iron oxide, from the decomposition of LiFePO_4 in air. The above results indicate that the gasification of the carbon coating by applying laser beam in air should be performed carefully to prevent oxidation of the LiFePO_4 particles.

As the coated carbon has been gasified by the laser beam, the post-exposed cathode would be less conductive. Consequently, as Eq.2.13 shows the penetration depth of the laser beam would increase. This would provide a better condition for detection of the LiFePO_4 bands during the in-situ experiment. On the other hand, since the carbon distribution varies across the cathode electrode surface, the laser irradiation and therefore decomposition of the LiFePO_4 by the laser beam is different. Additional care has also been taken to choose electrode surface with less LiFePO_4 decomposition for the in-situ Raman studies.

In order to practically estimate the local distribution of LiFePO_4 , four adjacent $150 \times 150 \mu\text{m}^2$ areas on the surface of the cathode were mapped in the ambient atmosphere Fig.4.19(a). During the mapping of the individual areas, the laser power was adjusted at 10mW and exposed to the area for 5minutes. The Raman spectra of domain C shows the carbon removal has happened with no decomposition of LiFePO_4 which facilitate the laser beam penetration from the surface. The domains (C and D positions) with the most intense Raman bands of ν_1 (less decomposition of LiFePO_4) were selected for further studies using the in-situ Raman spectroscopy.

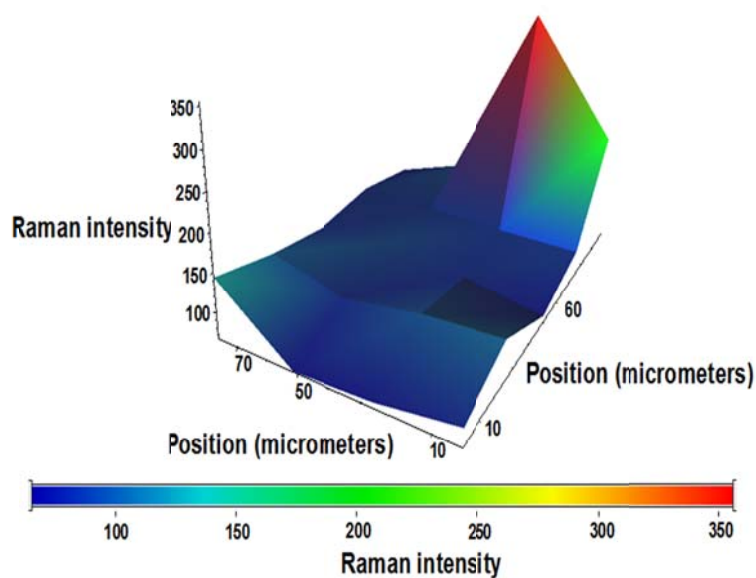
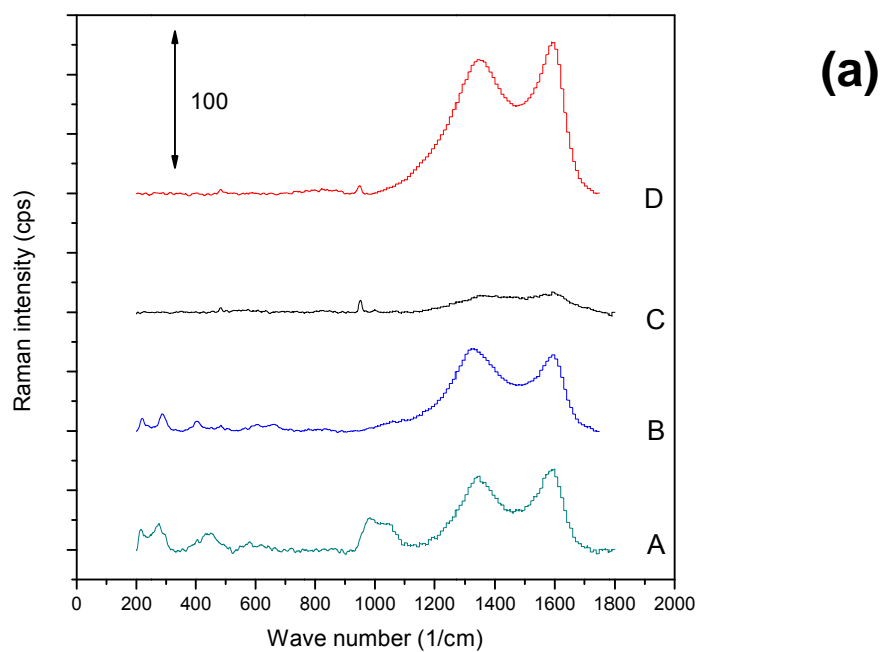


Figure 4.19(a) Raman spectra of individual (150×150) μm^2 areas in the cathode surface. More oxides from decomposition of LiFePO_4 are generated in areas of A and B. The identity of different vibrational bands is labeled in the fig.2. (b) Distribution of the band at 950 cm^{-1} in a (80×80) μm^2 area on the cathode surface. The color map, at the bottom of the figure, correlates correspond Raman intensity and the colors. The red color visualizes the region with the highest Raman intensity with the wavenumber of 950 cm^{-1} .

Fig.4.19 (b) shows surface distribution of Raman intensity for the band at 950 cm^{-1} in a more localized region of $(80\times 80)\text{ }\mu\text{m}^2$ on the cathode. The full spectrum of the individual $(20\times 20)\text{ }\mu\text{m}^2$ sub-areas along with the surface map can be utilized to locate a special vibrational band. However, as mentioned before, the individual areas of $(150\times 150)\text{ }\mu\text{m}^2$ were selected for mapping to be able to practically locate the appropriate regions for further study during the in-situ experiment.

4.4.4 In-situ Raman spectroscopy

The in-situ experiment was carried out on a post-exposed cathode electrode in a fully discharged state and after a rest of three days. Fig.4.20 displays the charge, discharge and the rest cycles of the Li-ion cell. The laser power of 2mW was applied for each measurement to the same spot on the cathode surface through the Al foil hole during the in-situ experiment. The spot size was set for $2\text{ }\mu\text{m}$ and the spectra were recorded between $(50\text{--}2000)\text{ cm}^{-1}$. All the measurements were carried out at the ambient temperature. The open circles indicate the states in which the Raman spectra were collected for 7 minutes. Charging process was performed in two different steps: a first constant-current charging process from 2.3 to 4.0V followed by the second step at a constant voltage of 4.0V. The discharge cycle was implemented by applying a constant current in a potential window between 3.2 and 2.5V. Both the discharge and the first stage of the charge carried out at 0.4C rate. The total discharge capacity was 135mAh/g, and the columbic efficiency for the cell was 84%.

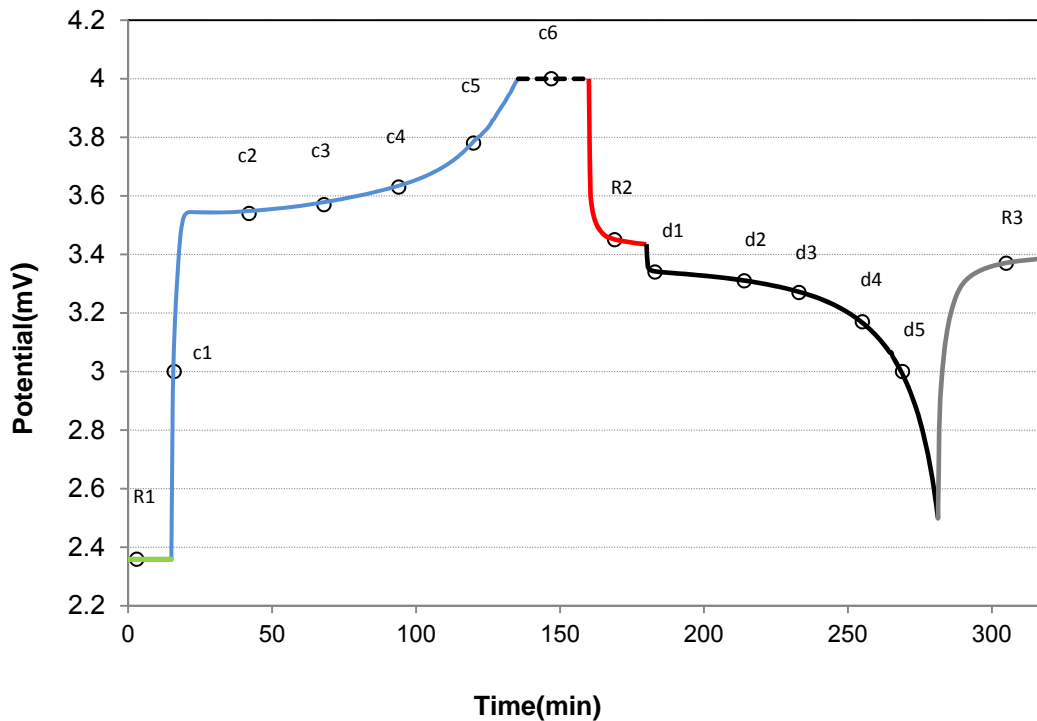


Figure 4.20 Charge, discharge and rest cycles of the C-LiFePO₄/Li cell during the in-situ experiment. During the first stage of charge and discharge cycle, the cell was charged at a constant rate of 0.4C. The second stage of charge was performed with a constant voltage at 4.0V. The open circles indicate the states when the in-situ Raman spectra were collected.

Fig. 4.21C shows the typical Raman spectra obtained during charge corresponding to the state of c3 in Fig. 4.19. The spectra contain all the necessary components for a potentially active region including, the electronically conductive G band carbon, the electrolyte (Raman spectra of individual solvent in the electrolyte are shown in Fig. 4.20A and B) in the region below 940cm⁻¹, coexisting with the active material band at about 950cm⁻¹. Table 4.4 summarizes the characteristic vibrational bands and wavenumber of the electrolyte and LiFePO₄.

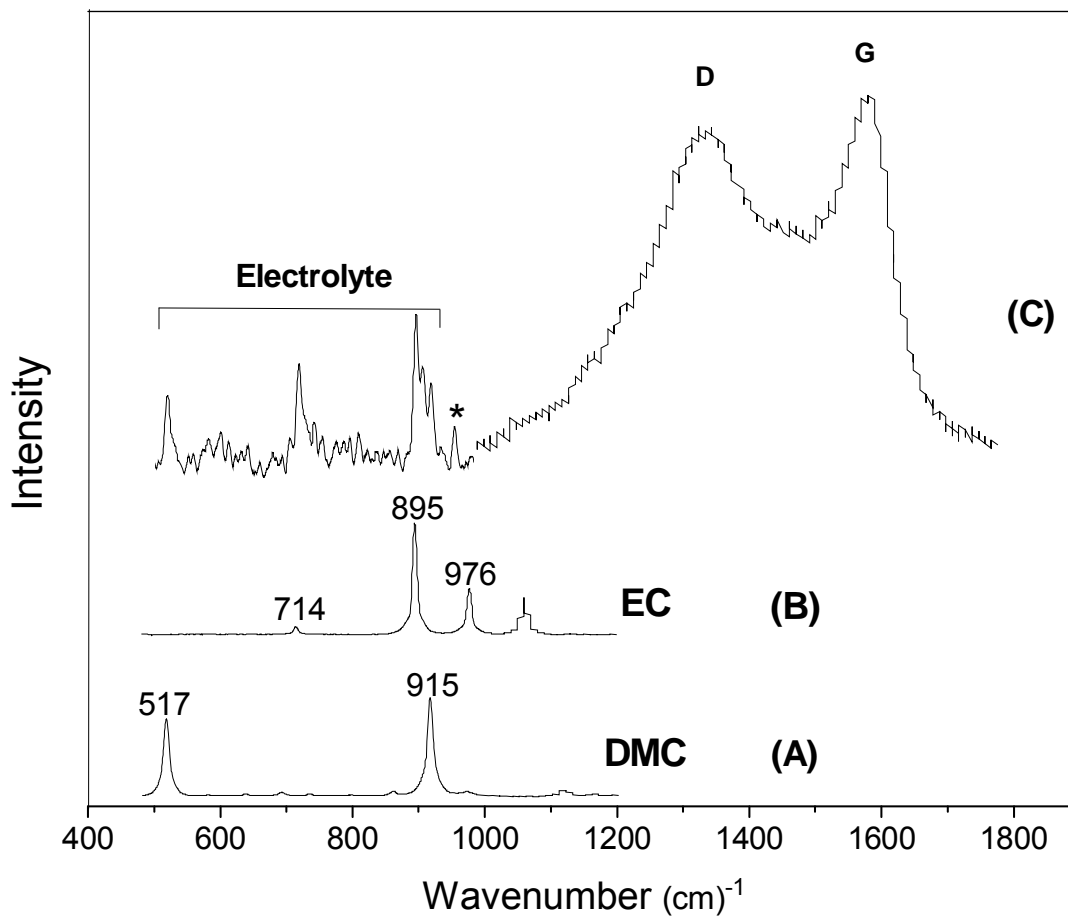


Figure 4.21 (A) The Raman spectra of DMC. The peak at about 915 cm^{-1} is assigned to C–O stretching band of the bulk DMC. (B) The Raman spectra of EC with the C–O stretching band at about 895 cm^{-1} . (C) Typical in-situ Raman spectra from (150–1800) cm^{-1} . The region below 1000 cm^{-1} has been rescaled for better illustration of the weak bands of both electrolyte and LiFePO_4 (*).

The band at about 950 cm^{-1} is attributed to the symmetric stretching modes (ν_1) of the PO_4^{3-} anions in LiFePO_4 [55, 66, 67]. The anti-symmetric stretching bands (ν_3) of the PO_4^{3-} have been reported to occur at higher wavenumbers with relatively weak intensities. The two internal bands are originating from the intermolecular vibrations of PO_4^{3-} anions, sensitive to the presence of lithium ions in the unit cell [66]. As has been reported, ex-situ Raman study of Li_xFePO_4 showed that reducing the lithium content, x , from 1 to 0.75 slightly changed the peak

profile of the 950 cm^{-1} band and also generates new weak bands at about (911, 1000-1050) cm^{-1} [55]. However, in our results, clear peak profile variation at 950 cm^{-1} and new peaks could not be observed due to low intensity of those peaks. Several bands have been reported to appear in the Raman spectra of FePO_4 (911, 960, 1124, 1064 and 1080 cm^{-1}) [55, 68] that are not found in our experiment. It is also possible that FePO_4 might exist beyond the skin penetration depth of incident laser beam, its existence was obviously not detected by the in-situ Raman from the surface of the particles. Although the Raman spectra could not provide conclusive interpretation of the profile change of the LiFePO_4 bands, they could offer insights about the dynamic processes at the surface of the particles and their adjacent electrolyte.

Table 4.4. Characteristic vibrational peaks observed in the in-situ Raman spectroscopy

Vibrational bands	LiFePO_4 (ν_1)	DMC		EC			
		Bulk	Solvated	Bulk		Solvated	
				C-O stretching	C=O Ring deformation	C-O stretching	C=O Ring deformation
Wavenumber (cm^{-1})	950	915, 517	932	895	714	904	720

The Raman peaks between 500 and 940 cm^{-1} are associated with the $\text{LiPF}_6/\text{EC}+\text{DMC}$ electrolyte (Fig.4.21). Particularly, the peak at about 714 cm^{-1} (Fig. 5.5B) has been reported for the symmetric ring deformation of EC [47, 69, 70], though it has also been assigned to C=O bending mode by Hyodo and Okabayashi [71], and Arocaby and co-workers [49]. The peaks from 880 to 940 cm^{-1} have been assigned to the stretching vibrational bands of the C-O single band of carbonate groups in EC and DMC [47, 71]. The peaks at about 915 and 895 cm^{-1} are assigned to C-O stretch bands of carbonate groups in non-solvated DMC and EC, respectively.

The spectroscopic studies of ion-ion and ion-solvent interactions for aprotic media have been reported by several research groups [47-49]. Morika et al. showed that the relative intensity of solvated EC, particularly the intensity of the C-O stretching band, is a linear function of the salt concentration in the $\text{LiPF}_6/(\text{DMC}+\text{EC})$ system [27], as the Li^+ -solvent interaction

leads to the formation of solvated products with vibrational modes at higher wavenumbers. Therefore, the level of Li^+ solvation can be calculated by relative intensity of solvation, I_r , according to the following equation

$$I_r = I_s / (I_s + I_n) \quad (4.2)$$

Where, I_n is the intensity of bulk non-solvated molecule and I_s is the intensity of solvated molecule. Both EC and DMC molecules interact with Li^+ cations but the interaction between EC and Li^+ is more intense [27]. Therefore, the relative intensity of solvation is calculated based on the C-O stretching bands of EC from 895 and 904 cm^{-1} as they are more intense. Peak deconvolution was conducted in the 870~970 cm^{-1} region as shown in Figs. 4.22 assuming a Gaussian function fit. The intensities of the solvated and non-solvated species were calculated by the integration of the corresponding peaks.

Fig. 4.23 shows the variation of Li^+ concentration in the $\text{LiPF}_6/\text{DMC+EC}$ system during the charge, discharge, and rest cycle. At the beginning of the charging process, the concentration of Li^+ at the LiFePO_4 particle surface decreased. However, after reaching a minimum value at the c_2 state, the Li^+ concentration started to increase till the c_5 state was reached, and then reduced slightly during the constant-potential charge at 4.0 V (from c_5 to c_6). As a laser spot size of 2 μm was applied in this study, the Li^+ concentration fluctuation observed in Fig. 4.23 may just reflect the localized particle-level transport dynamics, which highly depends on the balance between the Li^+ egress rate from the electrolyte near the particle surface, and the ingress rate from the LiFePO_4 particle to this region.

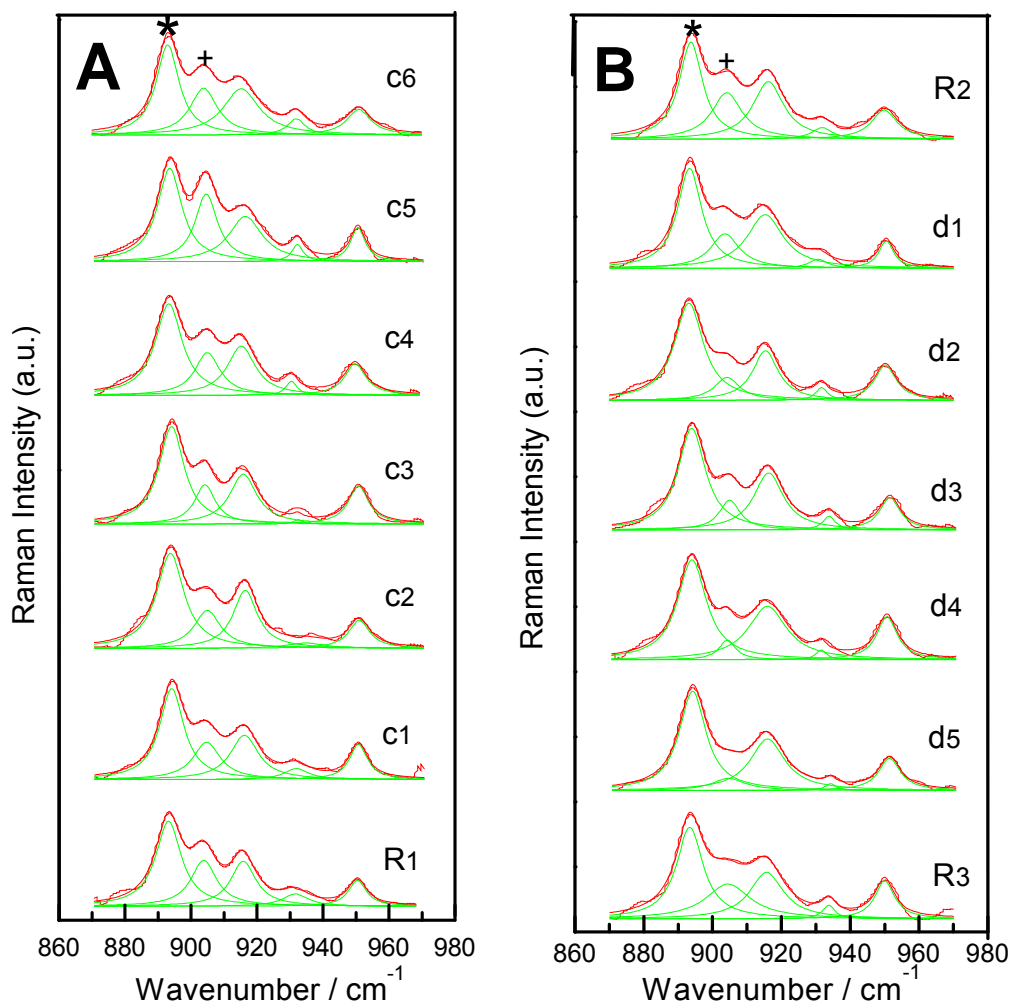


Figure 4.22 De-convoluted Raman spectra (between 870 and 970 cm^{-1}) at different states of the charge during (A) charge, and (B) discharge in the in situ experiment. The C-O stretching Raman bands of the un-solvated (*, at 895 cm^{-1}) and solvated EC (+, at 904 cm^{-1}) are labeled in (A) and (B).

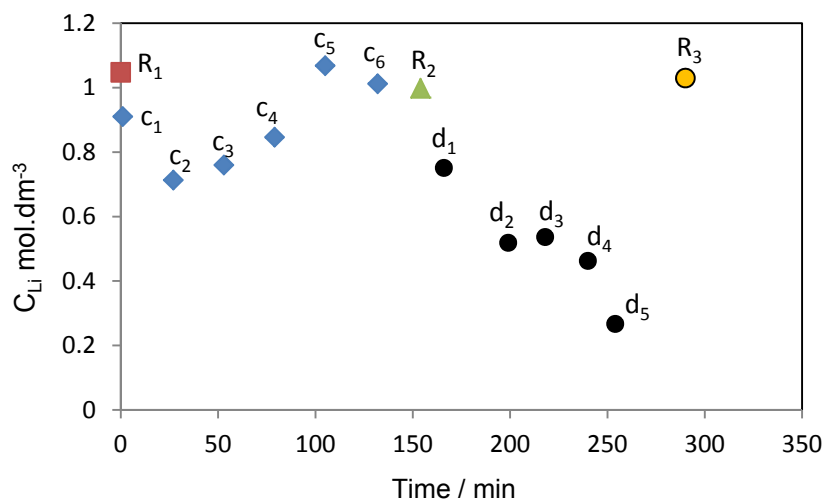


Figure 4.23 Variation of Li^+ concentration in the $\text{LiPF}_6/\text{DMC}+\text{EC}$ system during charge, discharge, and rest portions of the cycle. The Li^+ ion concentrations were computed from the Raman spectral data (Figs. 4.22 B and C) as described in the text.

In the second step of charging, at a fixed potential of 4.0 V (from c_5 to c_6), as the charging current reduces with time, the Li^+ in-coming rate from the LiFePO_4 particle decreased and the Li^+ concentration in the studied area slightly reduced. At the end of charging (c_6), the Li^+ concentration returned to the initial value (R_1) and remained constant during the rest (from c_6 to R_2) since there was no driving force for the concentration to change any more. In the discharge process, the Li^+ concentration in the electrolyte monotonically decreased due to continuous consumption of lithium ions from the electrolyte to the LiFePO_4 particle. After discharge, the consumed lithium ions were replenished by the electrolyte, and the Li^+ concentration reverted to the balanced value as in the other two rest states (R_1 and R_2).

The observed Li^+ concentration fluctuation may result from a non-uniform distribution of charging and discharging currents within the electrode, as well as unbalanced diffusion coefficients within the electrolyte and the LiFePO_4 particles. Therefore, the observed results reflect a dynamic transport process at the particle surface due to redistribution of Li^+ within the pore space of the (mesoporous) electrode, which relies on the charge/discharge rate, the physical position of the region, porosity, and thickness of the cathode electrode. The Li^+

concentration fluctuation at the LiFePO_4 particle surface has a significant implication to battery rate-limiting dynamics since the ionic conductivity of the $\text{LiPF}_6/\text{EC}+\text{DMC}$ electrolyte is a function of the salt concentration with a maximum value at about $(0.8-1.2) \text{ mol}\cdot\text{dm}^{-3}$ [55]; Therefore, deviation from the optimum Li^+ concentration at the cathode surface, especially close to the end of discharge in the d_2 - d_5 states, leads to significant loss of *local* ionic conductivity that is definitely a rate limiting factor.

4.5. Conclusion

In this chapter we have examined the effect of additive carbon on the performance and aging of LiFePO_4 cathodes in Lithium-ion Batteries. The performance of the cells with various carbon contents was examined at different rates over cycling. Charge/discharge plots, EIS and ex-situ Raman spectroscopy were used to analyze the rate performance and evaluate the conductive network of the cathodes. The aging and rate performance of C- LiFePO_4 cathodes were influenced by the quality and quantity of the conductive carbon as well as the porosity of the constructed electrode.

The cathode with 2% carbon showed a better rate performance, less internal resistance and concentration polarizations, as well as less charge transfer resistance. In addition, its larger pore size provided a better electrolyte access which in turn increased the ionic conductivity. A weak rate performance capability along with a higher capacity at 0.1C rate was achieved for 10% additive carbon. The higher capacity is considered for a proper electronic wiring and pore size to perform at 0.1C rate, at the same time high internal resistance polarization and charge transfer resistance indicates unsatisfactory conductive network to maintain the capacity at high discharge rates. 20% additive carbon has an enhanced electronic conductive network with a better rate performance than 10% carbon. Meanwhile, the small pore size prevents the electrolyte penetration into the particles which in turn reduces the total capacity.

A fast capacity fading over cycling for cathodes with 2% carbon was associated to insufficient conductive network of the cathode. Also considerably improved cycle ability of the

cathode with 10% additive carbon was addressed to the supportive role of extra carbon in retaining electronic conductivity. In-depth understanding of capacity fading was achieved comparing the D/G and sp^3/sp^2 ratios of carbon in Raman spectra. Accordingly, a faster growth in D/G and sp^3/sp^2 ratios gained over the cycling of cathodes with 2% carbon.

We have also shown the capability of in-situ Raman spectroscopy for probing the structural and compositional variations at the surface of the C- $LiFePO_4$ cathode in a charge-discharge cycle of an operating lithium ion battery. Though formation of $FePO_4$ was not detected on the particle surface during the in-situ experiment; however, its existence beyond the penetration depth of the Raman laser is quite possible. The variant electrolyte concentration on the C- $LiFePO_4$ particle surface was probed during a charge-discharge cycle. The electrolyte concentration at the particle surface was found to fluctuate during battery operation. Particularly, near the end of the discharge it reaches to a minimum which is far less than its balanced value (1 mol.dm^{-3}). The dynamics in electrolyte concentration at C- $LiFePO_4$ surface is due to competition between the in-coming and out-going rates of the lithium ions which depends on the charging rate and the physical position of the region.

Farther Raman study about the surface reactions that taking place in real situation requires to probe more localized area (100x magnification in Raman microscopy), preferably starting with non-coated nano-size $LiFePO_4$. Nano-size $LiFePO_4$ without carbon coating shows acceptable electrochemical behavior [72] with a more intense (ν_1) bands for $LiFePO_4$, providing more information about the surface reactions. Also Enhanced Raman Spectroscopy might be considered for more investigation however, applying to the actual situations remains a challenge.

REFERENCES

- [1] B. Scrosati, J.r. Garche, *Journal of Power Sources*, 195 2419-2430.
- [2] M. Perrin, Y.M. Saint-Drenan, F. Mattera, P. Malbranche, *Journal of Power Sources*, 144 (2005) 402-410.
- [3] M.S. Whittingham, *MRS Bulletin*, 33 (2008) 411-419.
- [4] R. Malik, F. Zhou, G. Ceder, *Nat Mater*, 10 (2011) 587-590.
- [5] B. Kang, G. Ceder, *Nature*, 458 (2009) 190-193.
- [6] Y.H. Chen, C.W. Wang, G. Liu, X.Y. Song, V.S. Battaglia, A.M. Sastry, *J. Electrochem. Soc.*, 154 (2007) A978-A986.
- [7] A. Patil, V. Patil, D. Wook Shin, J.-W. Choi, D.-S. Paik, S.-J. Yoon, *Materials Research Bulletin*, 43 (2008) 1913-1942.
- [8] B. Scrosati, J.r. Garche, *Journal of Power Sources*, 195 (2010) 2419-2430.
- [9] A.S. Arico, P. Bruce, B. Scrosati, J.M. Tarascon, W. Van Schalkwijk, *Nat. Mater.*, 4 (2005) 366-377.
- [10] M. Armand, J.M. Tarascon, *Nature*, 451 (2008) 652-657.
- [11] A. Vu, A. Stein, *Chemistry of Materials*, 23 (2011) 3237-3245.
- [12] S.-Y. Chung, J.T. Bloking, Y.-M. Chiang, *Nat. Mater.*, 1 (2002) 123-128.
- [13] K. Mizushima, P.C. Jones, P.J. Wiseman, J.B. Goodenough, *Materials Research Bulletin*, 15 (1980) 783-789.
- [14] C. Kim, T. Fujino, K. Miyashita, T. Hayashi, M. Endo, M.S. Dresselhaus, *J. Electrochem. Soc.*, 147 (2000) 1257-1264.
- [15] M.G.S.R. Thomas, P.G. Bruce, J.B. Goodenough, *Solid State Ionics*, 18-19, Part 2 (1986) 794-798.
- [16] Y. Shao-Horn, L. Croguennec, C. Delmas, E.C. Nelson, M.A. O'Keefe, *Nat Mater*, 2 (2003) 464-467.
- [17] S.R. Das, I.R. Fachini, S.B. Majumder, R.S. Katiyar, *Journal of Power Sources*, 158 (2006) 518-523.
- [18] A. Yamada, S.C. Chung, K. Hinokuma, *J. Electrochem. Soc.*, 148 (2001) A224.
- [19] A.K. Padhi, K.S. Nanjundaswamy, J.B. Goodenough, *J. Electrochem. Soc.*, 144 (1997) 1188-1194.
- [20] H. Huang, S.C. Yin, L.F. Nazar, *Electrochemical and Solid-State Letters*, 4 (2001) A170-A172.
- [21] D. Jugovic, D. Uskokovic, *Journal of Power Sources*, 190 (2009) 538-544.
- [22] P. Tang, N.A.W. Holzwarth, *Physical Review B*, 68 (2003).
- [23] G.G. Amatucci, J.M. Tarascon, L.C. Klein, *J. Electrochem. Soc.*, 143 (1996) 1114-1123.
- [24] Y.-G. Guo, J.-S. Hu, L.-J. Wan, *Advanced Materials*, 20 (2008) 2878-2887.
- [25] Y. Wang, G. Cao, *Advanced Materials*, 20 (2008) 2251-2269.
- [26] J.M. Tarascon, C. Delacourt, A.S. Prakash, M. Morcrette, M.S. Hegde, C. Wurm, C. Masquelier, *Dalton Transactions*, (2004) 2988-2994.
- [27] M. Morita, Y. Asai, N. Yoshimoto, M. Ishikawa, *Journal of the Chemical Society, Faraday Transactions*, 94 (1998) 3451-3456.
- [28] M. Winter, J.r.O. Besenhard, *Electrochimica Acta*, 45 (1999) 31-50.
- [29] G. Derrien, J. Hassoun, S. Panero, B. Scrosati, *Advanced Materials*, 19 (2007) 2336-2340.
- [30] T. Ohzuku, A. Ueda, N. Yamamoto, *J. Electrochem. Soc.*, 142 (1995) 1431-1435.
- [31] P. Kubiak, J. Geserick, N. Hüsing, M. Wohlfahrt-Mehrens, *Journal of Power Sources*, 175 (2008) 510-516.
- [32] A.R. Armstrong, G. Armstrong, J. Canales, R. García, P.G. Bruce, *Advanced Materials*, 17 (2005) 862-865.
- [33] T. Kawamura, S. Okada, J.-i. Yamaki, *Journal of Power Sources*, 156 (2006) 547-554.
- [34] R. Trocoli, J. Morales, S. Franger, J. Santos-Pena, *Electrochimica Acta*, 61 57-63.

- [35] D. Aurbach, B. Markovsky, G. Salitra, E. Markevich, Y. Talyossef, M. Koltypin, L. Nazar, B. Ellis, D. Kovacheva, *Journal of Power Sources*, 165 (2007) 491-499.
- [36] M. Koltypin, D. Aurbach, L. Nazar, B. Ellis, *Journal of Power Sources*, 174 (2007) 1241-1250.
- [37] R. Dedryvere, M. Maccario, L. Croguennec, F. Le Cras, C. Delmas, D. Gonbeau, *Chemistry of Materials*, 20 (2008) 7164-7170.
- [38] S.C. Nagpure, B. Bhushan, S.S. Babu, *Applied Surface Science*, 259 49-54.
- [39] e.a. M. Park, *J.Power Sources*, (2010).
- [40] M. Winter, R.J. Brodd, *Chemical Reviews*, 104 (2004) 4245-4270.
- [41] M.-L. Lee, Y.-H. Li, J.-W. Yeh, H.C. Shih, *Journal of Power Sources*, 214 (2012) 251-257.
- [42] S. Zhang, P. Shi, *Electrochimica Acta*, 49 (2004) 1475-1482.
- [43] D.I. Bower, Cambridge university press, (2002).
- [44] Y. Leng, J.Wiley, (2008).
- [45] X. Zhang, R. Frech, *J. Electrochem. Soc.*, 145 (1998) 847-851.
- [46] M. Inaba, Y. Iriyama, Z. Ogumi, Y. Todzuka, A. Tasaka, *Journal of Raman Spectroscopy*, 28 (1997) 613-617.
- [47] D. Battisti, G.A. Nazri, B. Klassen, R. Aroca, *The Journal of Physical Chemistry*, 97 (1993) 5826-5830.
- [48] W. Huang, R. Frech, R.A. Wheeler, *The Journal of Physical Chemistry*, 98 (1994) 100-110.
- [49] B. Klassen, R. Aroca, M. Nazri, G.A. Nazri, *The Journal of Physical Chemistry B*, 102 (1998) 4795-4801.
- [50] P. Novak, J.C. Panitz, F. Joho, M. Lanz, R. Imhof, M. Coluccia, *Journal of Power Sources*, 90 (2000) 52-58.
- [51] J.-C. Panitz, P. Novák, *Journal of Power Sources*, 97-98 (2001) 174-180.
- [52] R. Aroca, M. Nazri, G.A. Nazri, A.J. Camargo, M. Trsic, *Journal of Solution Chemistry*, 29 (2000) 1047-1060.
- [53] M. Kakihana, S. Schantz, L.M. Torell, *Journal of Chemical Physics*, 92 (1990) 6271-6277.
- [54] B. Sandner, J. Tübke, A. Werther, R. Sandner, S. Wartewig, S. Shashkov, - 43 (1998) - 1567.
- [55] C.M. Burba, R. Frech, *J. Electrochem. Soc.*, 151 (2004) A1032-A1038.
- [56] M.T. Paques-Ledent, P. Tarte, *Spectrochimica Acta Part A: Molecular Spectroscopy*, 30 (1974) 673-689.
- [57] E. Markevich, R. Sharabi, O. Haik, V. Borgel, G. Salitra, D. Aurbach, G. Semrau, M.A. Schmidt, N. Schall, C. Stinner, *Journal of Power Sources*, 196 (2011) 6433-6439.
- [58] ArunKumar, R. Thomas, N.K. Karan, J.J. Saavedra-Arias, M.K. Singh, S.B. Majumder, M.S. Tomar, R.S. Katiyar, *Journal of Nanotechnology*, 2009 (2009) 10.
- [59] M.M. Doeff, Y. Hu, F. McLarnon, R. Kostecky, *Electrochemical and Solid-State Letters*, 6 (2003) A207-A209.
- [60] J.D. Wilcox, M.M. Doeff, M. Marcinek, R. Kostecky, *J. Electrochem. Soc.*, 154 (2007) A389-A395.
- [61] Y. Wang, D.C. Alsmeyer, R.L. McCreery, *Chemistry of Materials*, 2 (1990) 557-563.
- [62] V. Palomares, A. Goni, I.G.d. Muro, I. de Meatza, M. Bengoechea, I. Cantero, T. Rojo, *Journal of Power Sources*, 195 (2010) 7661-7668.
- [63] F. Tuinstra, J.L. Koenig, *Journal of Chemical Physics*, 53 (1970) 1126-1130.
- [64] M. Endo, C. Kim, T. Hiraoka, T. Karaki, K. Nishimura, M.J.Matheous, S.D.M. Brown, M.S. Dresselhaus, *Journal of Materials Research*, 13 (1998) 2023-2030.
- [65] H.-C. Wong, J.R. Carey, J.-S. Chen, *International Journal of Electrochemical Science*, 5 (2010) 1090-1102.
- [66] M.T. Paques-Ledent, P. Tarte, *Spectrochimica Acta Part A: Molecular Spectroscopy*, 30 (1974) 673-689.
- [67] W. Paraguassu, P.T.C. Freire, V. Lemos, S.M. Lala, L.A. Montoro, J.M. Rosolen, *Journal of Raman Spectroscopy*, 36 (2005) 213-220.

- [68] C.M. Burba, R. Frech, *Spectrochimica Acta Part A: Molecular and Biomolecular Spectroscopy*, 65 (2006) 44-50.
- [69] S.R. Starkey, R. Frech, *Electrochimica Acta*, 42 (1997) 471-474.
- [70] G.J. Janz, J. Ambrose, J.W. Coutts, J.R. Downey Jr, *Spectrochimica Acta Part A: Molecular Spectroscopy*, 35 (1979) 175-179.
- [71] S.-A. Hyodo, K. Okabayashi, *Electrochimica Acta*, 34 (1989) 1551-1556.
- [72] M. Gaberscek, R. Dominko, J. Jamnik, *Journal of Electrochemistry Communications*, 9 (2007) 2778–2783.

BIOGRAPHICAL INFORMATION

Amir Salehi received his bachelor degree in Applied Physics from Tabriz University in 1990 and later while working in industry, he completed his Master degree in Ceramic Engineering in 2005. He joined to the department of Materials Science and Engineering of UT Arlington on fall 2011 to learn state-of-the-art technologies and further improve his skills. Li-ion batteries have been his primary research interest and he first started to investigate about it in his thesis towards Ceramic Engineering degree. Accordingly, he examined electro active iron oxide materials as the cathode of Li-ion batteries. He also studied the effect of synthesis route on the microstructure, and electrochemical behavior of $\text{Li}_x\text{Fe}_y\text{O}_z$ materials. He continued his research on lithium ion batteries in UT Arlington and developed a practical method for Raman study of real time reactions taking place in the LiFePO_4 /electrolyte interface in a working battery. His career performance shows diverse areas of experience in design, formulation and manufacturing of Alumina and SiC ceramics including high and low density muffles, tubes, crucibles, plates, stands and saggars. He also participated in several research projects for formulation and process development of ceramics and composites. After graduation he will join to industry to enhance his professional experience either in the field of ceramics or Li-ion batteries.